UNIVERSITY OF SOUTHAMPTON

Transient black hole candidates observed with INTEGRAL

Fiamma Capitanio

Submitted for the degree of Doctor of Philosophy

SCHOOL OF PHYSICS AND ASTRONOMY
FACULTY OF ENGINEERING, SCIENCE AND MATHEMATICS

May 17, 2007

UNIVERSITY OF SOUTHAMPTON

ABSTRACT

FACULTY OF ENGINEERING, SCIENCE AND MATHEMATICS

SCHOOL OF PHYSICS AND ASTRONOMY

Doctor of Philosophy

Transient black hole candidates observed with INTEGRAL

by Fiamma Capitanio

The work presented in this thesis has been developed inside the IBIS survey team and presents results from two different topics related to the IBIS survey work.

The first part of the work is focused on two specific sources: IGR J17091-3624 and H1743-322 considered as part of a sample of 7 transient black hole candidates (BHC) observed by *INTEGRAL* in outburst. Both sources have been followed by *INTEGRAL* for the entire outburst duration on a wide energy range from 3 keV up to 250 keV. The combined spectral evolution of H1743-322 with the X–ray monitor, JEM-X, the γ–ray telescope, IBIS and the spectrometer, SPI, gives a clear vision of a black hole candidate spectral evolution from hard to soft state and then back to hard state. The set of data used for IGR J17091-3624 analysis allowed a joint fit of a *RXTE/INTEGRAL* spectrum in the low/hard state. Also a soft state black body emission of the source is reported for the first time.

The second part of this thesis is focused on the analysis of all the archive data of the wide field cameras (WFCs) on board BeppoSAX satellite. Previous works published are dedicated on transient sources detection, while this work, producing a mosaic of the images of all the single WFC pointing, is more optimised for fainter, persistent sources observations. Since a final catalogue of the sources detected with the wide field cameras has not been published yet, this work represent the first unbiased source list compilation produced in this way from overall WFCs data set. The mosaiking technique approach, developed for the IBIS survey, has been successfully applied, for the first time, to the BeppoSAX WFCs. The list of sources detected in the wide field cameras mosaics have then been compared with the third IBIS survey catalogue in order to check the uncertain source detections.

Contents

1 Introduction 4

2 Galactic and extragalactic objects emitting in high energy bands 9

2.1 Black-hole candidates, X-ray novae, microquasars 10

2.2 Accreting neutron stars 12

2.3 Cataclysmic variables 13

2.4 Supernovae and Supernovae remnants 13

2.5 Isolated Pulsars 15

2.6 AGN 16

2.7 Gamma-ray bursts 18

2.8 Concluding remarks 18

3 The INTEGRAL mission and techniques for γ and X-ray astronomy 19

3.1 High energy detectors: general properties 19

3.1.1 Gas-filled detectors 23

3.1.2 Scintillation detectors 24

3.1.3 Semiconductor detectors 25

3.2 High energy telescopes and imaging astrophysical detectors 26

3.2.1 Compton Telescopes 27

3.2.2 Imaging with a coded mask telescope 27

3.2.3 Background shields 30

3.3 The INTEGRAL mission 31

3.3.1 Observations and goals 32

3.3.1.1 Observing Programme 32

3.3.1.2 Observing modes 34

3.4 Gamma-ray telescopes on-board INTEGRAL 35

3.4.1 The gamma-ray imager IBIS 36

3.4.1.1 ISGRI spectral capability 37

3.4.2 The spectrometer SPI 38

3.4.3 Monitors for counterparts: JEM-X and OMC 41

3.5 Summary 42

4 Introduction to X-ray Novae **43**

4.1 X-ray Binaries 43

4.1.1 The Compact Objects 44

4.1.2 Classification and distribution in the sky 47

4.2 Transient X-ray binaries (X-ray novae) 50

4.3 Review of physical emission mechanisms of X-ray transient BHB Spectra 53

4.3.1 Accretion disc: standard model 53

4.3.2 Disc-Corona Model 58

4.3.2.1 Inverse Compton scattering 60

4.3.2.2 Geometry of the model 62

4.3.3 Radio emission from black hole binaries: jet production 64

4.3.3.1 Synchrotron radiation: brief review 65

4.3.3.2 The jets 66

4.4 Correlation between X-ray and radio emission: a new spectral state classification 67

4.4.1 Low/Hard State (LS) 68

4.4.2 Hard Intermediate State (HIMS) I 69

4.4.3 Soft Intermediate State (SIMS) 69

4.4.4 High/Soft State (HS) 70

4.4.5 Hard Intermediate State (HIMS) II 70

4.5 Conclusions and open questions 71

5 Global view of the BHC observed with INTEGRAL 73

5.1 First and second survey catalogue 73

5.2 A Sample of transient black hole candidate observed by INTEGRAL 74

5.2.1 Transient BHC sample 75

5.3 Concluding remarks 82

6 IGR J17464–3213 (H1743–322) 83

6.1 History and characteristics of the source 83

6.2 Data Analysis 84

6.3 Results 86

6.3.1 The time evolution of the outbursts 86

6.3.2 First outburst 88

6.3.3 Second outburst 90

6.3.4 Spectral evolution of the source 92

6.3.4.1 First outburst 92

6.3.4.2 Second outburst 96

6.4 Discussion and Conclusion 97

7 IGR J17091–3624 **101**

7.1 History and characteristics of the source 101

7.1.1 Improvements over previous analysis 102

7.2 Data Analysis 103

7.3 Results 105

7.3.1 Time evolution 106

7.3.2 Spectral evolution of IGR J17091–3624 107

7.4 Discussion and conclusions 111

7.4.1 Similar properties between IGR J17091–3624 and IGR J17464–3213 114

7.4.2 New open questions on IGR J17091–3624 from optical observations 115

8 BeppoSAX WFC sky **116**

8.1 Introduction and aim of the work 116

8.2 BeppoSAX satellite 117

8.2.1 The scientific payload 117

8.2.2 BeppoSAX WFC 119

8.3 WFCs sky map production 120

8.3.1 Source search and localization 122

8.4 Correlation between the IBIS and WFC maps 123

8.5 Sources found only in WFCs maps and comparison with IBIS excesses 127

8.5.1 EXMS B1210–645 128

8.5.2 3A 0726–260 128

8.5.3 QSO B1821+643 130

8.6 Light curves from SAX/WFC data 130

8.6.1 Investigation of possible sources 132

8.6.2 Temporal studies of BHC 133

8.7 Concluding remarks 136

9 Conclusions **147**

List of Figures

1.1 The earth atmospheric transparency to cosmic electromagnetic radiation. . 4

1.2 An artist's impression of the INTEGRAL spacecraft. At the front is the SPI instrument with its circular coded mask and behind the square mask of the IBIS instrument. JEM-X, the X-ray monitor, is located between these two instruments with the OMC (Optical Monitoring Camera) to the side. The *INTEGRAL* payload is described in detail in Section 3. 6

2.1 Different spectral states of the BH binary Cyg X-1 (Zdziarski et al. 2002). 11

2.2 Life cycle of a massive star. 14

2.3 *INTEGRAL*/IBIS spectrum of the SNR Cas A. The spectrum shows the 2 ^{44}Ti emission lines at 68 & 78 keV. The continuum spectrum is fitted with a powerlaw with $\Gamma = 3.3 \pm 0.1$ (Renaud et al. 2006). 15

2.4 The folded light curves of some of the known γ-ray pulsars compared to other energies. 16

2.5 A schematic view of unified Active Galactic Nuclei model. 17

3.1 γ-ray processes as a function of atomic number and energy. 20

3.2 Schematic view of a gas-filled detector. 24

3.3 Schematic view of a scintillator detector and photomultiplier tube system. 25

3.4 COMPTEL (Schronfelder et al. 1993), the imaging telescope on board NASA Compton Gamma Ray Observatory (CGRO), consists of two layers of detectors. A photon is first Compton scattered in one of the upper detector modules and then – in the ideal case – completely absorbed by a detector module of the lower layer. COMPTEL covers the energy range between 1–30 MeV with an energy resolution between 10% at low energies and 5% at the high energies. The instrument had a field of view of one steradian and a location accuracy of about 1^o. 28

3.5 Schematic diagram illustrating the working principle of a coded aperture camera: the recorded count rate in each pixel of the detection plane is the summation of contributions from each source flux modulated by the mask. 29

3.6 Last decade γ-ray missions performances compared with the *INTEGRAL* performance after 6 months of operations. 33

3.7 An *INTEGRAL* payload modules view. 35

3.8 Scheme of IBIS detectors and shielding system. 38

3.9 IBIS and SPI coded mask patterns 39

4.1 Examples of a typical HMXB (top) and LMXB (bottom). The compact object (in this case a neutron star) in the HMXB is fed by a strong high-velocity stellar wind. The compact object in an LMXB is surrounded by an accretion disc which is fed by Roche lobe overflow. 48

4.2 Distribution of Low-Mass X-ray Binaries (open symbols) and High Mass X-ray Binaries (filled symbols) in galactic coordinates (Grimm et al. 2002) 49

4.3 Schematic spectrum of an ADAF around a black hole. S, C, and B refer to electron emission by synchrotron radiation, IC scattering, and Bremsstrahlung, respectively. The solid line corresponds to a low $\dot{m}$, the dashed line to an intermediate $\dot{m}$, and the dotted line to a high $\dot{m} \sim \dot{m}_{crit}$. The gamma-ray spectrum is due to the decay of neutral pions created in proton-proton collisions. r represents, in arbitrary units, the different distances from the black hole (corresponding to different parts of the spectrum) (from Narayan et al. 1998). 59

4.4 (a) A schematic representation of the likely geometry in the hard state, consisting of a hot inner accretion flow surrounded by an optically-thick accretion disc. In this case the hot flow constitutes the base of the jet (the jets are omitted from the figure for clarity). The disc is truncated away from the minimum stable orbit, but it overlaps with the hot flow. The soft photons emitted by the disc are Compton upscattered in the hot flow, and emission from the hot flow is partly Compton-reflected from the disc. (b) The likely geometry in the soft state consisting of flares/active regions above an optically-thick accretion disc extending close to the minimum stable orbit. The soft photons emitted by the disc are Compton upscattered in the flares, and emission from the flares is partly Compton-reflected from the disc (Zdziarski & Gierliński 2004). 63

4.5 Representation of the hardness-intensity diagram for a transient BHC in outburst. 68

5.1 XTE J1908+094: A, B and C *RXTE*/PCA bands light curves and the hardness ratio (see text). 76

5.2 XTE J1908+094. IBIS light curves in three energy bands (20-40, 40-60, 60-100 keV) and the hardness ratio (see text). 77

5.3 IGR J18539+0727: IBIS light curves in three energy bands (20-40, 40-60, 60-100 keV) and the hardness ratio (see text). 78

5.4 XTE J1720–318: A, B and C *RXTE*/PCA bands light curves and the hardness ratio (see text). 79

5.5 XTE J1720–318: IBIS light curves in three energy bands (20-40, 40-60, 60-100 keV) and the hardness ratio (see text). 80

5.6 4U 1630–47: A, B and C *RXTE*/PCA bands light curves and the hardness ratio (see text). 81

5.7 4U 1630–47: IBIS light curves in three energy bands (20-40, 40-60, 60-100 keV) and the hardness ratio (see text). 81

5.8 IGR J17285–2922: IBIS light curves in three energy bands (20-40, 40-60, 60-100 keV) and the hardness ratio (see text). 82

6.1 *Top panel: RXTE*/PCA 1-12 keV light curve of the H1743–322 temporal behaviour from March 2003 to August 2005. The dotted rectangles represent the *INTEGRAL* observation periods of the source (red: public data, green: proprietary data, violet arrows: radio observations with detection, pink arrow: radio observations without detection). *Bottom panel:* the zoom on the first outburst data of the *RXTE*/ASM 1-12 keV light curve. The dotted rectangles are the *INTEGRAL* fully coded observation periods of the source with their revolution numbers (the arrows have the same meaning explaned in the top panel caption). 85

6.2 *RXTE*/PCA light curve in A (1.5-3 keV), B (3-5 keV), C (5-12 keV) energy bands of H1743–322 during its three outbursts (from March 2003 to August 2005) and the hardness ratio (see Section 6.3.1). 87

6.3 IBIS light curves of H1743–322 (20-40 keV, 40-60 keV, 60-100 keV) and the hardness ratio (see Section 6.3.1). 88

6.4 (a) 20-40 keV and (b) 40-60 keV IBIS light curves from revolution 53 to revolution 61. The hardness ratio derived from the two energy ranges is shown in the bottom part of the figure (c) and defined in Section 6.3.2. . . 89

6.5 IBIS and JEM-X light curves binned to 2000 seconds of the July 2004 outburst. 90

6.6 *INTEGRAL* hardness ratio curve around the peak present in the declining part of the second outburst. The HR is defined in Section 6.3.3. 91

6.7 IBIS, JEM-X and SPI common spectra in different states of the source outburst: the numbers on the top of each spectrum indicate the revolution number of the corresponding *INTEGRAL* observation. 93

6.8 IBIS and JEM-X common spectra during the VHS of the source outburst (revolution 63). The data were analysed with OSA software version 5.2. . 94

6.9 Flux vs. powerlaw photon index for every SCW. The labels indicate the revolution number. 96

6.10 Spectrum of the top of the peak shown in Figure 6.5. 97

6.11 Photon index vs. flux of the different spectra during the outburst. 97

7.1 The 20-150 keV IBIS image of the field near IGR J17091–3624. It can be seen that IGR J17098-3628 (1) is not visible during the *RXTE*/PCA observations of IGR J17091–3624 (2), which argues against any contamination in the PCA field of view. 104

7.2 The 20-40 keV and 40-100 keV light curves (the top and middle panel, respectively) and the corresponding hardness ratio (the bottom panel), with the solid line representing a value of 1. 106

7.3 Left panel: the *RXTE*/IBIS count spectra for revs. 61-63; Right panel: the JEM-X/IBIS count spectra for revs. 100-119. 109

7.4 The unfolded spectra showing the source evolution during the *INTEGRAL* and *RXTE* observations. The red spectrum (PCA/IBIS) corresponds to revs. 61-63, the blue spectrum (JEM-X/IBIS) corresponds to revs. 100-119, and the green spectrum (IBIS) corresponds to revs. 164-185. The *Fe K*α line, shown by the red dotted curve, is due to the galactic ridge emission. The blue dotted curves denote the disk blackbody and powerlaw components of the models. 111

7.5 The spectra of IGR J17091–3624 during the rising part of the outburst (red: hard state; blue: soft state), compared with the spectra of IGR J17464–3213 also corresponding to the rising part of its outburst (dark green: soft state; light green: hard state). The blue and red dotted curves denote the same model components as in Fig. 7.4. The dark green dotted curves denote the blackbody and thermal-Compton components of the corresponding fit. 112

7.6 galactic centre region IBIS image between 20-40 keV covering a period in which both IGR J17091–3624 and IGR J17464–3213 were in outburst. . . 114

8.1 *BeppoSAX* scientific payload accommodation. 118

8.2 Energy coverage of *BeppoSAX* Instrument. 119

8.3 View of one of the *BeppoSAX* Wide Field Cameras 120

8.4 Exposure final map of the WFCs images mosaic. 123

8.5 WFCs final mosaic between 3-17 keV: Zoom of the galactic centre region. . 123

8.6 WFCs final mosaic between 17-28 keV: Zoom of the galactic centre region. 124

8.7 Percentage of different source types detected in WFC and IBIS/ISGRI catalogues. The question mark indicates the unidentified sources. 125

8.8 Percentage of different source types detected only by WFCs and by both WFCs and IBIS. The question mark indicates the unidentified sources. . . 126

8.9 Percentage of different AGN types detected only by WFCs and by both WFCs and IBIS. 127

8.10 Zoom of the IBIS maps 18-60 keV (left) and 20-100 keV (right) centered around the coordinates of EXMS B1210–645. 128

8.11 Zoom of the WFCs maps 3-17 keV (left) and 17-28 keV (right) centered around the coordinates of EXMS B1210–645. 129

8.12 Zoom of the IBIS maps 18-60 keV (left) and 20-100 keV (right) centered around the coordinates of 3A 0726–260. 129

8.13 Zoom of the WFCs maps 3-17 keV (left) and 17-28 keV (right) centered around the coordinates of 3A 0726–260. 130

8.14 Zoom of the IBIS maps 18-60 keV (left) and 20-100 keV (right) centered around the coordinates of QSO B1821+64. 131

8.15 Zoom of the WFCs maps 3-17 keV (left) and 17-28 keV (right) centered around the coordinates of QSOB1821+64. 131

8.16 Light curves of one of the possible new sources (NEW-339, see Table 8.2) in two energy ranges 3-17 keV (top) and 17-28 keV (bottom). The zero flux line is represented in red. 132

8.17 Light curves of one of the possible new sources (NEW-8046, see Table 8.2) in two energy ranges 3-17 keV (top) and 17-28 keV (bottom). The zero flux line is represented in red. 133

8.18 WFC light curves of the BHC IGR J17091–3624 in two energy ranges 3-17 keV (top) and 17-28 keV (bottom). The green lines sign the periods of the detections reported by In 't Zand et al. (2004). The zero flux line is represented in red. 134

8.19 3-17 keV mosaic image of the BHC IGR J17091–3624 during the 2001 outburst according to In 't Zand et al. (2004). 135

8.20 Light curves of the BHC 4U 1630–47 in two energy ranges 3-17 keV (top) and 17-28 keV (middle) and hardness ratio (bottom) (for the hardness ratio definition see text). The zero flux line is represented in red. 136

8.21 Light curves of 4U 1630–47. *Top panel RXTE*/ASM light curve (5-12 keV). *Bottom panel* WFC light curve (3-17 keV). 137

List of Tables

3.1 An overview of the IBIS scientific capabilities. 40

3.2 An overview of the SPI scientific capabilities. 41

3.3 An overview of the JEM-X scientific capabilities. 42

4.1 Candidate black hole binaries from Liu et al. (2000), Liu et al. (2001) and Bird et al. (2005). 45

6.1 Fit parameter values of the first outburst spectra (90% confidence). $T_{\rm in}$: temperature at inner disk radius; $N_{\rm Disk}=((R_{\rm in}/km)/(D/10kpc))^2 \times \cos(\theta)$, where $R_{\rm in}$ is the inner disk radius, D the distance to the source, and θ the angle of the disk; $kT_{\rm e}$: electron plasma temperature; τ_p: plasma optical depth; $N_{\rm Comp}$: COMPTT normalization constant. 95

7.1 The log of the *INTEGRAL* observations of IGR J17091–3624 used for the spectral fits. 104

7.2 The fit parameters to the PCA/IBIS spectrum of revs. 61-63 with the COMPTT and COMPPS models (see the red spectrum in Figure 7.4). . . . 110

7.3 The fit parameters to the JEM-X/IBIS spectrum of revs. 100-119 with the disk blackbody and a powerlaw model (see the blue spectrum in Figure 7.4). 110

7.4 The fit parameters to the hard-state spectrum of the black hole candidate IGR J17464–3213 (= H1743–322, Capitanio et al. 2005) with the COMPTT and COMPPS models (see the light green spectrum in Figure 7.5). 112

8.1 *BeppoSAX* WFCs characteristics compared with the IBIS/ISGRI ones. 121

8.2 List of sources detected in WFCs mosaics. The sources in bolted have not been detected in IBIS maps. While the others have been detected in both instruments. 138

List of acronyms

ADAF	Advection Dominated Accretion Flow
AGN	Active Galactic Nuclei
BHB	Black Hole Binary
BHC	Black Hole Candidate
CGRO	Compton Gamma-Ray Observatory
COMPTEL	Compton Telescope on board CGRO
FCFOV	Fully Coded Field Of View
FOV	Field Of View
FWHM	Full Width At Half Maximum
GCDE	Galactic Centre Deep Exposion
GPS	Galactic Plane Scan
GRB	Gamma-Ray Burst
HIMS	Hard Intermediate State
HMXB	High Mass X-ray Binary
HPGSPC	High Pressure Gas Scintillation Proportional Counter
HR	Hardness Ratio
HS	High Soft state
IC	Inverse Compton
IBIS	Imager on Board the INTEGRAL Satellite
INTEGRAL	INTErnational Gamma-Ray Laboratory
IROS	Iterative Removal Of Sources
IS	Intermediate State
ISGRI	INTEGRAL soft Gamma-Ray Immager
JEM-X	Joint European X-ray Monitor
LECS	Low Energy Concentrator Spectrometer
LMXB	Low Mass X-ray Binary
LS	Low State
LUTs	Look Up Tables
MECS	Medium Energy Concentrator Spectrometer
MJD	Modified Julian Date

NFI	Narrow Field Instruments
NRAO	National Radio Astronomy Observatory
NS	Neutron Star
OMC	Optical Monitoring Camera on board INTEGRAL
OSA	INTEGRAL Off Line Scientific Analysis
PCFOV	Partially Coded Field Of View
PDS	Phoswich Detector System
PICsIT	Pixilated CsI Telescope
PSLA	Point Source Location Accuracy
QPO	Quasi-Periodic Oscillations
RXTE	Rossi X-ray Timing Explorer
SAX	Italian Satellite for X-ray Astronomy
SIMS	Soft Internediate State
SCW	Science Window
SNR	Super Nova Remnants
SPI	SPectrometer on INTEGRAL
TBHB	Transient Black Hole Binary
ToO	Target of Opportunity
VHS	Very High State
WFC	Wide Field Camera on board BeppoSAX
XMM	X-ray spectroscopy Multi Mirror
XN	X-ray Nova
XSPEC	X-ray Spectral Fitting Package

Acknowledgements

I would like to thank my supervisor Dr. Tony Bird for having given me the possibility to have the PhD at the Southampton University, for his helpful support and for having shared all his knowledge with me. This allowed me to widen my own.

I would also like to thank Dr. Angela Bazzano and Dr. Pietro Ubertini ("my Italian bosses") that gave me the opportunity to have a PhD, supporting me with their patient assistance during the work and the thesis writing. It is important to thank them for their financial support that was (and still is) fundamental for this PhD and for my life. I am particularly grateful to my room-mate in Rome, Antonella Tarana for the fruitful scientific discussions and her psychological support. My thanks also go to the Roman IBIS group, especially Giovanni De Cesare, Maria Teresa Fiocchi and Melania Del Santo for their careful advises and their friendly assistance.

I would also like to thank my room-mates in Southampton Vito Sguera and Manuela Molina who gave me a lot of advises on how to survive in Southampton and who helped me to feel at home. My gratitude also goes to Adam Hill and Elisabeth Barlow for their help. Finally I'm grateful to my family: my mother, my father and my husband Andrea that supported (and bore) me along all this adventure.

This thesis is dedicated to my dog Luna that faithfully waited for me during the whole period I spent in Southampton and who is still very angry for this.

Declaration

This thesis represents the result of three years of research performed by the author as a part of the IBIS survey team (of which the author is a member). In particular this work has been developed thanks to the collaboration between the IBIS Team of the Italian institute IASF-Roma/INAF of Rome (*Istituto di Astrofisica Spaziale e Fisica Cosmica di Roma / Istituto Nazionale di Astrofisica*) and the University of Southampton. The author's work can be divided in two principal topics:

- The first topic concerns the IBIS data analysis and interpretation of transient black hole candidates detected in outburst in the survey data. Two of them, IGR J17091–3624 and H1743–322 (IGR J1746–3213), have been analysed by the author in detail because of their brightness. For these two sources it was possible to collect also the data of the X-ray monitor JEM-X. While only for H1743–322, Dr. Angelique Joinet (CNRS-Toulose, France) provided the extraction of the *INTEGRAL* spectrometer SPI spectrum.

- The second topic concerns the analysis and mosaicking of the data collected by the wide field cameras (WFCs) on board the BeppoSAX satellite during the entire operational life. The WFC data have been collected from the IASF-Rome archive created by Mrs Catia Spalletta. The author had the responsibility of the imaging processing and source identification, extraction and light curves production. Dr. A. J. Bird provided the mosaicking and the source location softwares employed in the analysis.

Publications

Most of the material found in this thesis has been already published or is accepted for publication or is in preparation for publication and performed solely by the author. All the papers concerning the work presented in this thesis are listed below:

"Spectral States of the X-Ray Binary IGR J17091–3624 Observed by INTEGRAL and RXTE" **Capitanio, F.**, Bazzano, A., Ubertini, P., Zdziarski, A. A., Bird, A. J., De Cesare, G., Dean, A. J., Stephen, J. B., Tarana, A. 2006, ApJ, 643, 376

"3-200 keV Spectral States and Variability of the INTEGRAL Black Hole Binary IGR J17464–3213" **Capitanio, F.**, Ubertini, P., Bazzano, A., Kretschmar, P., Zdziarski, A. A., Joinet, A., Barlow, E. J., Bird, A. J., Dean, A. J., Jourdain, E., De Cesare, G., Del Santo, M., Natalucci, L., Cadolle Bel, M., Goldwurm, A. 2005, ApJ, Volume 622, 503.

"The 3rd IBIS/ISGRI soft gamma-ray survey catalog" A. J. Bird, A. Malizia, A. Bazzano, E. J. Barlow, L. Bassani, A. B. Hill, G. Belanger, **F. Capitanio**, D. J. Clark, A. J. Dean, M. Fiocchi, D. Gotz, F. Lebrun, M. Molina, N. Produit, M. Renaud, V. Sguera, J. B. Stephen, R. Terrier, P. Ubertini, R. Walter, C. Winkler, J. Zurita. 2007, Accepted for publication in ApJ Suppl.

"The second IBIS/ISGRI Soft Gamma-Ray Galactic Plane Survey Catalogue", Bird, A. J., Barlow, E. J., Bassani, L., Bazzano, A., Belanger, G., Bodaghee, A., **Capitanio, F.**, Dean, A. J., Fiocchi, M., Hill, A. B., Lebrun, F., Malizia, A., Mas-Hesse, J. M., Molina, M., Moran, L., Renaud, M., Sguera, V., Shaw, S. E., Stephen, J. B., Terrier, R., Ubertini, P., Walter, R., Willis, D. R. & Winkler, C., 2006, ApJ, 366, 765

"The First IBIS/ISGRI Soft Gamma-Ray Galactic Plane Survey Catalogue", Bird, A. J., Barlow, E. J., Bassani, L., Bazzano, A., Bodaghee, A., **Capitanio, F.**, Cocchi, M., Del Santo, M.,Dean, A. J., Hill, A. B., Lebrun, F., Malaguti, G., Malizia, A., Much, R., Shaw, S. E., Stephen, J. B., Terrier, R., Ubertini, P., Walter, R., 2004, ApJ 607, L33

"From BeppoSAX to INTEGRAL: Wide Field Camera results on the Galactic Plane and INTEGRAL prospective" **Capitanio, F.**, Bazzano, A., Cocchi, M., Natalucci, L., Ubertini, P., in't Zand, J. J. M., Heise, J. Nuclear Physics B, Proc. Sup., 2004, 132, 580

"Monitoring of transient black hole candidates observed in the INTEGRAL survey" **Capitanio, F.**, Bazzano, A., Bird, A., J., Ubertini, P., Federici, M. Proceedings of the 6th INTEGRAL Workshop 2006, submitted

"New outbursts of the black hole candidate H1743–322/IGR J17464–3213 observed by INTEGRAL" **Capitanio, F.**, Bazzano, A., Ubertini, P., Bird, A. J., Proceedings of the VI Microquasar Workshop: Microquasars and Beyond. September 18-22 2006, Societá del Casino, Como, Italy in publication (for the on line version

see http://pos.sissa.it)

"Two years of INTEGRAL observation of the BHC IGR J17464–3213" **Capitanio, F.**, Bazzano, A., Ubertini, P., Cesare, G. De, Santo, M. Del, Tarana, A., Joinet, A. 2006, Ad.Sp.R., 38,2816

"High-Energy Behavior of the BHC IGR J17464–3213" **Capitanio, F.**, Kretschmar, P., Ubertini, P., Barlow, E. J., Bazzano, A., Brandt, S., Bouchet, L., Budtz-Jorgensen, C., Cadolle Bel, M., Castro-Tirado, A., Dean, A. J., De Cesare, G., Del Santo, M., Farinelli, R., Frontera, F., Gehrels, N., Goldoni, P., Goldwurm, A., Huovelin, J., Lund, N., Mirabel, F., Natalucci, L., Piraino, S., Reglero, V., Roques, J. P., Tarana, A., Vilhu, O., Westergaard, N. J., Zdziarski, A. A. Proceedings of the 5th INTEGRAL Workshop on the INTEGRAL Universe (ESA SP-552). 16-20 February 2004, Munich, Germany. Scientific Editors: V. Schönfelder, G. Lichti & C. Winkler, p.313, 2004

"IGR J17464–3213" Revnivtsev, M., Chernyakova, M., **Capitanio, F.**, Westergaard, N. J., Shoenfelder, V., Gehrels, N., Winkler, C. The Astronomerś Telegram, 132, 2003

"IGR J17091–3624" Kuulkers, E., Lutovinov, A., Parmar, A., **Capitanio, F.**, Mowlavi, N., Hermsen, W. The Astronomer's Telegram, 149, 2003

Chapter 1

Introduction

The development of high energy astronomy showed a much larger variety of sources in the sky than optical astronomers had known and opened new horizons for investigations of celestial bodies. Luminous X-ray and γ-ray sources have been observed both in our and in other galaxies. The high energy activity of most of the objects observed can be explained by the release of potential energy in a strong gravitational field such as the one produced by a compact object like a black hole or a neutron star. This process takes place in the form of accretion of gas onto the compact object, which is accompanied by emission mainly in the form of UV, X-ray and γ-ray photons.

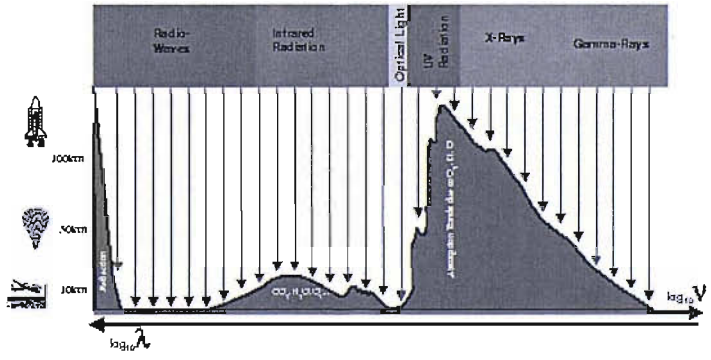

Figure 1.1: The earth atmospheric transparency to cosmic electromagnetic radiation.

The opacity of the atmosphere for X and γ wavelengths, due to photoelectric absorption of photons by atoms and molecules, did not permit the development of high energy astronomy until it was possible to get detectors above all or most of the atmosphere (see Fig. 1.1). The first detectors were launched in 1949 on board rockets and observed for the first time the X-ray emission from the Sun. In 1962 the first observation of a galactic source, Sco X-1, was again performed with a detector on board a rocket.

The satellite era began in the late 1960s and early 1970s with a γ-ray satellite *OSO-3*, the X-ray missions *Uhuru*, the *HEAO* satellite series and others. Their observations allowed the detection and classification of numerous X-ray sources, among them accreting compact objects such as neutron stars and black holes. The 1980s and 1990s brought rapid technical development. Among others, observations by the *ROSAT*, *Ginga*, *ASCA*, *CGRO*, *RXTE* and *BeppoSAX* satellites provided broad-band (from hundreds of eV to MeV range) spectra of accreting black holes as well as allowing for timing analysis on millisecond time scales. The recent satellite missions *XMM-Newton*, *Chandra*, *INTEGRAL* and *Swift* have provided spectral and spatial resolution in the X-ray and γ-ray bands allowing us to test with real data more advanced physical models.

INTEGRAL is an ESA satellite launched in October 2002 and is devoted to the broad band study of galactic and extragalactic soft γ-ray sources and to diffuse soft γ-ray emission. Due to its improved sensitivity with respect to previous instruments and to its large field of view, the imaging telescope IBIS, on board *INTEGRAL* , is detecting a lot of new compact objects improving considerably our knowledge about their distribution and characteristics, as for example the discovery of a probable new class of highly absorbed X-rays binaries ($N_h > 10^{23}\mathrm{cm}^{-2}$) in star-forming regions (Kuulkers 2004). The second soft gamma-ray catalogue of the IBIS sources, between 20-100 keV, contains 209 objects, the main category is being represented

Figure 1.2: An artist's impression of the INTEGRAL spacecraft. At the front is the SPI instrument with its circular coded mask and behind the square mask of the IBIS instrument. JEM-X, the X-ray monitor, is located between these two instruments with the OMC (Optical Monitoring Camera) to the side. The *INTEGRAL* payload is described in detail in Section 3.

by the galactic accreting binaries (115 sources) (Bird et al. 2004; Bird et al. 2006). Moreover the *INTEGRAL* periodic observations of the galactic plane and in particular of the galactic centre zone (Core Program observations) give the community a large amount of serendipitous data on known and unknown transient X-ray sources.

This thesis presents the work made by the author, in the last three years, that is divided in two main topics:

- the first part concerns the work on transient black hole candidates observed in outburst by IBIS and JEM-X (JEM-X is the X-ray monitor on board *INTEGRAL*). Most of the data belong to core program observations, even if some data have been added to the analysis when they became public. This collection of data resulted in a very good coverage of the outburst of the sources analysed. The source sample is based on black hole transients, or supposedly

black hole transients, observed by *INTEGRAL* in outburst. This sample consists of seven sources, two of them have been chosen for their characteristics and brightness for a more detailed analysis;

- the second part is included in the IBIS survey work and consists of a survey of all the data collected by the wide field cameras (WFC) on board the Beppo Sax satellite. The purpose of this work is to create a mosaic of the images produced by all the WFC data in order to compare the sources found in both the WFC and IBIS mosaics and verify IBIS (and eventually WFC) uncertain detections. This work is concentrated more on persistent sources or sources with long periods of activity with respect to the previous WFC works published in the last years. The SAX WFC are particular useful for this purpose because they had a large field of view (bigger than IBIS), an energy range partially overlapping with IBIS, and an observation strategy that allowed a good coverage of all the sky.

The chapters are structured as follow:

- the second chapter is dedicated to a general introduction on the astrophysical sources of high energy emission;
- the third chapter starts with a short introduction to high energy detectors and techniques and then describes the *INTEGRAL* satellite and its payload;
- the fourth chapter is a general introduction on transient black hole binaries;
- Chapter 5 is dedicated to a summary of the properties of all the transient black hole candidate (or supposed TBHC) observed with *INTEGRAL* in outburst;
- Chapter 6 provides a detailed analysis of the black hole candidate H1743–322 observed by *INTEGRAL* during the 2003 outburst, the first time this source was observed since 1977 by the *HEAO* observatory;

- Chapter 7 describes the *INTEGRAL* and *RXTE* analysis of IGR J17091–3624 discovered by *INTEGRAL* in 2003 during an outburst. This source has been tentatively classified as a black hole candidate due to its spectral shape and variability;

- Chapter 8 is dedicated to the techniques used to obtain the WFC *BeppoSAX* survey and to its results compared to the IBIS survey.

Chapter 2

Galactic and extragalactic objects emitting in high energy bands

The mechanisms of high energy photon emission, in the 20-500 keV range, can be found in several particle physics processes. At these energies the acceleration processes become dominant with respect to thermal emission. These are the most common known processes emitting at high energies:

- non-thermal synchrotron radiation of accelerated electrons in high electromagnetic fields;
- inverse Compton scattering due to the up-scattering of soft photons with high energy electrons;
- thermal bremsstrahlung emission of optical and UV photons produced by decelerated electrons in electric fields;
- electron-positron annihilation, $e^+ + e^- \rightarrow \gamma + \gamma$, a process that releases two photons at 511 keV, the energy of the rest mass of the electron.

- radioactive decay that produces spectral lines at the characteristic energy of the nuclear levels.

All these processes occur in many places in the universe. The principal astronomical objects known to emit in the high energy bands are listed in the following Sections.

2.1 Black-hole candidates, X-ray novae, microquasars

The class of stellar mass black hole (dynamically confirmed and candidates) divides into persistent sources and soft X-ray transients, also called X-ray novae. The persistent sources are mostly high-mass X-ray binaries (HMXB), the prototype being Cyg X-1, while X-ray novae are generally low-mass X-ray binaries (LMXB) (see Chapter 4 for a comprehensive review on X-ray novae). Probably the most characteristic spectral signature of black hole candidates (BHCs) is the hard powerlaw tail that extends to energies greater than 200 keV. The study of outburst phenomena is important since it generally reflects a change in the accretion rate, hence it provides an excellent laboratory to study accretion physics and the formation mechanism of relativistic jets. Figure 2.1 shows different spectral states of the black hole binary Cygnus X-1. Black hole binaries able to generate relativistic jets and accreting matter through an accretion disc are also called microquasars as they appear to be analogues of active galactic nuclei (AGN). In fact both classes of sources share similar geometry and accreting physical processes.

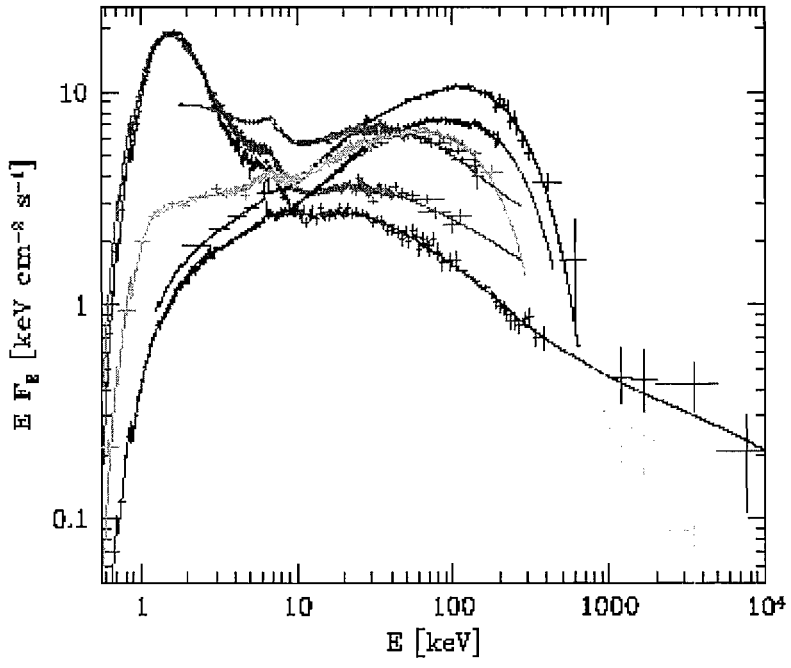

Figure 2.1: Different spectral states of the BH binary Cyg X-1 (Zdziarski et al. 2002).

2.2 Accreting neutron stars

The compact object inside X-ray binaries (either high or low mass) can also be a neutron star. Typical effects of the presence of a neutron star in a binary system are:

- Periodic X-ray pulsations that are present mostly in HMXB systems. This signal originates from the beamed radiation which is produced close to the magnetic poles of the young accreting neutron star with a surface magnetic field of about 10^{12}Gauss. This is due to the misalignment of the magnetic and rotational axes, the neutron star rotation modulates the X-ray intensity in a light-house fashion.

- Type I X-ray bursts – i.e. a sudden and short-lived increase in emission – that are interpreted as thermonuclear explosions at the surface of weakly magnetised neutron stars, and are associated with LMXBs. They typically occur at intervals of hours to several days, and show characteristic spectral changes which are interpreted as photospheric temperature changes during the outburst.

- Type II X-ray bursts that are also a sudden increase in emission but believed to be caused by changes in the viscous properties of the accretion disk or the influence of the neutron star's magnetic field. The profiles of Type II bursts are generally characterized by rapid successions of bursts of a few minutes. Type II bursts have been observed in very few sources.

2.3 Cataclysmic variables

Cataclysmic variables (CVs) are interacting binary systems formed by a white dwarf and a main sequence star companion with a mass $\lesssim 1\ M_{\odot}$. The companion star fills its the Roche lobe and transfers material onto the white dwarf. The classification of CVs is based on the magnetic field strength: if the white dwarf is not highly magnetised, an accretion disk is formed and the material is gradually transported through the disk onto the compact star releasing large amounts of UV and X-ray emission. The accretion through the disc gives rise to thermonuclear explosions, called novae, blowing off the outer layers of the white dwarf envelope. This phenomenon is thought to be recurrent even if the recurrent novae, like RS Ophiuci, are rare.

In the case of highly magnetised white dwarf (polar) the disk is not formed or at least the disk is truncated very far from the white dwarf. The accretion takes place directly into the white dwarf magnetosphere and the system becomes a source of hard X-ray emission.

2.4 Supernovae and Supernovae remnants

Two basic mechanisms have been suggested to account for the large energy release in supernovae explosions. Type I supernova explosions usually occur in binary stellar systems when the secondary star evolves and transfers material to the white dwarf, the mass of which may grow until it reaches a critical point, the Chandrasekhar limit, becoming unstable. This results in a supersonic shock wave (detonation) or a rapid but subsonic combustion (deflagration) or a combination of the two which may destroy the star completely.

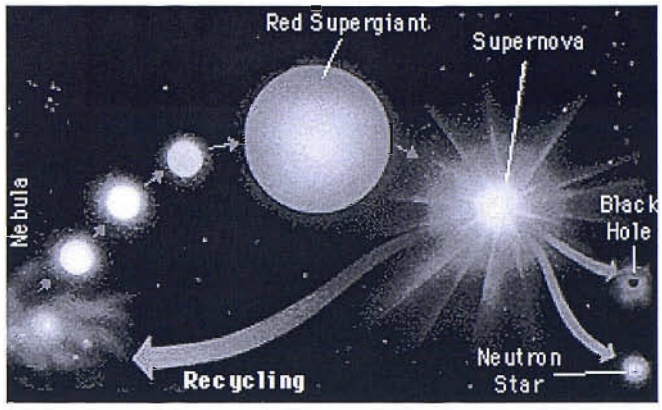

Figure 2.2: Life cycle of a massive star.

The second mechanism of supernova explosion (Type II) consists of the collapse of an iron core of massive stars ($> 8M\odot$); iron is the element that undergoes endoenergetic reactions which lead to a stellar collapse. In the core collapse, the protons capture electrons and therefore neutrons are formed with neutrinos emitted. Such an electron-capture process gives out large amounts of energy, 99% of which is lost through neutrinos, with only 1% responsible for the subsequent explosion. Depending on the progenitor mass, a neutron star or a black hole is often left behind in such a case. The life cycle of a massive star is summarised in the scheme of Figure 2.2. The matter thrown off by the explosion plows through the surrounding gas producing shock waves that create a shell of hot gas and high energy particles, often with a pulsating neutron star inside. Supernova remnants produce intense radiation from radio to the X-ray band and their expanding gas seeds the interstellar medium with heavy elements formed during the supernova explosions. Figure 2.3 shows the ^{44}Ti feature found in the soft γ-ray spectrum of the supernova remnant Cas A.

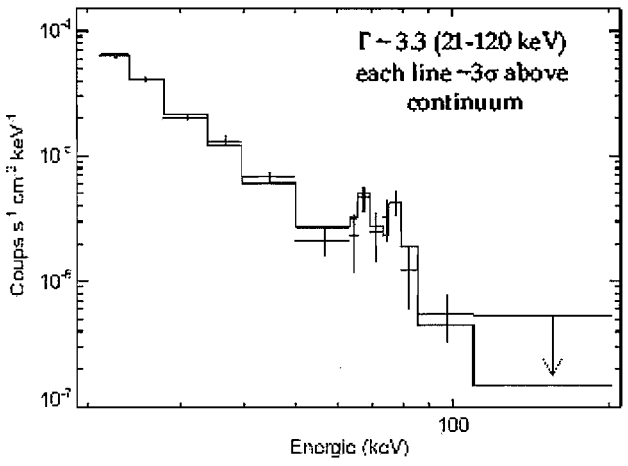

Figure 2.3: *INTEGRAL*/IBIS spectrum of the SNR Cas A. The spectrum shows the 2 ^{44}Ti emission lines at 68 & 78 keV. The continuum spectrum is fitted with a powerlaw with $\Gamma = 3.3 \pm 0.1$ (Renaud et al. 2006).

2.5 Isolated Pulsars

Isolated pulsars are highly magnetised rotating neutron stars that do not accrete matter. They are generally formed during a supernova explosion and their pulsating emission can be detected up to the X- and γ-ray domain. As the prototype of an isolated pulsar, the Crab pulsar shows a pulse shape transition in the hard X-ray to γ-ray domain which indicates the presence of different emission components either thermal or non-thermal. The origin of the hard X-ray emission is thought to be due to neutron star rotation or to an internal heat reservoir following formation. The rotational power manifests itself through the pulsed emission or as nebular radiation produced by the relativistic wind of particles emitted by the neutron star. The residual heat of formation can be observed, in young neutron stars, as soft X-ray emission. Often in a single object it is possible to observe both emission phenomena. Figure 2.4 shows the light curves (in fractions of pulse period) of three pulsars in different energy ranges. As the figure shows, for some pulsars there is a pulsation phase shift between the optical, radio and X-ray bands.

2.6 AGN

Active Galactic Nuclei (AGN) are believed to consist of an accreting supermassive black hole, where the central region is populated by a hot electron corona surrounded by an extended molecular cloud torus. Depending on the viewing angle, different types of AGNs may be observed as Figure 2.5 shows. Most AGNs detected above $\sim$ 50 keV are either blazars (radio-loud AGNs viewed along the relativistic jet), or radio-quiet Seyfert (AGNs without strong jet emission).

Blazars show important flaring activity on timescales of days and less, and obey a characteristic spectral turnover at MeV energies. In the X-/γ-ray domain, blazar emission is generally interpreted as inverse Compton radiation generated by relativis-

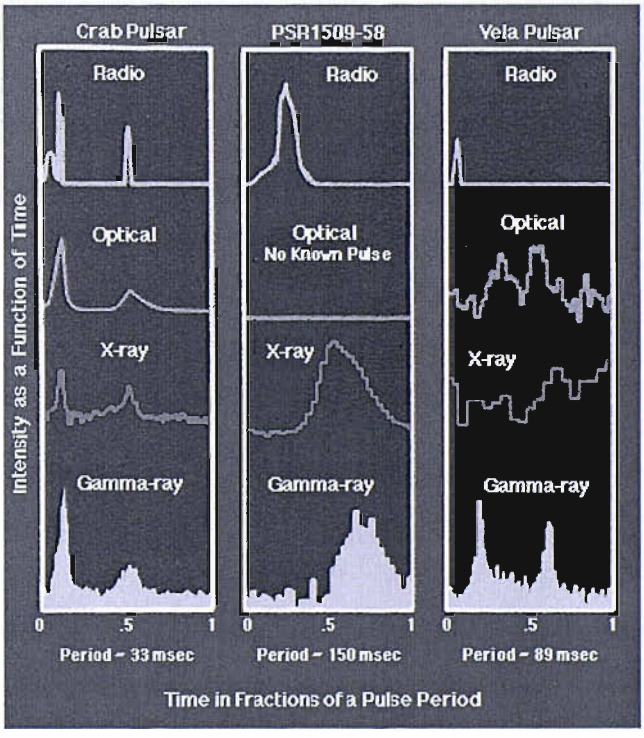

Figure 2.4: The folded light curves of some of the known γ-ray pulsars compared to other energies.

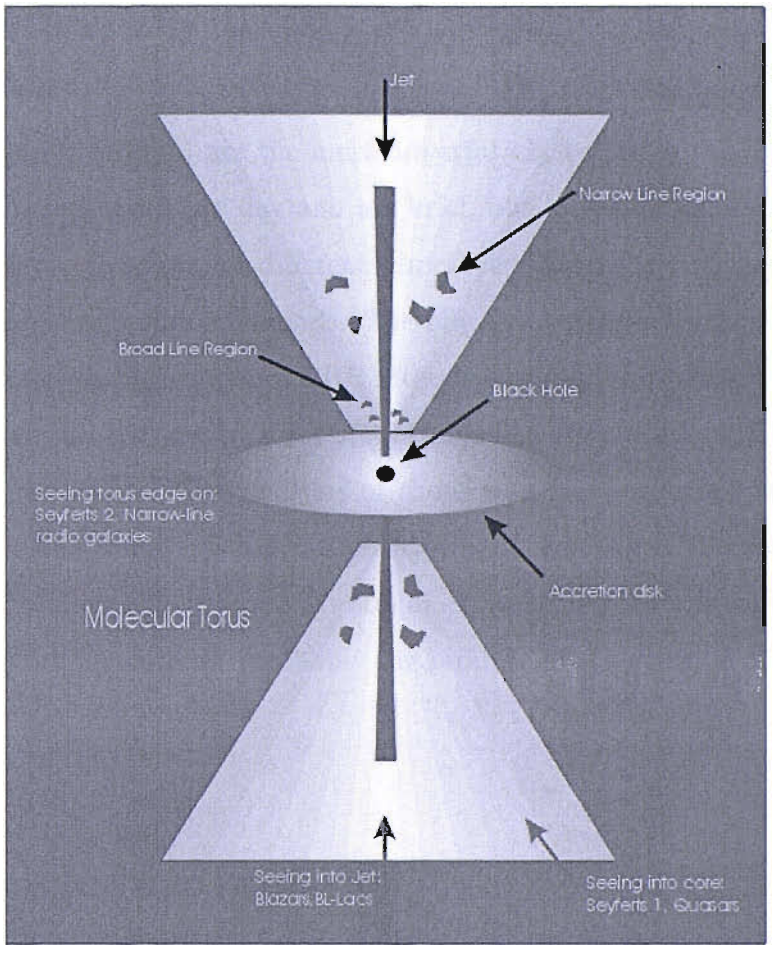

Figure 2.5: A schematic view of unified Active Galactic Nuclei model.

tic electrons on soft photons. A synchrotron component from relativistic electrons and eventually a thermal accretion disk component may contribute.

Radio-quiet Seyferts are generally only detected up to a few 100 keV, showing a thermal Comptonisation spectrum with an exponential cut-off. The emission source is typically located above the surface of the accretion disk, by which it is Compton reflected. However, the origin of the incident primary radiation is much less understood.

2.7 Gamma-ray bursts

Gamma-ray bursts (GRBs) are the most powerful explosions in the Universe, they occur approximately once per day and are brief, but intense, flashes of gamma-ray radiation. They come from all different directions of the sky and last from a few milliseconds to a few hundred seconds. The physical processes that produce GRBs are still unknown. A big sample of GRB afterglows and prompt emission have been detected, in the last decade, by a lot of satellites like *BeppoSAX* , *CGRO* and now *INTEGRAL* and *Swift* . The analysis of these data has permitted to make some hypothesis on their origin: probably the majority of observed GRBs seem to be due to the birth of a black hole in a massive stellar explosion. While a specific subclass of GRBs, the "short " bursts, are probably the product of the collision of two neutron stars.

2.8 Concluding remarks

Compact objects are the most powerful sources of high energy photons above 20 keV. This energy range is largely characterised by the reprocessing of soft radiation due, mostly, to synchrotron radiation or inverse Compton scattering. In Chapter 4 we briefly summarise these processes focusing our attention on a specific case, the subject of this thesis work: the X-ray novae. While in the next Chapter the principal techniques, used in astronomy for γ and X-ray detections, are reviewed.

Chapter 3

The INTEGRAL mission and techniques for γ and X-ray astronomy

3.1 High energy detectors: general properties

The interaction between γ-ray and matter is driven until $\sim$ 100 MeV by three principal processes: The photoelectric effect, Compton scattering and pair production. The relative importance of the different kinds of interaction depends on the atomic number of the material and on the energy of the γ-ray. The principal characteristics of these three processes are briefly summarised as follows:

- **photoelectric absorption** is dominant until $E \lesssim 300$ keV if the atomic number of the detector material is high. Detectors based on photoelectric absorption are proportional counters and solid state detectors;

- **electron-positron pair production** is dominant for energies $E \gtrsim 10$ MeV. Spark chambers can be used as detectors in this range of energy;

- in the intermediate energy range 0.3–30 MeV, **Compton scattering** is the dominant process. This process is used in a particular imaging detector for γ-rays, the Compton telescope that is described in Section 3.2.1.

Figure 3.1 shows a schematic view on how the γ-ray processes vary as a function of atomic number and energy range.

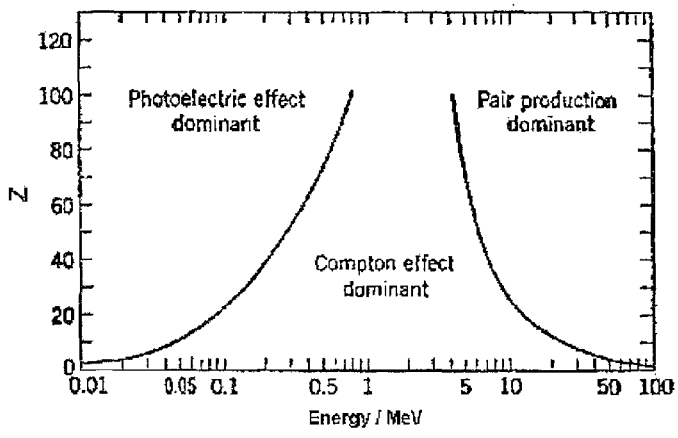

Figure 3.1: γ-ray processes as a function of atomic number and energy.

Generally all detectors for high energy physics (and astrophysics) are based on the same concept: the transfer of all or part of the radiation energy into other forms more accessible to human perceptions (that means essentially, for modern detectors, transform the signal into electrical impulses). This can happen in different ways depending on the detector, its design and the interaction process involved. For example gaseous detectors are designed to directly collect the ionization electrons to form an electric current signal, while in scintillators, both the excitation and ionization contribute to producing molecular transitions which result in the emission of light. The first characteristic that can be considered for a detector is the sensitivity, i.e. the capability of producing a usable signal for a given type of radiation

and energy. Each type of detector is sensitive to a certain type of radiation in a given energy range. The sensitivity depends on several factors, like the cross section and the detector mass that determine the probability that the energy, of the incident radiation, will be converted into ionization of the detector atoms. In order for the signal to be usable, the ionization in the detector has to be greater than a certain minimum amount. This minimum amount is determined by the noise from the detector itself and its electronics.

If the amount of ionization produced by radiation is proportional to the energy losses in the detector, it is possible to provide some information on the energy of the radiation. In general the output signal of electrical detectors is in the form of an electrical pulse (even if there are detectors working with variation of continuous current or voltage), the amount of ionization is then reflected in the electrical charge contained in this signal. The relation between the radiation energy and the total charge or pulse height of the output signal is defined as the response of the detector. For many detectors, the response is linear or approximately linear over a certain range of energies. In general, however, the response is a function of the incident photon energy and particle type, and it does not automatically follow that a detector with a linear response for one type of radiation will be linear for another.

For the measure of the incident radiation spectrum, the most important factor is the energy resolution that is usually given in terms of the Full Width at Half Maximum of the peak (FWHM). This is the extent to which the detector can distinguish two close lying energies, principally given by the fluctuations in the number of ionizations and excitations produced.

Another important factor for the determination of the incident radiation spectrum is the response function. If the response of the detector is linear, the spectrum of pulse heights measured from the detector corresponds directly to the energy spec-

trum of the incident radiation. Unfortunately, a Gaussian peak response is not always realized for most detectors because the interaction between the incident radiation and the detector is not always due to only one process. If the detector is, for example, used to measure a spectrum of gamma rays, the observed pulse height distribution will be a convolution of the gamma ray spectrum and the detector response.

An important characteristic of detectors is the response time. This is the time which the detector takes to form the signal after the arrival of the radiation. This is crucial to the timing properties of the detector. For good timing, it is necessary for the signal to be quickly formed into a sharp pulse with a rise-time as close to zero as possible. In this way a more precise moment in time is marked by the signal. The duration of the signal is also of importance, because during this period, a second event cannot be accepted. This contributes to the dead time of the detector and limits the count rate at which it can be operated.

It is also possible to determine the total detector efficiency that is the ratio between the events registered and the events emitted by the source. This is a function of the detector geometry, the probability of an interaction in the detector and the dead time.

Some detectors are position sensitive, i.e. in conjunction with an imaging system they are able to distinguish different radiations coming from different directions. The imaging capability for this kind of detector is described by three principal factors: the angular resolution that gives a measure on the capability of the telescope to distinguish between two near sources, the point source location accuracy that measures how the instrument is able to determine the real position of the source, and the size of its field of view. The principal characteristics of some high energy detectors most used in astrophysics are summarised in the next Sections.

3.1.1 Gas-filled detectors

This type of detector works on the principle that as radiation passes through a specific gas, ionization of the molecules of the gas occur. Figure 3.2 shows a schematic view of how a gas-filled detector works: when an X- or γ-ray enters the tube an energetic electron pair is created at a single point of photoionization. If a potential is applied across the tube, the positive ions will migrate towards the cathode and the negative ions towards the anode. If the voltage applied to the electrodes is very low the ions can recombine and the current of ions is not proportional to the initial photon energy. On the contrary if the voltage is too high the ions can gain enough energy to interact again with gas atoms or molecules producing more than one interaction. So the output current is proportional to the incident radiation only in a small range of voltages. Gas-filled detectors working in the *proportional regime* are called *proportional counters*. *Geiger counters* work at regimes of higher voltages, while *ionising chamber detectors* work at very low voltage regimes. The proportional counters are mostly used in X-ray astronomy to detect energies between 0.1 and 20 keV. In the *position sensitive proportional counters* the position at which the electrons hits the anode can be estimated using two sets of orthogonal anode wires to define the location of each event.

An array of miniaturised Geiger counters is used to create a position sensitive detector called a spark chamber. Since the Geiger counters are so small this array can track accurately the trajectory of the ions. This kind of detector is very important for γ-ray detection especially if the spark chambers are spaced out with materials that can absorb convert γ-rays into electron-positron pairs.

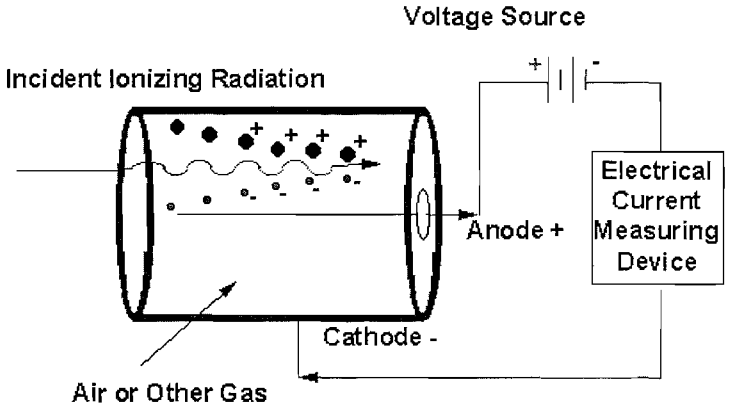

Figure 3.2: Schematic view of a gas-filled detector.

3.1.2 Scintillation detectors

The electrons, released by the primary interaction with the incoming radiation, produce photons inside the crystal and these photons reach the photomultiplier hitting the semitransparent photocathode which liberates photoelectrons. These released photoelectrons are accelerated, focused and multiplied producing a large pulse to the anode. The size of the pulse is proportional to the energy released in the scintillating crystal. For a schematic view of a photomultiplier see Figure 3.3. These devices are often used for cosmic ray telescopes and also for hard X-ray detections above 20 keV. The materials used in scintillation detectors are generally inorganic crystals like *sodium iodide* (NaI), *cesium iodide* (CsI) and *bismuth germanate* (BGO) which has the highest density. Scintillator detectors are often used as active shielding or used as a position sensitive detector using as detector plane a pixelating array of scintillator.

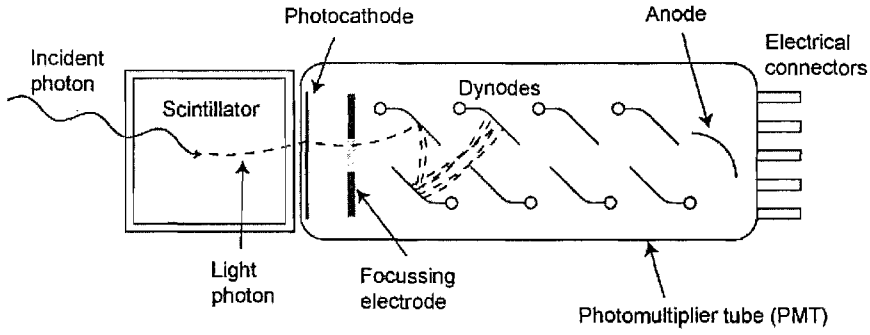

Figure 3.3: Schematic view of a scintillator detector and photomultiplier tube system.

3.1.3 Semiconductor detectors

Semiconductor detectors, as their name implies, are based on crystalline semiconductor materials, most notably silicon and germanium. These detectors are also referred to as *solid state detectors*. The passage of ionizing radiation creates electron-hole pairs which are then collected by an electric field. The average energy required to create an electron-hole pair is 10 times less than that required for gas ionization. They can be used for detecting higher energy radiations than gas-filled detectors, typically from few keV to MeV, because of their higher atomic number and density. The advantage of silicon semiconductors is that they work at room temperature. On the contrary, the germanium ones, even if they are preferred for γ-ray detection due to their higher atomic number, work at low temperatures because of its smaller band gap. A new class of semiconductor detector, working at room temperature, has been developed for γ-ray detection. An example of room temperature semiconductor detector materials are CdTe and CdZnTe, that are especially applied for imaging applications in soft γ-ray astrophysics using, as scintillator detectors, an array of small semiconductors as the detector plane.

3.2 High energy telescopes and imaging astrophysical detectors

An X- and γ-ray telescope works, generally, outside the earth atmosphere and is designed to collect as much information as possible on the incident radiation emitted from a source. It should have the capability to provide information on the position of the sources, on its flux variation and on its energy distribution.

It is not easy to focus a γ-ray photon because it passes through most materials and thus cannot be simply reflected by a mirror like optical photons. Some techniques have been developed in order to overcome these problems, but they depend on the energy range considered. The simplest way to produce a position sensitive detector is to create an array of identical small detectors as detector plane, but the area of a single pixel has construction limits (the space occupied by the electronics, the structure that keeps the pixels together etc..). There are other techniques that can also be used together with an array of detectors that have been developed in order to optimize the imaging capability of a high energy telescope:

X-rays can be reflected from surfaces, but at very small incidence angles. The critical grazing angle (the maximum incidence angle at which reflection can occur), is inversely proportional to the photon energy, so that reflecting high-energy X-rays requires very small incidence angles. This makes designing practical mirrors very difficult. Up to soft X-rays ($\lesssim$ 20 keV), some methods, using multiple reflections, are available to increase the typical reflection angles and permit to focus the X-rays on the detector, as for example, a combination of a paraboloid mirror and an hyperboloid mirror. This solution was used in satellites like *HEAO-2* and now *Chandra*. For gamma-ray observations, two different methods are commonly used: coded aperture masks and Compton telescopes.

3.2.1 Compton Telescopes

Compton telescopes are typically two-layer instruments: in the top layer, the cosmic gamma-ray Compton scatters off an electron in a liquid scintillator. The scattered photon then travels down into a second layer of scintillator material (generally a sodium iodide scintillator) which completely absorbs the scattered photon. Phototubes viewing the two layers can approximately determine the interaction points at the two layers and the amount of energy deposited in each layer. The Compton scattering law provides for a definite relationship between the energy of the scattered photon and the angle between the incoming photon and the scattering electron. The azimuthal direction of the incoming photon is, in principle, not possible to be determined, so the gamma-ray could have come from anywhere in a ring on the sky. Sources can then be identified either by tracking the electron produced in the Compton scattering or by the clustering of the intersection of the cones of each photon at the position of the source.

This kind of detector has a small effective area: typically a geometric area of several thousand cm^2, like in COMPTEL, corresponds to an effective area of a few tens of cm^2). The energy resolution is typically of about 5–10% and it is limited by uncertainties in the measurements of the energy deposited in each layer. Figure 3.4 shows a schematic view on how COMPTEL, the Compton telescope on board NASA Compton Gamma Ray Observatory (CGRO), works.

3.2.2 Imaging with a coded mask telescope

An alternative class of imaging techniques employs straight-line ray optics that offer the opportunity to image at higher photon energies and over larger FOV's (Fenimore & Cannon 1981; Caroli et al. 1987; Skinner 1995). These techniques

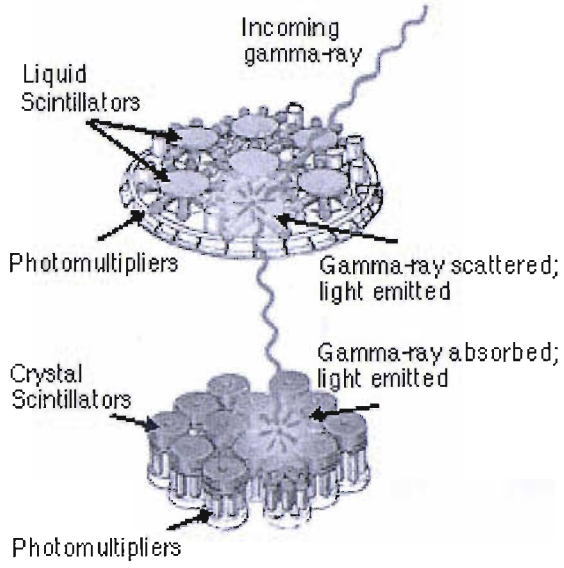

Figure 3.4: COMPTEL (Schronfelder et al. 1993), the imaging telescope on board NASA Compton Gamma Ray Observatory (CGRO), consists of two layers of detectors. A photon is first Compton scattered in one of the upper detector modules and then – in the ideal case – completely absorbed by a detector module of the lower layer. COMPTEL covers the energy range between 1–30 MeV with an energy resolution between 10% at low energies and 5% at the high energies. The instrument had a field of view of one steradian and a location accuracy of about 1^o.

have one common signature: the direction of the incoming rays is, before detection, encoded; the image of the sky has to be reconstructed by decoding the observation afterward (Goldwurm 1995).

This method of producing sky images is a two-step, indirect procedure in contrast to the direct, one-step, imaging procedure of focusing techniques. These alternative techniques are referred to as multiplexing techniques, for which, for equal collecting areas, the sensitivity of a focusing instrument is always better. Multiplexing techniques can be divided into two classes: those based on temporal and those on spatial multiplexing (Caroli et al. 1987).

In a spatial sensitive coded-mask telescope such as IBIS, the imager on board *INTEGRAL* satellite, the imaging system and concept is shown in Fig. 3.5. Every source within the field of view projects a shadow of the aperture onto the detection plane.

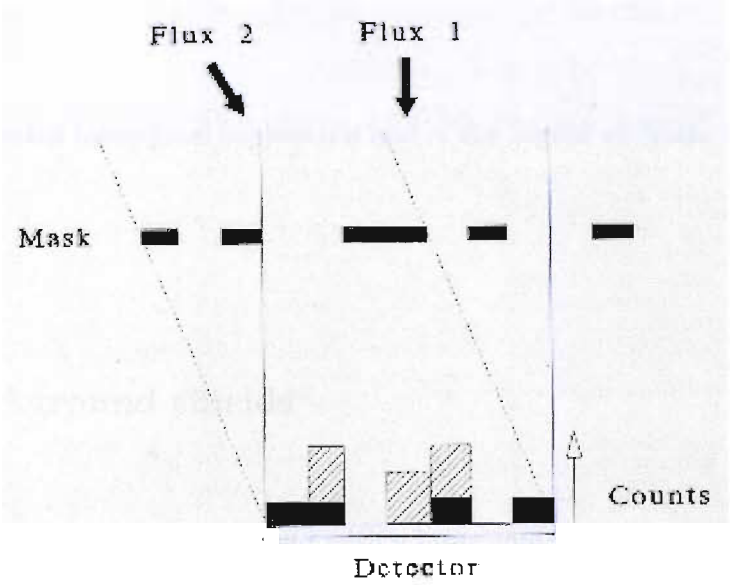

Figure 3.5: Schematic diagram illustrating the working principle of a coded aperture camera: the recorded count rate in each pixel of the detection plane is the summation of contributions from each source flux modulated by the mask.

For any particular telescope geometry, the field of view consists of two different kinds of zones: The Fully Coded Field of view (FCFOV) in which the detected flux is completely modulated by the mask, and the Partially Coded Field of View (PCFOV) in which the detected photons are coded only by a fraction of the mask.

The angular resolution $d\theta$ of a coded mask telescope depends on the ratio between the mask element size, C, and the mask-detector distance, H. Each peak in the deconvolved image has angular extent (FWHM) of approximately the size of C/H.

For point sources and no source confusion, the parameter actually driving the

imaging performance is the Point Source Location Accuracy (PSLA). The theoretical PSLA is limited by the spatial resolution of the detector array.

$$PSLA = \arctan(d/H)/n \tag{3.1}$$

with d the detector inter-pixel separation and n the Signal to Noise ratio (S/N).

3.2.3 Background shields

X and γ-ray detectors have to contend with a large contamination from cosmic rays, that often affect gamma-ray detectors at the same level as the source photons. For this reason a shielding system is often added to high energy telescopes to reduce the amount of background radiation interacting with the detector. There are two principal types of shields used for high energy astronomical telescopes: passive and active. High atomic number materials, like tungsten, are used for passive shielding systems. A passive shield substantially absorbs photons and to a lesser extent charged particles arriving outside the field of view of the telescope, but the absorption efficiency decreases with increasing incident radiation energy. In active shields the radiation is not absorbed, but only detected by a partial energy deposit, so that any simultaneous event in the shield and primary detector can be rejected, because it is assumed to come from outside the telescope field of view. This method does not require that the full energy of the photon is absorbed, so it is also efficient at high energies. The active shields are generally made of scintillator materials as for example BGO.

3.3 The INTEGRAL mission

INTEGRAL is the second ESA γ-ray mission (the first was COS-B launched in 1975). It is a medium size mission conceived as part of ESA's Horizon 2000 programme. The spacecraft has been developed in parallel for two ESA missions: *INTEGRAL* and *XMM-Newton*. *INTEGRAL* was launched by a 4-stage PROTON from Baikonur in Kazakhstan on 17^{th} October 2002. *INTEGRAL* was inserted into a geosynchronous highly eccentric orbit with high perigee in order to have long periods of uninterrupted observation with nearly constant background. *INTEGRAL* is a major milestone in hard X-ray and low energy gamma-ray astronomy after the successful missions of SIGMA on GRANAT (France/USSR) and the Compton Gamma-Ray Observatory (NASA). In fact the instruments of its payload cover a wide energy range in the hard X-rays and soft gamma-rays bands (15 keV – 10 MeV) and achieve a sensitivity, an energy and angular resolution an order of magnitude better than the CGRO. It fills a gap which was neither covered by SIGMA nor CGRO. Comparison with SIGMA shows a major advance, with an improvement in continuum sensitivity that is considerably more than one order of magnitude between 100 keV and 1 MeV, and the narrow line sensitivity is increased by nearly two orders of magnitude. The table in Figure 3.6 shows the performances of the last decade of γ-ray missions compared with the *INTEGRAL* ones.

INTEGRAL scientific goals are attained by fine spectroscopy with imaging capability and accurate positioning of celestial sources. Fine spectroscopy over the entire energy range permits spectral features to be uniquely identified and line profiles to be determined for physical studies of the source region.

The fine imaging capability within a large field of view permits an accurate location and hence identification of the gamma-ray emitting objects with counterparts at other wavelengths. It provides considerable serendipitous science which is very

important for an observatory-class mission.

3.3.1 Observations and goals

3.3.1.1 Observing Programme

Most of the observing time, from 65% of the total time in the first year to 75% for subsequent years, is devoted to the scientific community. Typical observations last from 100 ks up to about two weeks. Proposals for observations are selected on their scientific merit only by a single Time Allocation Committee. These selected observations form the basis of the General Programme.

The remaining fraction of the total observing time is the Core Programme (Winkler 2001), reserved for scientific institutes which have developed and delivered instruments and for the data centre (guaranteed PI time). During the nominal period of the mission, the Core Programme consists of three parts with a dedicated exposure time per year:

- Frequent scans of the galactic plane (Galactic Plane Survey, GPS): these scans provide a periodic monitor of the gamma-ray sky to search for transient sources and monitoring the persistent ones. The scans are performed weekly with a "slew and stare " manoeuvre of the spacecraft along the seasonally visible part of the galactic plane within a galactic latitude of $\pm 10°$.
- Deep Exposure of the galactic central radian (Galactic Central Deep Exposure, GCDE): has the aim of mapping line emission and diffuse emission of the central galactic region and to perform deep imaging and spectroscopic studies of the galactic bulge and of the single point sources around the galactic centre zone.

	OSSE	COMPTEL	EGRET	BATSE	SIGMA	HEAO-3	BeppoSAX PDS	INTEGRAL (at MPVR)
Energy range (MeV)	0.05 – 10	0.7 – 30	20 - 30000	0.03 - 1.9	0.035 - 1.3	0.05 – 10	0.015 - 0.3	0.004 – 10 (JEM-X, SPI, IBIS)
Energy resolution	5 - 12%	4 - 15 %	~20 %	20 - 32%	8 - 16%	0.2% at 1.8 MeV	12% at 0.1 MeV	0.16 % at 1.8 MeV (SPI)
Position Localization	10 arcmin	0.5-1 deg	<10 arcmin	1 deg	~1 arcmin	None (spin-frequency: 1/20min)		< 1 - 1.5 arcmin (IBIS)
Field of View	3.8 x 11.4 deg	1 steradian	0.6 steradian	Earth occultation	4.7 x 4.3 deg fully coded	30 x 30 deg	1.3 deg (hexagonal)	16 deg fully coded (hexagonal, SPI)
Narrow line sensitivity 3σ (photon cm^{-2} s^{-1}) in 1 Msec	$7\ 10^{-5}$ (1) @ 1 MeV	$5\ 10^{-5}$ (1) @ 1 MeV	n.a.		~$8\ 10^{-4}$ (3) @ 511 keV	~$2\ 10^{-4}$	-	$2.4\ 10^{-5}$ (1) @ 1 MeV (SPI)
Continuum sensitivity 3σ (photon keV^{-1} cm^{-2} s^{-1}) in 1 Msec	$2\ 10^{-7}$ (2) @ 1 MeV $5x10^{-7}$ @ 0.1 MeV	$1.7\ 10^{-7}$ (2) @ 1 MeV	$5\ 10^{-8}$ >100MeV	~2 10E-3 (3) 25 – 35 keV	$7\ 10^{-6}$ @ 0.1 MeV	~$1\ 10^{-5}$ (7) entire survey @ 0.1 MeV	$7\ 10^{-7}$ (10) @ 100 keV	$5\ 10^{-7}$ @ 1 MeV (IBIS)
Operation	1991-2000	1991-2000	1991-2000	1991-2000	1989-1998	1979-1981	1996-2002	2002-->

Figure 3.6: Last decade γ-ray missions performances compared with the *INTEGRAL* performance after 6 months of operations.

- Target of opportunity (ToO), pointed observations of selected sources.

One of the key investigations of the *INTEGRAL* Core Program is mapping the soft gamma-ray sky with particular interest in the galactic plane regions of the galaxy from 20 keV up to 1 MeV.

Within the new Key Program strategy, started after the mission extension, only specific interesting zones of the galactic plane, not covered enough, will be the target of observations.

3.3.1.2 Observing modes

In order to minimize systematic effects taking place in the the two main instruments, SPI and IBIS (see Section 3.4) due to spatial and temporal background variations, a controlled and systematic spacecraft dithering manoeuvre is required.

This manoeuvre consists of several off-axis pointings of the spacecraft pointing axis from the target in steps of 2 degrees. The integration time for each pointing could vary in the range 0.5–1 hour and time is adjusted in a way so that always multiples of a complete dither pattern are executed for each observation. Two main, different pointing patterns are currently used:

- Hexagonal dither pattern: this consists of a hexagonal pattern around the nominal target location (1 source on-axis pointing, 6 off-source pointings, each 2 degrees apart).
- Rectangular, or 5×5, dither pattern: this consists of a square pattern around the nominal target location (1 source on-axis pointing, 24 off-source pointings, each 2 degrees apart).

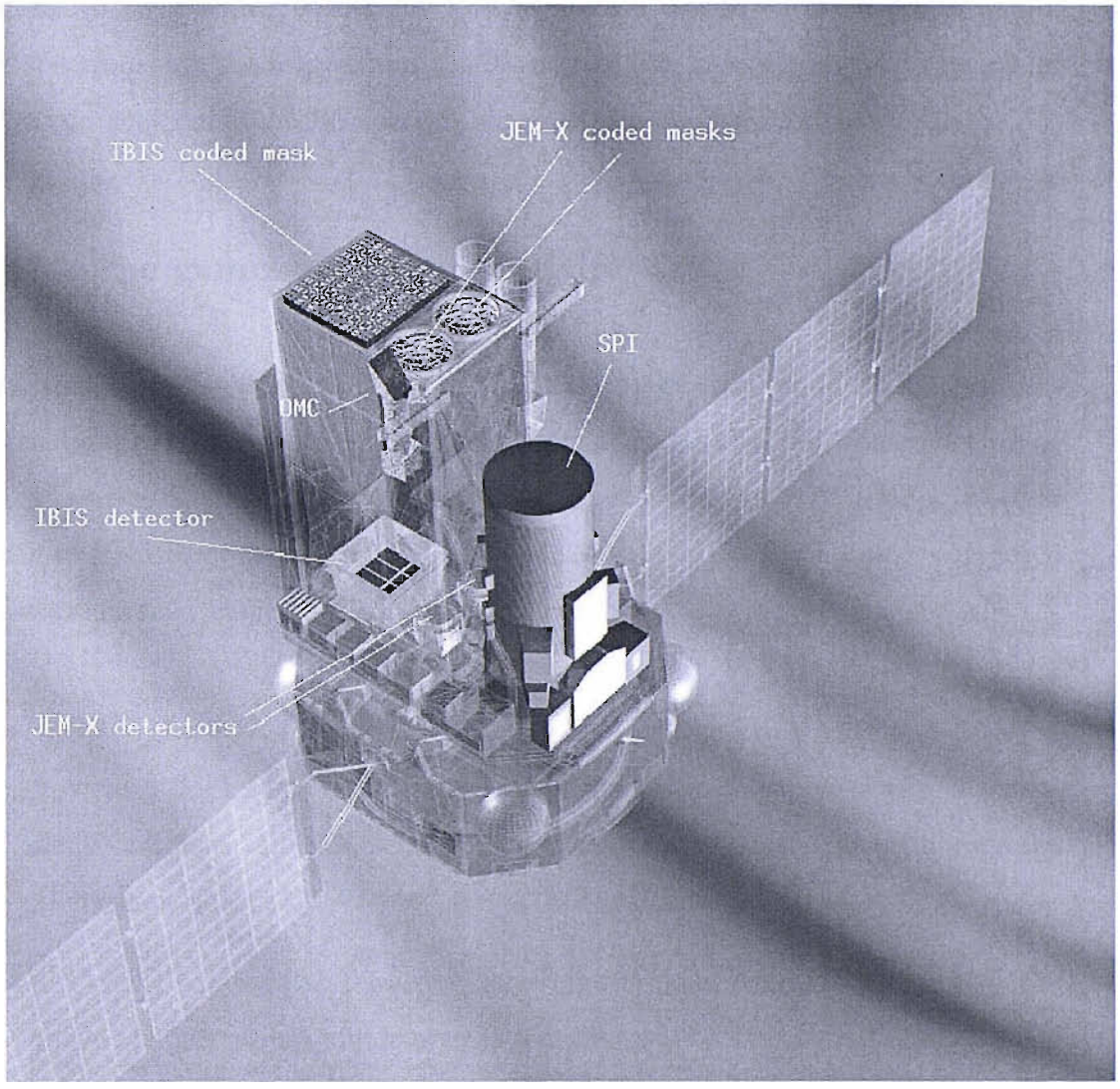

Figure 3.7: An *INTEGRAL* payload modules view.

3.4 Gamma-ray telescopes on-board INTEGRAL

The two main gamma-ray instruments, integrated in the *INTEGRAL* payload (Fig. 3.7), have both spectral and angular resolution, but they are differently optimised

in order to complement each other and to achieve overall excellent performance. The spectrometer, the imager and the X-ray monitor have a common principle of operation: they are all coded aperture mask telescopes (see Section 3.2.2).

3.4.1 The gamma-ray imager IBIS

IBIS, Imager on Board the *INTEGRAL* Satellite (Ubertini et al. 2002), provides diagnostic capabilities of fine imaging (12 arcmin Full Width Half Maximum). The source location accuracy is of 30 arcsec for strong sources, the FOV is $19° \times 19°$ (Full Width to Half Response) with a FCFOV of $9° \times 9°$. The detection unit is composed of two gamma-ray cameras separated by 10 cm:

- ISGRI (*INTEGRAL* Soft Gamma-Ray Imager), covering the range from 15 keV to 1 MeV, has a detection plane made of 16384 physically independent cadmium telluride semiconductor crystals organized in eight modules (Lebrun et al. 2003).
- PICsIT (Pixilated CsI Telescope) covering the range from 170 keV to 10 MeV, made of 4096 cesium iodide crystal scintillators (Di Cocco et al. 2003).

Photons are detected by IBIS in three modes: detection on ISGRI, detection on PICsIT, and detection on the two layers (Compton mode). Table 3.1 shows the principal IBIS scientific capabilites.

Two anti-coincidence shields protect the detector from external radiation:

- a tungsten passive shield composed by an "hopper " unit (truncated pyramid on the top of the ISGRI detector) and a "tube " made of four walls closing the

aperture down to the hopper level. The passive shielding is designed to reduce the celestial diffuse background component; it becomes transparent above 200 keV;

- an active anti-coincidence shield, the VETO anti-coincidence system is composed of 16 independent modules, each made with two large BGO crystals. This ensures a substantial reduction of the background due to the induced photons and hadronic component, enhancing the detector sensitivity. Measured over the whole energy range, the VETO system provides a background suppression effect of $\sim 50\%$ for ISGRI and $\sim 40\%$ for PICsIT.

The basic design of the IBIS mask (Figure 3.9 top) is a Modified Uniformly Redundant Array (MURA)[1] of 53×53 elements. This pattern, reiterated four times and cut on the borders, provides the IBIS mask of 95×95 individual square cells. Half of them are in tungsten (16 mm thickness) offering a 70% opacity at 1.5 MeV; the other half are opened and covered by a carbon fibre with an off-axis transparency of 60% at 20 keV.

The FCFOV size, for which sensitivity is the nominal one, is $9° \times 9°$; it becomes then 50% at 19°, and response decreases to zero at 29°. The angular resolution is $d\theta = \arctan(C/H) = 12'$ with $C = 11.2$ and $H = 3133$ mm

3.4.1.1 ISGRI spectral capability

Each pixel of the ISGRI camera is a spectrometer chain with its own characteristics. The spectral performance of the camera depends therefore critically on the alignment of the pixel gains and offset. The alignment is performed in two steps: the electronics allow for a rough alignment and then a fine software correction must be applied.

[1]For design and properties of MURA pattern, see Gottesman & Fenimore (1989)

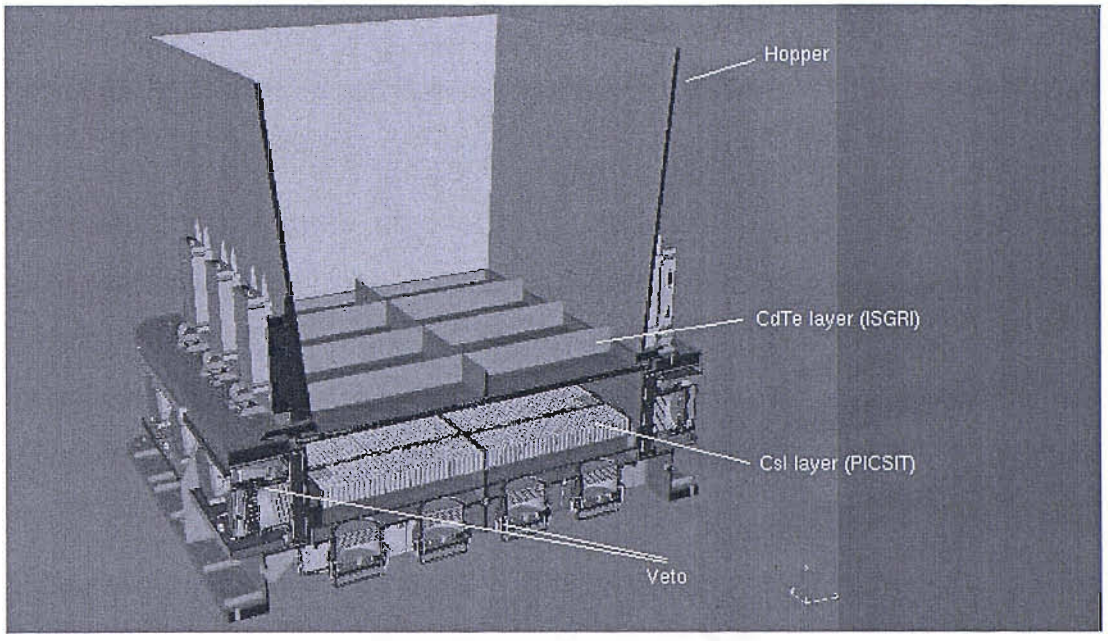

Figure 3.8: Scheme of IBIS detectors and shielding system.

In principle, the amplitude of the pulse yields the energy of the incident photon. However, above 60 keV the energy is a function of both pulse height and rise time, because of the charge trapping inside the CdTe material. The longer the rise time, the more important are the charge losses. In order to determine the energy for each photon, raw data are corrected on-ground using Look Up Tables (LUTs) carried out by calibrations. In addition, the resulting line profile is no longer a Gaussian, but more similar to a Lorentzian. ISGRI energy resolution (Tab. 3.1) depends on the operating temperature, and also on the bias voltage.

3.4.2 The spectrometer SPI

The spectrometer SPI (SPectrometer on *INTEGRAL*) provides spectral analysis of gamma-ray point sources as well as extended sources over an energy range between 20 keV and 8 MeV.

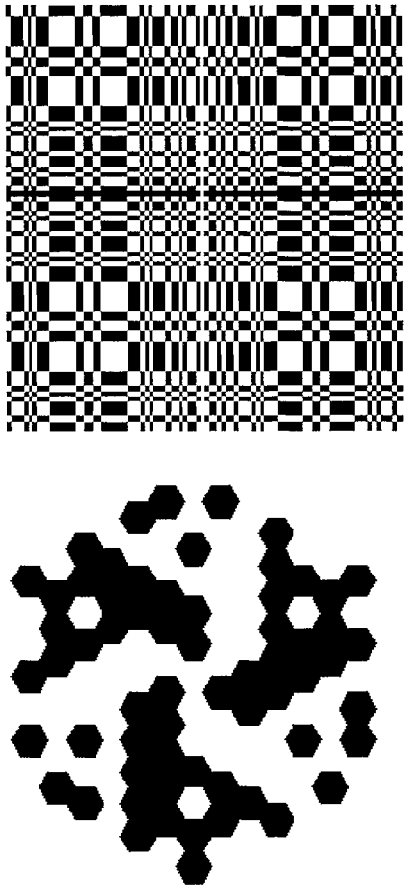

Figure 3.9: IBIS and SPI coded mask patterns

Table 3.1: An overview of the IBIS scientific capabilities.

Energy Range	15 keV–10 MeV
Continuum sensitivity, at 3σ and 10^6 s integration (ph cm^{-2} s^{-1} keV^{-1})	2.3×10^{-6} @ 100 keV 1.6×10^{-6} @ 1 MeV
Line sensitivity, at 3σ and 10^6 s integration (ph cm^{-2} s^{-1})	1.8×10^{-5} @ 100 keV 3.8×10^{-4} @ 1 MeV
Energy Resolution (FWHM %)	8% at 100 keV ISGRI 10% at 1 MeV PCSIT
Angular resolution (FWHM)	$\sim 12'$
Point Source Location Accuracy (90 % error radius)	30" @ 100 keV (50 σ source) 3' @ 100 keV (5 σ source) 5'-10' @ 1 MeV (5 σ source)
Timing accuracy	61 μs - 1 hr
Field of View	$9°\times9°$ (fully coded) $29°\times29°$ (zero response)

The field of view is 16 degrees with an angular resolution of 2 degrees. The SPI detector is composed of an array of 19 hexagonal high purity germanium detectors. Table 3.2 summarises the principal SPI scientific capabilites. Emission lines from radioactive nuclei, such as ^{26}Al, are some of the main observational subjects of the spectrometer SPI.

The SPI Mask, (Figure 3.9 bottom) placed 1.7 m above the 19 germanium detectors, is a Hexagonal Uniformly Redundant Array (HURA) made up of 127 hexagonal cells of which 63 are opaque to the radiation (95 % opaque @ 1 MeV) and 64 are transparent to gamma-radiation (60 % transparent @ 20 keV & 80 % transparent

@ 60 keV). The pattern has a 120° symmetry and the cells are of size 60 mm side-to-side (i.e. short axis) by 67.55 (i.e. long axis) forming a hexagonal-shaped coded area of overall dimensions 692.72 mm (i.e. short axis) by 770 mm (i.e. long axis). The opaque elements are made of 3 cm thick tungsten.

Table 3.2: An overview of the SPI scientific capabilities.

Energy Range	20 keV – 8 MeV
Continuum sensitivity, at 3σ and 10^6 s integration (ph cm^{-2} s^{-1} MeV^{-1})	1.5×10^{-4} @ 1MeV
Line sensitivity, at 3σ and 10^6 s integration (ph cm^{-2} s^{-1})	5.1×10^{-6} @ 1MeV 2.8×10^{-5} @ 511 keV
Energy Resolution (FWHM %)	2.33 keV @ 1.33 MeV
Angular resolution (FWHM)	$\sim 2.0°$
Timing accuracy (3σ)	0.129 ms
Field of View	16° (corner to corner) (fully coded)

3.4.3 Monitors for counterparts: JEM-X and OMC

The JEM-X monitor (Lund et al. 2003) works simultaneously with the other instruments in the energy range between 3 and 35 keV and with an angular resolution of one arcmin and a FCFOV of 4.8 °. The coded mask is placed 3.4 m above the detector. The detector consists of two identical chambers filled with Xenon at a pressure of 1.5 bar (see Table 3.3).

The Optical Monitoring Camera (OMC) is a CCD detector of 1024 × 1024 pixels located in the focal plane of a 50 mm lens with a Visible (V) filter (Mas-Hesse et al. 2003).

The size of each pixel is 13 × 13 μm covering a field of 17.6 x 17.6 arcsec. The total field of view of the OMC camera is of 5 × 5 degrees. The camera is placed on top of the satellite and is sensitive to stars of magnitude up to about 18.

Table 3.3: An overview of the JEM-X scientific capabilities.

Energy Range	3 keV–35 keV
Continuum sensitivity, at 3σ and 10^6 s integration (ph cm^{-2} s^{-1} keV^{-1})	1.3×10^{-5} @ 6 keV
Line sensitivity, at 3σ and 10^6 s integration	1.7×10^{-5} (ph cm^{-2} s^{-1}) @ 6keV
Spectral Resolution	1.2 keV @ 10 keV
Angular resolution (FWHM)	$\sim$ 3 arcmin
Point Source Location Accuracy	$<$ 30" (10 σ source)
Timing accuracy (3σ)	122 μs
Field of View	4.8° (fully coded)

3.5 Summary

INTEGRAL's combination of wide energy range with high spectral resolution, imaging capability and consequently higher sensitivity with respect to previous X and γ-ray satellites, permits astronomers to measure detailed spectra and overcome most source confusion limits. This, together with the observational strategy, consisting of frequent scans of the galactic plane, permit an accurate monitoring of galactic hard X-ray transients. The wide FOV also increases the chance of serendipitous detections of new transient sources. Spectral and imaging analysis of IBIS data of a sample of these transients is the basis of the work presented in the next Sections.

Chapter 4

Introduction to X-ray Novae

4.1 X-ray Binaries

X-ray binaries are systems in which a compact object and a stellar companion orbit each other at a distance small enough to enable mass transfer from the companion star onto the compact object; this phenomenon is one of the powerful galactic sources of X-rays. The companion star is, generally, a main sequence star while the compact object is a collapsed star that could be a black hole (BH), or a neutron star (NS). The latter can be immediately identified if X-ray pulses (due to neutron star rotation) or bursts (resulting from explosions of accumulated gas) are observed. Anyway the decisive criterion allowing us to distinguish between the two types of compact objects is the mass measurement. All neutron star masses are theoretically expected to not exceed $\approx 3M_{\odot}$ (Rhoades & Runi 1974).

Especially for weak sources, it is not easy to understand if an X-ray binary system contains, as compact object, a weakly magnetized NS or a BH. The principal reason is that the physical processes involved in the accretion are the same

in both cases. In fact the mass of the compact object has been measured precisely enough to prove the presence of a black hole only in about 18 X-ray binaries (McClintock & Remillard 2003). When the mass of the accreting object cannot be determined, other criteria have to be applied, either based on the spectral shape or timing analysis (Rutledge et al. 2000); (Titarchuk et al. 2005); there are about 22 sources classified as black hole candidates that are listed in Table 4.1 (Psaltis 2004). On the other hand there are major differences between NSs and BHs that should imply certain differences in their radiation spectra. NSs have real surfaces whereas BHs have horizons, which represent the complete absence of a physical surface. The characteristic magnetic field present in NSs would also be expected to mark a distinction. Nonetheless, up to now, no one has succeeded in predicting the spectral differences only from theoretical considerations.

Recently, on the basis of the correlation between Quasi-Periodic Oscillations (QPO) and the spectral index, Titarchuk et al. (2005) argued a probable signature of the presence of a NS rather than a BH.

Among accreting binary systems we observe both persistent and transient sources. In the former (e.g. Cygnus X-1 and LMC X-3) strong X-ray emission is observed continuously, while the latter (e.g. GX 339-4) exhibit short periods of intense emission (outbursts) and periods of quiescence.

4.1.1 The Compact Objects

At the end of stellar evolution, the core of the star runs out of nuclear fuel, and it collapses until other forms of pressure support new equilibrium configurations. The possible configurations are are thought to be: white dwarfs, neutron stars and black holes.

Table 4.1: Candidate black hole binaries from Liu et al. (2000), Liu et al. (2001) and Bird et al. (2005).

Source	RA(2000)	DEC(2000)	Type
1354–645 (BW Cir)	13 58 09.74	–64 44 05.2	T,U, BHC
1524–617 (KY TrA)	15 28 16.7	–61 52 58	T,U,BHC
4U 1630–47	16 34 01.61	–47 23 34.8	LMXB,T,U,D,BHC
XTE J1650–500	16 50 01.0	–49 57 45	LMXB,T, BHC
IGR J17091–3624	17 09 06.0	–36 24 39.0	T,BHC?
SAX J1711.6–3808	17 11 37.1	–38 07 06	
GRS 1716–249 (Nova Nuscae)	17 19 36.93	-25 01 03.4	LMXB, T, BHC
XTE J1720–318	17 19 59.06	–31 44 59.7	LMXB, T, BHC
KS 1730–312	17 33 37.6	–31 13 12	T,BHC
GRS 1737–31	17 40 09	–31 02.4	T,BHC
GRS 1739–278	17 42 40.03	–27 44 52.7	LMXB, ,BHC
1E 1740.7–2942	17 43 54.88	–29 44 42.5	BHC
IGR J17464–321 (H 1743–322)	17 46 15.61	-32 14 00.6	LMXB,T, BHC
SLX 1746–331	17 49 50.6	–33 11 55	U,BHC
XTE J1748–288	17 48 05.06	–28 28 25.8	T, BHC
XTE J1755–324	17 55 28.6	–32 28 39	T, BHC
1755–338 (V4134 Sgr)	17 58 40.0	–33 48 27	LMXB, T,U,BHC
GRS 1758–258	18 01 12.67	–25 44 26.7	LMXRB, U, BHC
EXO 1846–031	18 49 16.9	–03 03 53	T,BHC
XTE J1901+014	19 01 41.00	+01 26 18.5	T,BHC?
XTE J1908+094	19 08 53.08	+09 23 04.9	LMXB, T,BHC
1957+115 (V1408 Aql)	19 59 24.0	+11 42 30	U,BHC?
XTE J2012+381	20 12 37.70	+38 11 01.2	T,BHC
IGR J17285-2922	17 28 30.00	–29 22 00.0	T,BHC?
IGR J18539+0727	18 53 54.00	+07 27 00.0	T,BHC?

Even if the processes are not completely understood, the problem can be understood considering the range of masses which these "dead stars " can have. In white dwarfs and neutron stars, the pressure that holds up the star is the quantum mechanical pressure associated with the fact that electrons and protons are fermions and only one particle is allowed to occupy any one quantum mechanical state. White dwarfs are held up by *electron degeneracy pressure*, and can have a mass lower than about 1.4 $M_{\odot}$. White dwarfs are the end product of the low-mass stars that are not heavy enough to generate the core temperatures required to fuse carbon in nucleosynthesis reactions.

Neutron stars are the end products of Type II supernova explosions of massive stars (range $\sim$ 10–20 $M_{\odot}$). They are produced by the rapid neutronization of degenerate cores, a process that releases explosive energy leading to a supernova. At the end of this process the core contains a degenerate gas of neutrons except for a few percent of protons and electrons (1%). So, the force that supports a neutron star against collapse is the degeneracy pressure of neutrons. The neutron star masses range from 1.3 $M_{\odot}$ to 3 $M_{\odot}$ with a range of radii of 10 Km $\leq$ R_{NS} $\leq$ 20 Km. Because of its small size and high density, a neutron star possesses an extremely high surface gravitational field and often a high magnetic field.

Based on the calculations of Schwarzschild (1916), general relativity predicts that a black hole is a region formed in a further collapse of a neutron star of mass higher than 3 $M_{\odot}$, that cannot communicate with the external universe because the escape velocity exceeds the speed of light (Shapiro & Teukolsky 1983).

The escape velocity from the surface of a star of mass M and radius r can be obtained through classical calculations: $v = (2GM/r)^{1/2}$. If we set v as the speed of light (c) the radius of such a star would be $r = 2GM/c^2$. This is the so-called *Schwarzschild radius*, $r_{\rm Sch}$, of a black hole of mass M. The boundary of the region

is called the event horizon. The only three properties of a black hole that can be externally detected are mass, spin and electric charge (see a review in Longair 1997). An accreting binary system containing a white dwarf as a compact object is mostly classified, for its emission properties, as a cataclysmic variable (see Chapter 2).

4.1.2 Classification and distribution in the sky

A compact object in a binary system accreting mass from its companion in a stable phase is characterised mostly on the mode of mass transfer, the ratio of the mass of the two objects and their orbital separation. Over 90% of the strong galactic X-ray sources appear to fall into two distinct groups: the high-mass X-ray binaries (HMXBs) and the low-mass X-ray binaries (LMXBs). These two groups differ in a number of physical characteristics.

In the case of a LMXB the companion star has a small mass, less than the one of the compact object ($M \leq 2\ M_{\odot}$). The accretion of matter is due to direct mass transfer through the inner Lagrangian point. This happens only when the companion fills its Roche lobe. The mass lost through the Lagrangian point reaches the compact object via an accretion disc. In such systems the mass is driven by angular momentum losses due to gravitational radiation (for small masses and orbital separations) and magnetic braking (for orbital periods ≤ 2 day) or by the evolution of the companion star (for orbital periods ≥ 2 day). In these systems the low-mass companion is a late-type star, which cannot be detected easily in optical wavebands. So, the determination of the masses of the components is not possible in most cases. Among the low-mass companion stars we find white dwarfs, late-type main-sequence stars, A-type stars and F-G-type sub-giants. The orbital periods vary between 0.2–400 hours. LMXBs show X-ray bursts in many cases, but regular X-ray pulsations in a very few cases. This implies that the neutron stars in this kind of system are

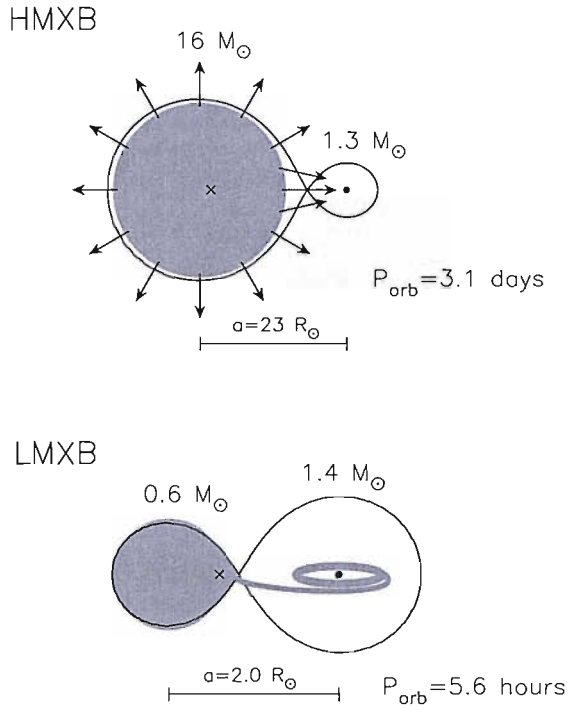

Figure 4.1: Examples of a typical HMXB (top) and LMXB (bottom). The compact object (in this case a neutron star) in the HMXB is fed by a strong high-velocity stellar wind. The compact object in an LMXB is surrounded by an accretion disc which is fed by Roche lobe overflow.

often weakly magnetised. The LMXB are concentrated around the galactic centre zone and the globular clusters.

A compact object can also accrete matter from a companion star that does not fill its Roche lobe, which is the case of High Mass X-ray Binaries (HMXBs). Here the companion star loses mass in the form of a stellar wind. This process is important and produces high X-ray emission only if the companion star is massive ($\geq 10\ M_{\odot}$) because only in this case can it drive a strong stellar wind. The accretion disc is probably not present except in particular cases. These sources contain early-type stars (generally O or B type) as companions. In the optical wavebands their spectrum is dominated by the companion star. Conventionally HMXBs can be further divided into two subgroups: those in which the primary is a Be star (Be/X-

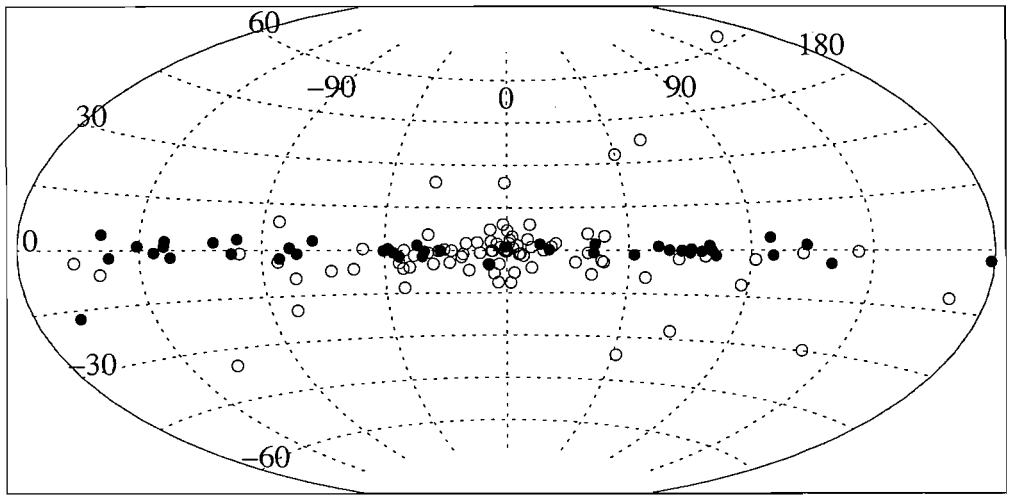

Figure 4.2: Distribution of Low-Mass X-ray Binaries (open symbols) and High Mass X-ray Binaries (filled symbols) in galactic coordinates (Grimm et al. 2002)

ray binary) and those in which the primary is a supergiant. The majority of the known high-mass X-ray binaries are Be/X-ray systems. Most Be/X-ray binaries have relatively wide orbits with moderate eccentricity and their compact companions spend most of their time far away from the disc surrounding the Be stars and their X-ray spectra are usually hard.

In the second group of HMXB systems, the compact star orbits a supergiant early-type star, deep inside the highly supersonic wind. The X-ray luminosity is either powered by pure stellar wind accretion or, in some cases (the brightest systems) also Roche-lobe overflow via an accretion disc. They form a young stellar population (age $< 10^7$ yrs). They contain a bright secondary component, which can be easily detected. The orbital period of this kind of system and the mass of each component, as well as the average radius of the companion star have been detected in the majority of these systems (Psaltis 2004). Figure 4.1 shows a simple accretion scheme of HMXB and LMXB respectively.

From the observations over the past decade, there are about 300 bright X-ray sources included in X-ray catalogs (Liu et al. 2000; Liu et al. 2001). Studying the galactic sources, Grimm et al. (2002) found significant differences in the 3D spatial distribution of HMXBs and LMXBs in our Galaxy as is shown in Fig. 4.2 (in good agreement with theoretical expectations and earlier results – White & van Paradijs 1996). Whereas HXMBs are more concentrated towards the galactic plane with a vertical scale height of 150 pc, and clear indications of a distribution following the spiral structure, LMXBs have a strong tendency to concentrate towards the galactic bulge and their vertical distribution has a scale height of 410 pc.

All these properties confirm the fact that LMXBs are old systems with age $\sim (5-15)\times 10^9$ yrs (White & van Paradijs 1996). The classification as LMXB is mainly based on the spectra obtained from an optical identification, on the mass function or by the presence of bursts. If none of those is available, a classification may be inferred based on the similarity of the X-ray properties to other identified systems. A recent work based on data collected by the *INTEGRAL* satellite (Dean et al. 2005) confirm the previous results on angular distribution of high and low mass XRBs

4.2 Transient X-ray binaries (X-ray novae)

Transient sources are characterised by long periods of X-ray inactivity, lasting months to decades, that are interrupted by short outbursts, during which their X-ray brightness increases by several orders of magnitude.

Tanaka & Shibazaky (1996) define X-ray Novae (XN) as LMXBs where a compact object accretes matter, at a very low rate, from a late-type companion star. Of the sources present in the X-ray catalogs, more than half of them are LMXBs, and are classified as transient sources. The principal hallmarks of an X-ray nova include

both the discovery of the source during a violent outburst and a very large ratio of maximum to minimum X-ray intensity. Recurrent eruptions have been observed for several X-ray novae as for example, H1743–322 in 1977 and 2003; 4U 1543–47 in 1971, 1983, 1992 and 2002; 4U 1630–472 and GX 339–4 at $\sim 1-2$ year intervals. Most X-ray novae, however, have been observed to erupt only once. Nevertheless, all X-ray novae are thought to be recurrent, with cycle times as long as several centuries or more.

Most of the transient XN are associated with confirmed black hole binaries (BHB) or black hole Candidates (BHC) (McClintock & Remillard 2003).

Because of large changes in the effective accretion rates that occur during the XN outbursts, these sources provide powerful probes of the accretion phenomena and radiation processes at work in black hole binaries. During their outbursts, these sources often undergo changes in their spectral and temporal characteristics; they may pass through the different *spectral states* observed in BHB (McClintock & Remillard 2003; Belloni, 2005). The X-ray ($\sim$1–10 keV) luminosities can change from values below 10^{30} erg s^{-1} when the sources are in quiescence (Garcia et al. 2001) to values that can approach or exceed 10^{39} erg s^{-1} for some sources.

During outbursts, we still do not have a detailed understanding of all the mechanisms that lead to changes in the X-ray emission properties, but the physics involves the structure of the accretion disc around the black hole as well as the connection between the accretion disc and the steady or impulsive jets that can be emitted from these systems. One of the causes of the changes in the X-ray emission properties are the variations of the mass accretion rate onto the black hole; however, also other physical parameters must be important for determining those properties even though a "two-dimensional behaviour " has emerged from the study of the spectral

and timing behaviour of the BHC XTE J1550–564, suggesting that a second parameter, correlated with the relative size of the Comptonised region, may play a role (Homan et al. 2001).

From the observational point of view, the emission properties of accreting black holes are often classified in terms of "spectral states ". A first classification that makes the state definitions more quantitative and connects these definitions directly to the continuum spectral components is due to McClintock & Remillard (2003). The spectra can often be described as the combination of a soft, thermal component along with a hard component that can fall off more or less steeply with energy. The simplest classification of black hole binary spectral states consists of two states: the hard and the soft (Zdziarski & Gierliński 2004). Roughly these two states are characterised by a different photon spectral index around $\sim$ 10 keV: $\Gamma < 2$ and $\Gamma > 2$ for hard and soft states respectively.

The hard state (also called low state, LS) is characterised by a weak soft blackbody component and a high-energy tail with a spectral cutoff at $\sim$100–200 keV, whereas the soft state (also called high state, HS) is characterised by a strong blackbody component and a hard tail beyond the blackbody, without any observable (as yet) high-energy cutoff. The soft state can take place at a very large range of the Eddington ratio, up to $L/L_{Ed} \sim 0.2$–0.3, where $L_{Ed} \simeq 1.5 \times 10^{38}(M/M_{\odot})$ erg s^{-1}.

When the source is in a quiescent state (weak or off) it usually has a relatively hard spectrum (when it can be measured), so it is probably a subset of the hard state. However, the detailed form of spectra of weak states remains uncertain because of their intrinsic low luminosity. Furthermore the soft state is often subdivided into the high (HS), very high (VHS) and intermediate (IS) states. The 'pure' high, or ultrasoft, state is supposed to have only the blackbody disc component, without a high-energy tail, but this definition is clearly dependent on the sensitivity of the

detecting instrument.

The IS takes place during transitions between the hard and soft states, and spectrally it is characterised by a high-energy tail starting close to the peak of the disc blackbody. The VHS is often defined as having the same spectral type as the IS (Gierliński 2003), but at high luminosities. In fact, the VHS is usually observed during transitions from the hard state to the soft state, so the difference with respect to the IS is small, if any (Homan et al. 2001). The appearance of VHS/IS can take place at a large range of the luminosity, between ~ 0.02 L_{edd} or even less and ~ 0.3 L_{edd} (Zdziarski & Gierliński 2004).

Today the *RXTE* and the *INTEGRAL* provide an opportunity to study the long-term evolution of sources as they enter different spectral states and exhibit different emission properties over a wide energy band.

4.3 Review of physical emission mechanisms of X-ray transient BHB Spectra

4.3.1 Accretion disc: standard model

The accretion disc component of the X-ray BHB spectra is usually modeled by the so-called *"Standard disc model"* in which the accreting gas forms a geometrically thin and optically thick disc, producing a quasi-blackbody spectrum due to thermal emission. The effective temperature of the accreting gas is in the range $10^5 - 10^7$ K, depending on the compact object mass and the accretion rate. The "standard disc model" was developed by Shakura & Sunyaev (1973): matter accreting onto a compact object (either in an AGN or a binary) is likely to have a net angular mo-

mentum, which causes formation of a disc. This occurs via viscous drag: assuming the system is Keplerian, differential rotation will occur, with the material closest to the black hole moving more quickly than the distant matter; the velocity at a radius r is given by:

$$v_{Kepl} = (\frac{GM}{r})^{\frac{1}{2}} \tag{4.1}$$

Thus, particles from an inner region will interact with those in the next region out, feeling a drag force. This causes the particles to move inward towards the centre of the gravitational field. As well as causing the inward movement of material, viscous drag dissipates heat, increasing the temperature of the accretion disc. The disc can then emit thermal photons, which are observed in the soft X-ray band (in the case of an X-ray binary) due to the range of temperatures produced.

The energy released through accretion is that due to the loss of potential energy, i.e.

$$E_{acc} = (\frac{GMm}{r}) \tag{4.2}$$

giving the accretion luminosity to be

$$L_{acc} = (\frac{dE_{acc}}{dt}) = (\frac{GM\dot{M}}{r}) \tag{4.3}$$

where m is the mass of the inward-falling particle, $\dot{M}$ the mass accretion rate and M the mass of the central accreting body. This is the maximum possible energy

gain of the particle; in fact, only half of this accretion energy is extracted, since the particle is actually orbiting the central object, rather than in free-fall. From the Virial Theorem, which states that, for a stable, self-gravitating distribution, the magnitude of the potential energy is equal to twice that of the kinetic energy, the remaining half of the potential energy is radiated as heat. Although accretion is a highly efficient process, there is a maximum luminosity that such systems can reach; this is known as the Eddington Limit, or Eddington Luminosity and occurs when the radiative force, pushing the accreting matter outwards, is equal and opposite to the gravitational attraction. The limit is given by

$$\frac{\sigma_T L_{acc}}{4\pi r^2 c} = \frac{GMm_H}{r^2} \tag{4.4}$$

$$\Rightarrow L_{Edd} = \frac{4\pi GMm_p c}{\sigma_T} \approx 1.26 \times 10^{38} \frac{M}{M_\odot} erg\ s^{-1} \tag{4.5}$$

with the assumption: $m_H = m_p + m_e \approx m_p$ and σ_T is the Thomson scattering cross-section.

The Shakura & Sunyaev theory describes the radiation emitted in terms of a geometrically thin ($H << R$ where H is the thickness and R is the radius of the disc), optically thick ($\tau > 1$, where τ is optical depth) and cool ($T = 10^4$ K) accretion disc (Shakura & Sunyaev 1973).

In this specific case, each element of the disc face radiates roughly as a blackbody with a temperature T(r) given by equation:

$$T(r) = \{\frac{3GM\dot{M}}{8\pi r^3\sigma}[1 - (\frac{r_*}{r})^{1/2}]\}^{1/4} \tag{4.6}$$

where we assume that there is an inner cut-off radius to the accretion disc at r_*.

We can approximate the spectrum emitted by each element of area of the disc as:

$$I_\nu = B_\nu[T(r)] = \frac{2h\nu^3}{c^2(e^{\frac{h\nu}{kT(r)}} - 1)}(erg\ s^{-1}\ Hz^{-1}\ sr^{-1}). \tag{4.7}$$

where $B_\nu(T)$ is the Planck function. For an observer at a distance D whose line of sight makes an angle i to the normal to the disc, the observed flux is:

$$F_\nu = \frac{2\pi\cos i}{D^2}\int_{r_*}^{r_{out}} I_\nu r\ dr \tag{4.8}$$

where r_{out} is the outer radius of the disc, since a ring between radii r and r+dr subtend a solid angle $2\pi r\ dr\cos i\ /D^2$. With the blackbody assumption, we get

$$F_\nu = \frac{4\pi h\cos i\ \nu^3}{c^2D^2}\int_{r_*}^{r_{out}} \frac{r\ dr}{e^{\frac{h\nu}{kT(r)}} - 1} \tag{4.9}$$

For frequencies $\nu \ll kT(r_{out})/h$ the Planck function B_ν takes the Rayleigh-Jeans form $2kT\nu^2/c^2$; hence Eq. 4.9 gives $F_\nu \propto \nu^2$.

For frequencies $\nu \gg kT(r_{out})/h$ the Planck function B_ν assumes the Wien form $2h\nu^3c^{-2}e^{-h\nu/kT}$: the integral in Eq. 4.9 is dominated by the hottest parts of the disc ($T \sim T_*$) and the integrated spectrum is exponential.

For intermediate frequencies ν such that $kT(r_{out})/h \ll \nu \ll kT_*/h$, Eq. 4.9 becomes approximately $F_\nu \propto \nu^{1/3}$. Assuming a black hole mass of 3 $M_\odot$ and an accretion rate of $\dot{m}_E$ ($\dot{m}_E = L_E/\eta c^2$ where η is the efficiency of accreting process, generally assumed ~ 0.1 and L_E is the Eddington luminosity) the maximum of F_ν gives us a peak of disc emission in the X-ray band.

This model can explain the production of soft X-ray photons, but not the hard X-ray photons. In fact the observed X-ray spectrum is too hard to be produced by the standard, optically thick disc model just described above.

The region supposed to be responsible for emission that gives rise to the observed hard X-rays is named the "Corona". Different models have been developed, based on different assumptions and physics, but all having the same aim to interpret and fit those observed spectra that could not be fully explained with the standard disc model. One of them, that is still being developed and tested, the *"Advection - Dominated Accretion Flow"* or ADAF model, originates as an alternative solution to the same hydrodynamic equations of viscous differentially-rotating flows that were solved in the standard disc model: the ADAF solution implies that matter falls into a black hole radiating inefficently. The energy, trapped in the gas, is advected towards the black hole. This can happen if the density of the infalling matter is low, so the particles make **few** collisions on their way beyond the event horizon. Therefore, ADAFs are much **less** luminous than thin discs at low values of $\dot{m}$. In fact, the luminosity of an ADAF scales roughly as $\sim \dot{m}^2$. In a thin disc, on the other hand, the luminosity scales as $\dot{m}$ (Narayan et al. 1998). The spectrum from

an ADAF around a black hole ranges from radio frequencies of $\sim 10^9$ Hz to gamma-ray frequencies. Figure 4.3 shows the schematic spectrum of an ADAF around a black hole.

Another largely used model, the *"Disc - Corona"* model, on the contrary, simply adds a new component to the standard model (see Section 4.3.2). For both models a critical value of the mass accretion rate, $\dot{m}_{crit}$, exists at which the approximations of the model fail. The convergence of the two possible relations between $\dot{m}$ and $\dot{m}_{\rm crit}$ gives:

$$\begin{cases} \text{Thin disc to ADAF} & \dot{m} < \dot{m}_{crit} \\ \text{ADAF to thin disc} & \dot{m} > \dot{m}_{crit}. \end{cases}$$

In fact the ADAF model is successfully applied to several black hole binaries in the quiescent state and low luminosity galactic nuclei that are supposed to have low efficiency accretion (Narayan et al. 1998). On the other hand, disc-corona models are generally applied to bright black holes supposed to be in a high accretion rate state like transient black holes in outburst.

4.3.2 Disc-Corona Model

The disc-corona model is not another solution of the set of equations that the standard disc or the ADAF fulfill; an extra component is added to the already defined thin disc, "the corona". A low density corona can be heated by reconnecting magnetic loops emerging from the disc (Galeev et al. 1979). This implies that the corona is coupled to the disc by the magnetic field.

In this case the broad-band X/γ-ray spectra of galactic black holes can be explained in terms of successive Compton scatterings of soft photons - *Comptonization*

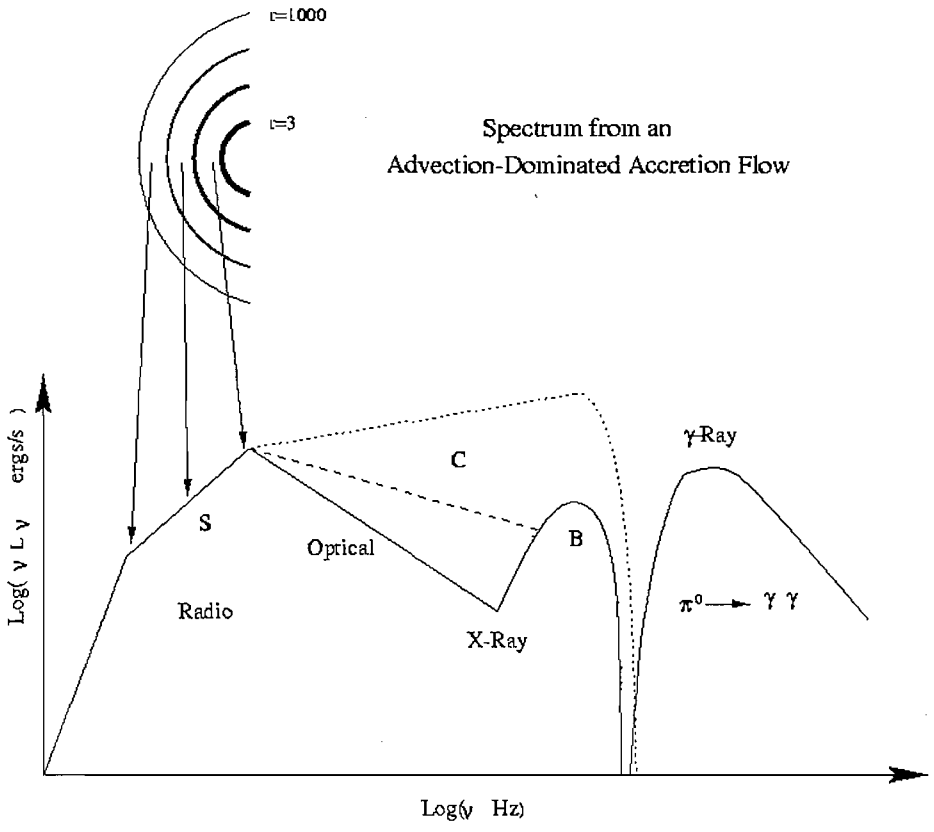

Figure 4.3: Schematic spectrum of an ADAF around a black hole. S, C, and B refer to electron emission by synchrotron radiation, IC scattering, and Bremsstrahlung, respectively. The solid line corresponds to a low $\dot{m}$, the dashed line to an intermediate $\dot{m}$, and the dotted line to a high $\dot{m} \sim \dot{m}_{crit}$. The gamma-ray spectrum is due to the decay of neutral pions created in proton-proton collisions. r represents, in arbitrary units, the different distances from the black hole (corresponding to different parts of the spectrum) (from Narayan et al. 1998).

- in a hot electron cloud. Both galactic black holes and Seyfert galaxies (a specific case of AGN) show a hardening of the spectra at $\sim$ 10 keV, which is attributed to Compton reflection (combined effect of photoelectric absorption and Compton down-scattering) of hard radiation from a cold material (George & Fabian 1991). This implies the presence of that cold material in close proximity. Hard radiation,

reprocessed in the cold matter, can form a significant fraction of the soft seed photons for Comptonization. The energy balance of the cold and hot phases determines their temperatures and the shape of the emerging spectrum (Poutanen & Svensson 1996).

4.3.2.1 Inverse Compton scattering

Inverse Compton scattering is the basic process involved in the reprocessing of the accretion disc photons (Comptonization). The main features of this process are briefly summarized below.

In the Inverse Compton process, an electron of energy $\gamma m_e c^2$ collides with a photon of frequency ν and up-scatters it to a higher frequency ν_c:

$$\nu_c \sim \frac{4}{3}\gamma^2\nu \tag{4.10}$$

This relation is valid in the Thomson limit, i.e. as long as the photon energy, in the electron rest frame, is less than the electron mass energy ($\gamma h\nu \leq 511$ keV).

At higher energies, the scattering in the electron rest frame is no longer elastic, and the full expression for the scattering cross section must be used (Klein-Nishina cross section). Considering an electron traveling in an isotropic photon plasma, due to the beaming effect it will see half of the photons (all those with $\theta \geq \pi/2$) coming inside a cone of angle $1/\gamma$, and all the photons scattered by the electron within an angle of $\pi/2$ in its rest frame, in the lab frame will be emitted inside an angle of $1/\gamma$ from the direction of motion. Averaging over all angles, the mean cooling rate for

the electron can be obtained as the difference between the incident and scattered powers. For an isotropic photon field, it is

$$\dot{E}_{IC} = \frac{4}{3}\sigma_T c U_{rad} \gamma^2 \beta^2 \tag{4.11}$$

where U_{rad} is the "seed" radiation energy density.

For a power-law electron energy distribution ($\propto \gamma^{-n}$), the total emissivity for a monochromatic photon field of energy ε_0 is

$$j_{IC}(\varepsilon_c) = \frac{1}{4\pi} \frac{(4/3)^\alpha}{2} \frac{\tau_c}{R/c} \frac{U_{rad}}{\varepsilon_0} (\frac{\varepsilon_c}{\varepsilon_0})^{-\alpha} \tag{4.12}$$

where R/c is roughly the photon escape timescale, $\tau_c = \sigma_T N_0 R$ is the total number of scattered photons, U_{rad}/ε_0 is the "seed" photon density, $\varepsilon_c/\varepsilon_0$ is the gain per scattering and $\alpha = (p-1)/2$ is the spectral index. This process translates a power-law particle distribution to a power-law emitted spectrum. For a non-monochromatic photon field, the emissivity is obtained by integrating Eq. 4.12 over the frequency range of "seed" photons:

$$j_{IC}(\varepsilon_c) = \frac{1}{4\pi} \frac{(4/3)^\alpha}{2} \frac{\tau_c}{R/c} \varepsilon_c^{-\alpha} \int_{\varepsilon_1}^{\varepsilon_2} \frac{U_{rad}(\varepsilon)}{\varepsilon} \varepsilon^{-\alpha} \, d\varepsilon \tag{4.13}$$

Note that ε_1 and ε_2 in general do not correspond to the minimum and maximum energies of the "seed" photon spectrum, but depend on ε_c. In fact, for a given photon energy ε_c, not all the seed photons ε can be upscattered to that energy, but

only those for which electrons exist such that satisfy the following:

$$\varepsilon = \frac{3}{4}\frac{\varepsilon_c}{\gamma^2}. \tag{4.14}$$

4.3.2.2 Geometry of the model

The hard powerlaw-like tail has different behaviour and characteristics depending on whether the source is in the hard or soft state.

In particular, in the hard state of a BHB, the dominant process is thermal Comptonization of soft photons from an outer accretion disc. Several geometries for the hot plasma cloud and the source of seed photons are possible, but the thermal character of the distribution of the scattering electrons is probably related to the most likely source geometry, consisting of an inner hot accretion flow (Abramowicz et al. 1995). As shown in Fig. 4.4(a), the electrons in the flow are powered from the hot ions by energy transfer, which receive most of the available gravitational energy. The stochastic nature of the energy transfer, probably via Coulomb interactions, results in the electron distribution being nearly thermal. In addition, the cold medium gives rise to reprocessing, including Compton reflection and fluorescence.

In the soft state the situation is more complex: the spectrum can be roughly described by a strong blackbody component that dominates the spectrum in energy terms, followed by an high energy tail with a photon index $\Gamma \sim 2.5 - 3$. The blackbody component is thought to come from an optically-thick accretion disc. However there is no consensus at present regarding the origin of the tail. Three main models have been proposed, all involving Comptonization of blackbody photons by high-energy electrons.

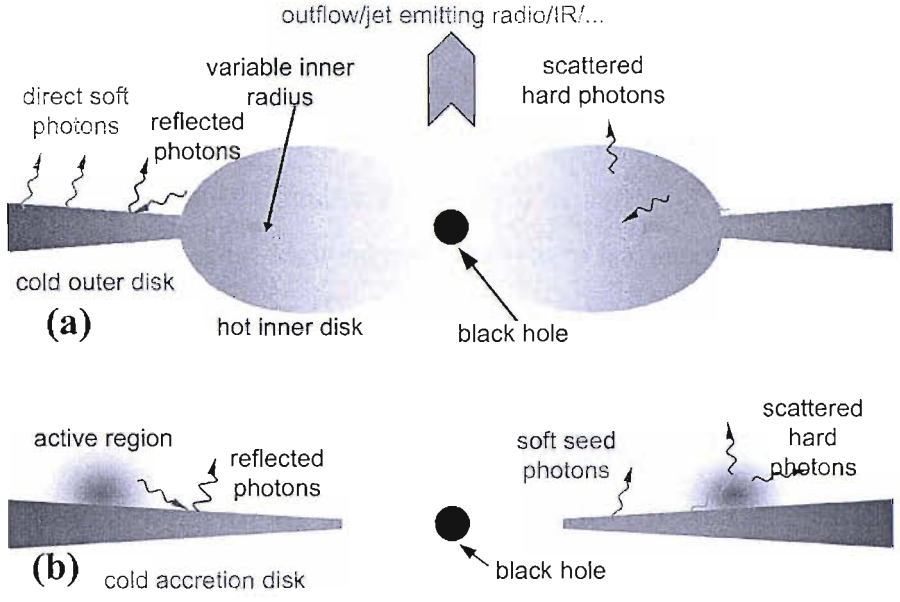

Figure 4.4: (a) A schematic representation of the likely geometry in the hard state, consisting of a hot inner accretion flow surrounded by an optically-thick accretion disc. In this case the hot flow constitutes the base of the jet (the jets are omitted from the figure for clarity). The disc is truncated away from the minimum stable orbit, but it overlaps with the hot flow. The soft photons emitted by the disc are Compton upscattered in the hot flow, and emission from the hot flow is partly Compton-reflected from the disc. (b) The likely geometry in the soft state consisting of flares/active regions above an optically-thick accretion disc extending close to the minimum stable orbit. The soft photons emitted by the disc are Compton upscattered in the flares, and emission from the flares is partly Compton-reflected from the disc (Zdziarski & Gierliński 2004).

The models differ in the distribution (and location) of the electrons, which are assumed to be either thermal (with a Maxwellian distribution), non thermal (with a distribution close to a powerlaw), or in free fall from about the minimum stable orbit down to the horizon of the black hole (see Zdziarski 2000 for a review).

Fig. 4.4(b) shows the supposed geometry of the soft state: the scattering plasma is believed to form active regions above the surface of an accretion disc, which emit

the energetically dominant blackbody emission. The active regions are powered by energy transfer from inside the disc, most likely via magnetic buoyancy and subsequent magnetic field annihilation, leading then to the acceleration of particles. This is inherently a non-thermal process, which explains the observed non-thermal photon spectra, showing no high-energy cutoff up to high energies. The ratio of the power in the active regions to the disc power increases in the sequence of the soft states: ultrasoft, high, intermediate/very high.

4.3.3 Radio emission from black hole binaries: jet production

Jets are formed in the region extending from around the black hole and the inner edge of the accretion disc and extending out, probably, along the symmetry axis. They are a narrow stream of energy and particles flowing out of the system with relativistic velocities. There is still not a comprehensive theory that can account for the process of jet formation, acceleration and collimation even if it is known, from the observations, that certain sub-classes of object produce powerful jets whilst others do not. A jet is identified by several unique observational characteristics in the radio band. The principal ones are:

- high brightness temperatures;
- "non-thermal" spectra;
- high degree of linear polarization measurements.

All of these characteristics indicate an origin of synchrotron emission from relativistic electrons. The principles of synchrotron radiation are briefly summarized in the next Section.

4.3.3.1 Synchrotron radiation: brief review

Charged particles, moving relativistically in the presence of magnetic fields B, lose energy emitting non-thermal synchrotron radiation with frequency spectrum peaked around

$$\nu \approx \frac{4}{3}\gamma^2\nu_L \tag{4.15}$$

where ν_L is the Larmor frequency ($= eB/2\pi mc$). The power emitted by the particle, if α is the angle between the velocity $\vec{v}$ and the magnetic field $\vec{B}$, is

$$P_s = 2\sigma_T c U_B \gamma^2 \beta^2 \sin\alpha^2 \tag{4.16}$$

where σ_T is the Thomson cross section and $U_B = B^2/8\pi$ the magnetic energy density. For an isotropic distribution of electrons, the average over the pitch angles leads to the expression for the electron average cooling rate:

$$\dot{E}_{syn} = \frac{4}{3}\sigma_T c U_B \gamma^2 \beta^2 \tag{4.17}$$

Beaming effects concentrate the emitted radiation field along the forward direction, leading to a distribution lying within a cone of half-angle $1/\gamma$, where

$\gamma = (1 - v^2/c^2)^{-1/2}$ for a velocity v.

For a population of electrons, assuming a power-law energy distribution $N(\gamma) = N_0\gamma^{-n}$ between γ_1 and γ_2, the total emissivity is obtained integrating Eq. 4.17 over $N(\gamma)$, yielding

$$j_{syn}(\nu) = B^{1+\alpha}\ N_0\ \nu^{-\alpha} \tag{4.18}$$

where $\alpha = (n-1)/2$. A power-law energy distribution of the emitting particles yields a corresponding power-law profile in the emitted spectrum. The emitted spectrum extends up to the maximum frequency ν_{max}, given by $\nu_{max} \sim \gamma_2^2\nu_L$.

Since the electrons also absorb photons with energy roughly similar to that which they can emit, a given population of electrons can self-absorb part of the synchrotron emission they produce. The frequency at which the optical depth is ≥ 1 is referred to as the self-absorption frequency ν_t. In this case, depending on whether thermal equilibrium is established or not, the resulting spectrum is $\propto \nu^2$ or $\nu^{\frac{5}{2}}$. Above ν_t, however, the region is optically thin and the spectrum is therefore given by Eq. 4.18.

4.3.3.2 The jets

Different jet properties are associated with different X-ray spectral states of transient BHBs. Transient BHBs in hard states display persistent radio emission with a flat radio-mm spectrum. This indicates the presence of an expanding outflow and the persistent emission implies the presence of a continuous supply of plasma. The flat spectral indices are generally interpreted in terms of synchrotron emission from a steady jet partially self-absorbed, which becomes progressively more transparent at lower frequencies as the particles travel away from the launching site

(Falke & Biermann 1996).

Some authors propose a jet interpretation (rather than the standard Comptonizing corona) for the X-ray power-law which dominates the spectrum of BHXBs in the hard/quiescent state (Markoff, Falcke & Fender 2001; Markoff et al. 2005). In this model a significant fraction – if not the whole – of the hard X-ray photons would be produced in the inner regions of the steady jet, by means of optically thin synchrotron and synchrotron self-Compton emission.

Whenever the source enters the soft state, there is a significant decrease in radio flux that is probably correlated with the disappearance of the jets.

X-ray state transitions seems to be associated with relativistic transient jets corresponding to arcsec-scale (thousands of A.U.) synchrotron-emitting plasma moving away from the binary core with highly relativistic velocities (Fender et al. 1999). The monotonic flux decay, observed after a few days in these transient radio ejections, seems to be primarily due to adiabatic expansion losses, as the decay rate is the same at all frequencies.

4.4 Correlation between X-ray and radio emission: a new spectral state classification

The results of detailed timing and colour/spectral analysis of the new data available for bright BHBs have provided evidence for a correlation between the inflow of material into the black hole and the outflow through the jets.

On the basis of these results, a new observational classification for black hole binary outbursts has been published (Belloni 2006; Fender Belloni & Gallo 2004).

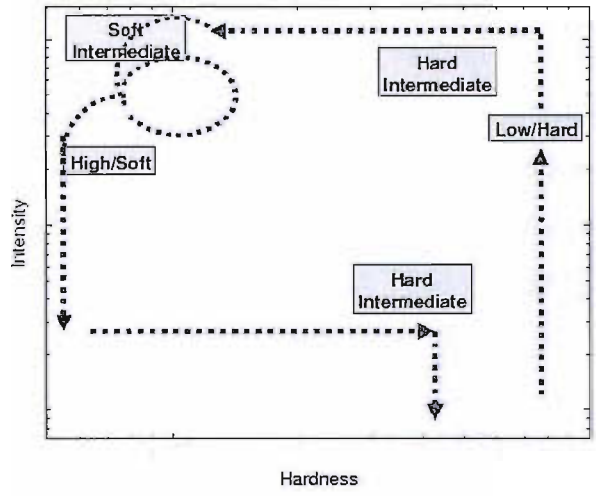

Figure 4.5: Representation of the hardness-intensity diagram for a transient BHC in outburst.

This classification, summarised below, is based on a characterization in terms of spectral and timing parameters, summarised in the color-intensity diagram of Transient Black Hole Binaries (TBHB) outburst data. This classification is inferred from a disc-jet coupling semi-quantitative model for black hole binaries systems (Fender Belloni & Gal In fact the state transitions also involve sudden changes in the properties of QPOs and radio and infrared bands. This scheme is followed by most of the transient BH observed and can be characterised in the colour-intensity diagram by a "Q-like" feature in which each branch represents a different state of the BH (see Fig. 4.5). The evolution of these states are briefly summarised below.

4.4.1 Low/Hard State (LS)

This state is associated with an accretion rate relatively lower than in the other bright states. The energy spectrum is hard and the fast time variability is dominated

by a strong (~30% fractional rms) band-limited noise and sometimes low frequency QPOs can be observed in the power spectrum and the characteristic frequencies of the different noise components increase with time. This state can be associated with the right branch of Fig 4.5. The source flux increases with harder spectral shape. Also flat-spectrum radio emission is observed that is probably associated to compact jet ejection (see Gallo, Fender & Pooley 2003; Fender, Belloni & Gallo 2004).

4.4.2 Hard Intermediate State (HIMS) I

This state corresponds to the top of the right branch of Fig 4.5 and part of the horizontal branch. In fact the energy spectrum becomes softer than in the LS, and a soft thermal disc component becomes detectable. The radio spectrum becomes steeper and the velocity of the jet outflow increases (Fender Belloni & Gallo 2004). In the power spectrum the transition is smoother with characteristic frequencies that continue to increase.

4.4.3 Soft Intermediate State (SIMS)

Just before the transition to the SIMS state, Fender (2004) suggested that the jet velocity increases rapidly, giving origin to a fast relativistic jet together with strong radio flares. Also great changes appear in the power spectrum features. This happens when the hardness-intensity diagram of the source approaches the second line in the horizontal branch, called the "jet line" (Fender Belloni & Gallo 2004).

Behind this line, there is no detection of any radio emission. The source remains for a long time in the top left region of the diagram; the spectrum is now softer because the disc component dominates the flux, and the power spectrum shows

complex and variable features.

The properties of the SIMS are complex. For example in systems like XTE J1859+226, fast transitions to and from the HIMS are observed corresponding to the crossing of the jet line with immediately subsequent radio flares that correspond only to the previous jet ejections (Fender, Belloni & Gallo 2004).

4.4.4 High/Soft State (HS)

The energy spectrum is soft and strongly dominated by a thermal disc component, a weak power-law hard component is present without any detectable cutoff up to 300 keV. The flux decreases with time and only weak power-law noise is observed in the power spectrum. No core radio emission is detected (see Fender et al. 1999). In this configuration the source is in a regime that is probably the closest one to the Shakura-Sunyaev theory of accretion discs (Belloni 2006).

4.4.5 Hard Intermediate State (HIMS) II

The source flux decreases with time and starts to move to the right part of the diagram with a harder spectrum. After the flux passes the line, it enters again the HIMS state with the same characteristics of the previous transition but with a weaker flux. The source continues to harden and moves to the right reaching the same value in the diagram where it started its outburst.

4.5 Conclusions and open questions

The classification described in the previous pages is a semi-quantitative classification based on the observational characteristics of transient black hole binaries. A comprehensive model that could explain and predict the different state of a BHB has not been developed yet. ADAFs and disc-corona models do not work for all cases. This is probably due to the fact that the mechanisms at the base of the accretion processes are still not totally understood. To date a crucial test of the models is given by how they are able to reproduce the shape of the high-energy tail. Its major spectral feature is the lack of an observable high-energy cutoff in all BH binaries in the soft state. The open questions and the basic topics on accretion disc theory can be summarised as follows:

- it is by now generally believed that one of the main parameters driving the transition between states is the accretion rate variation;

- from the theoretical point of view, the soft quasi-thermal component is thought to be the clear signature of a Shakura & Sunyaev standard model disc. Thus, the observed hard-X-ray powerlaws represent a universal signature that another physical process is involved. This is why the standard thin accretion disc model accounts for the basic physical properties of black holes in their soft states;

- the accretion mode responsible for the low-luminosity hard/quiescent states is still a matter of debate. In this case radiatively inefficient, advection-dominated accretion flows (ADAF) could be a natural solution of the problem;

- When tested against the best data for hard state BH-XRBs, though, as in the case of XTE J1118+480 (Esin et al. 2001) or Cygnus X-1 (Esin et al. 1998),

ADAF models alone do not work. A transition between an inner ADAF and an outer Shakura-Sunyaev disc is needed.

An overall model could also take into account the presence of jets that, as the observations seem to demonstrate, are strictly connected to the accretion phenomena. In fact the jets represent one of the most obvious, important and yet poorly-explained phenomena associated with accreting relativistic objects. It is reasonable to suppose that 70% of the galactic X-ray binary systems are able to generate jets (Fender 2004). In fact jets have been observed in most of the objects in which emission is driven by accretion:

- all the black hole systems which are either in the 'low/hard' X-ray state or in the intermediate state are associated with the formation of jets. Then the majority of known binary black holes are, or have been in the past, associated with a jet;
- most of the accreting neutron stars are also associated with jets or radio emission. In particular the six bright "Z sources" are all associated with jets, while the lower luminosity magnetic fields, "the Atoll sources", are all associated with radio emission;
- on the contrary, the high magnetic field neutron stars and only two accreting X-ray pulsars are not associated with jets.

The next Chapters describe the work, undertaken for this thesis, on a sample of BHBs in outburst. We focused our analysis on the sources detected by *INTEGRAL* from its launch to the end of 2005. The data cover an energy range from about 3 keV to 200 keV and are sampled in different periods of the outburst. For the brightest sources, a detailed spectral analysis is also reported.

Chapter 5

Global view of the BHC observed with INTEGRAL

5.1 First and second survey catalogue

The first and the second *INTEGRAL*/IBIS surveys have been realised collecting the *INTEGRAL* GPS and GCDE data together with all the public data available. The energy range chosen is 20-100 keV and the sources are detected up to a limited sensitivity $\sim$ 1 mCrab. The mean position error for all the sources detected with significance above 10σ is $\sim$ 40". The first and the second catalogues have been published in 2004 (Bird et al. 2004) and in 2006 (Bird et al. 2006) respectively. The 123 sources detected in the first catalogue were mostly concentrated in the galactic plane region, due to the obvious constraints in the Core Program pointing strategy. In the second catalogue the source number has increased by $\sim$ 70% because of the high increase of the exposure time (from 5 Ms to more than 10 Ms) and also due to a higher coverage of the sky (more than 50%). In fact in the second catalogue not

only the Core Program data but also all the public data of the first observation year (more randomly distributed in the sky) are included. This impacts mostly on the AGN number that are concentrated out of the galactic plane. The second catalogue is dominated by the detection of X-ray binaries (113 objects), with 38 high-mass and 67 low-mass. In most cases the compact object is a neutron star, but the sample also contains 4 confirmed black holes and 5 LMXB black hole candidates. There are also an additional 6 tentative associations as BHCs based simply on spectral and timing properties. The sample contains also 4 isolated pulsars, 4 supernovae remnants and 2 associations with molecular clouds. As a direct consequence of wider and deeper sky coverage, the number of AGN are increased by 200% with respect to the previous catalogue, detecting 33 extragalactic sources. The *INTEGRAL* (IGR) sources represent new detections in the soft gamma-ray wavebands. There are 39 sources of this sample that are of unknown nature while 17 have been tentatively classified.

5.2 A Sample of transient black hole candidate observed by INTEGRAL

In the sample of 12 sources (BHC or tentatively associated with a BHC) there are 7 transient sources that went into outburst during the *INTEGRAL* survey observations. The following Sections of this Chapter provide a summary of the temporal behaviour of these source outbursts as detected by *INTEGRAL* . In order to have a better understanding of the overall behaviour, when possible, the *RXTE*/ASM light curves and hardness ratio are also shown. In particular two of them, IGR J17464–3213 (H1743–322) and IGR J17091–3624, have been chosen for their similarity in both outburst characteristics and spectral properties. A detailed analysis of their data is described in Chapters 6 and Chapter 7 respectively. Concerning the other

sources, two of them were very faint and poorly covered by observations to enter in details (XTE 1908+094 and IGR J18539+027). The data analysis of the remaining sources of the sample has been reported by other authors.

5.2.1 Transient BHC sample

- **IGR J17464–3213** (H1743–322)(see Chapter 6). This is an X-ray transient observed in outburst for the first time by *HEAO* 1 in 1977. The second outburst observed by *INTEGRAL* in 2003 was very bright and was followed through its evolution by *INTEGRAL* (Capitanio et al. 2005b), *RXTE*(Homan et al. 2005) and *Chandra* (Miller et al. 2004). The source was also observed, during the outburst, in the radio bands (Rupen et al. 2004a).

- **IGR J17091–3624** (see Chapter 7). This source was observed for the first time by *INTEGRAL* itself (Kuulkers et al. 2003) and immediately after it was observed by *RXTE*(Lutovinov & Revnivtsev 2003).
  After the discovery, detections from the archival data of both *mir* KVANT/TTM in 1996 (Revnivtsev et al. 2003b) and *BeppoSAX* WFC in 1996, 2001 (in 't Zand et al. 2003), have been reported.

- **XTE 1908+094** has been detected for the first time during a *RXTE*/PCA scan of the soft-gamma-ray repeater SGR 1900+14 (Woods et al. 2002) The source spectrum (2-30 keV) can be best fit with a powerlaw function including photoelectric absorption (column density $N_h = 2.3 \times 10^{22}$, photon index = 1.55). An iron line emission is present, but it may be due to the galactic ridge. The maximum source flux (2-10 keV) reached was 64 mCrab, no coherent pulsations are seen between 0.001 and 1024 Hz. XTE J1908+094 is classified as a possible black hole candidate. Figure 5.1 reports the A (1.5-3 keV), B (3-5 keV) and C (5-12 keV) *RXTE*/PCA bands light curves and the hardness ratio from 2001

til the end of 2003. The hardness ratio is defined as the ratio between the lower energy range and the subsequent one (1.5-3 keV/3-5 keV in the case of RXTE data). The *INTEGRAL* data cover the period around November 2003. Unfortunately the *INTEGRAL* data covers only the final part of the weak outburst detected by ASM monitor, when the source was coming back to the hard state. Fig. 5.2 shows the IBIS light curves and the hardness ratio (20-40 keV/40-60 keV).

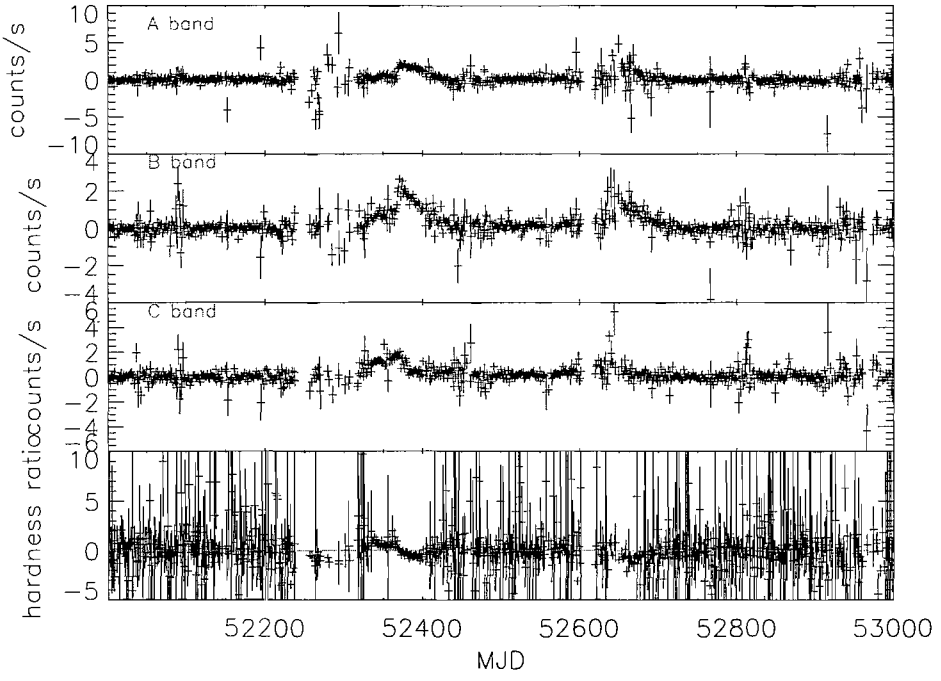

Figure 5.1: XTE J1908+094: A, B and C *RXTE*/PCA bands light curves and the hardness ratio (see text).

- **IGR J18539+0727**. This faint transient source was detected during a routine scan of the galactic plane and deep observations of the GRS1915+105 field

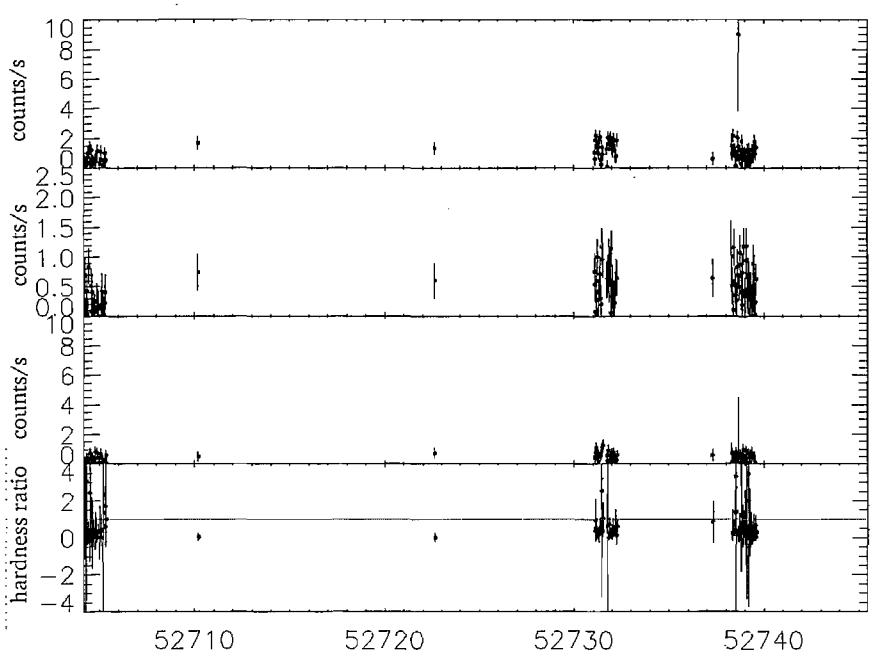

Figure 5.2: XTE J1908+094. IBIS light curves in three energy bands (20-40, 40-60, 60-100 keV) and the hardness ratio (see text).

on April 17-18 2003. It is classified as a probable BHC because of its hard spectrum. Figure 5.3 shows the IBIS light curves and hardness ratio between the first and the second energy band (20-40 keV/40-60 keV). The HR shows a slight softening probably due to a spectral transition of the source.

- **XTE J1720–318** was discovered on 2003 January 9 with the ASM monitor on board *RXTE*as a transient source in outburst. The source flux increased to the maximum value of ~430 mCrab in 2 days, and then started to decay slowly. Follow-up observations of *RXTE*/PCA have shown the presence of a 0.6 keV thermal component and a hard tail. The spectral parameters and the source luminosity suggested a BHB in a high/soft state. Soon after, a radio counterpart was identified with the VLA and ATCA radio telescopes.

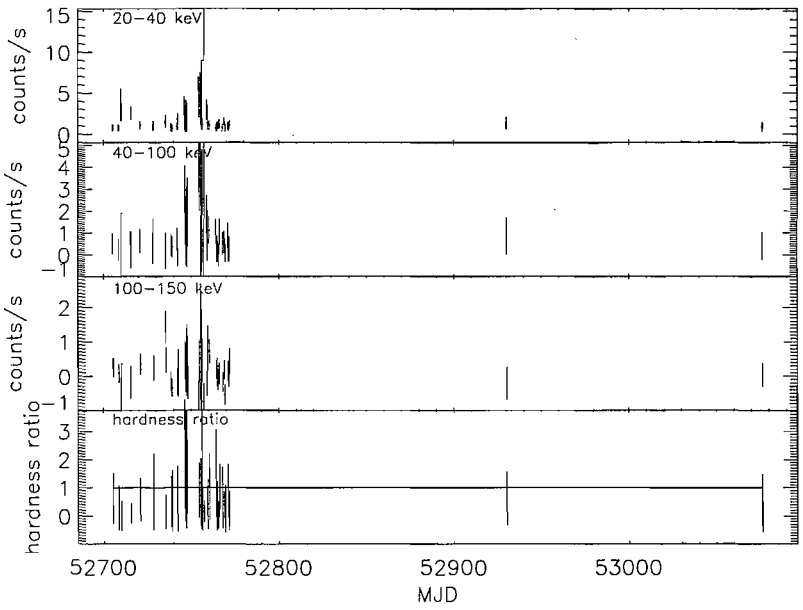

Figure 5.3: IGR J18539+0727: IBIS light curves in three energy bands (20-40, 40-60, 60-100 keV) and the hardness ratio (see text).

XTE J1720–318 was observed by *XMM-Newton*, *RXTE*and *INTEGRAL* in February during dedicated Target of Opportunity (ToO) observations. It was then observed by *INTEGRAL* during the deep observations of the GC region performed in March and April and again from August to October 2003 (Cadolle Bel et al. 2004). Even if the data coverage is not complete, the results obtained from all these observations present a weak and steep tail in the hard energy range, typical of a BHC in high/soft state. The overall data analysis showed a possible transition to a hard state. In this state, the source was detected up to 200 keV with a powerlaw index of ~ 1.9 and a peak luminosity of $\sim 7 \times 10^{36}$ erg s^{-1}. The source decayed to a quiescent state after April. A detailed analysis of the XTE1720–318 outburst can be found in Cadolle Bel et al. 2004. Figure 5.4 (top panel) shows the *RXTE*/ASM light curves and the hardness ratio, while the bottom panel of the same figure shows the IBIS light curves in three energy bands. The outburst of the source and its softening are clearly visible in both *RXTE*and IBIS light curves and hardness ratios.

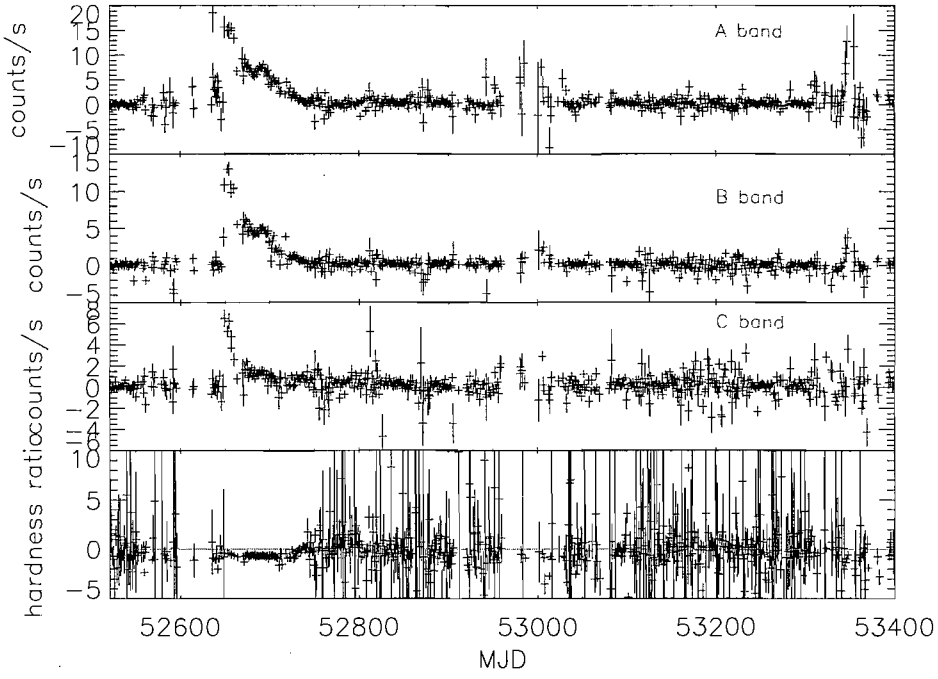

Figure 5.4: XTE J1720–318: A, B and C *RXTE*/PCA bands light curves and the hardness ratio (see text).

- **4U 1630–47** is one of the most active transient BHC. Its last outburst was very long covering more than two years (2002-2004). Moreover the source went again into outburst at the end of 2005. The 2002-2004 outburst, probably the longest observed for this source, was followed continuously by *RXTE*and *INTEGRAL* . The analysis of *INTEGRAL* and *RXTE*2002-2004 outburst data was published by Tomsick at al. (2005). Figure 5.6 shows the *RXTE*/ASM light curves and the hardness ratio, while Figure 5.7 shows the IBIS light curves and the hardness ratio.

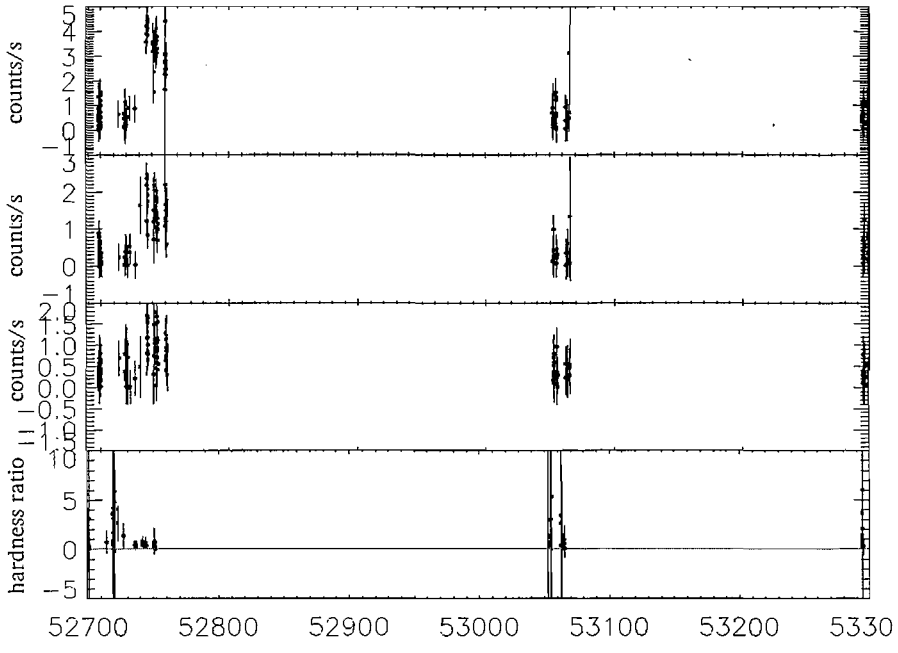

Figure 5.5: XTE J1720–318: IBIS light curves in three energy bands (20-40, 40-60, 60-100 keV) and the hardness ratio (see text).

- **IGR J17285–2922** had a single period of activity in September 2003 when it was detected by *INTEGRAL* . The spectral characteristics and its position in the sky, very close to galactic bulge, are consistent with a LMXB containing a black hole or a neutron star. Even if the nature of the compact object is still not constrained, its hard spectrum and the lack of type-I bursts suggests that the source could be a BHC. Figure 5.8 shows the IBIS light curves and the hardness ratio. A detailed analysis of the IGR J17285–2922 data, collected by *INTEGRAL* , is reported by Barlow et al. (2005).

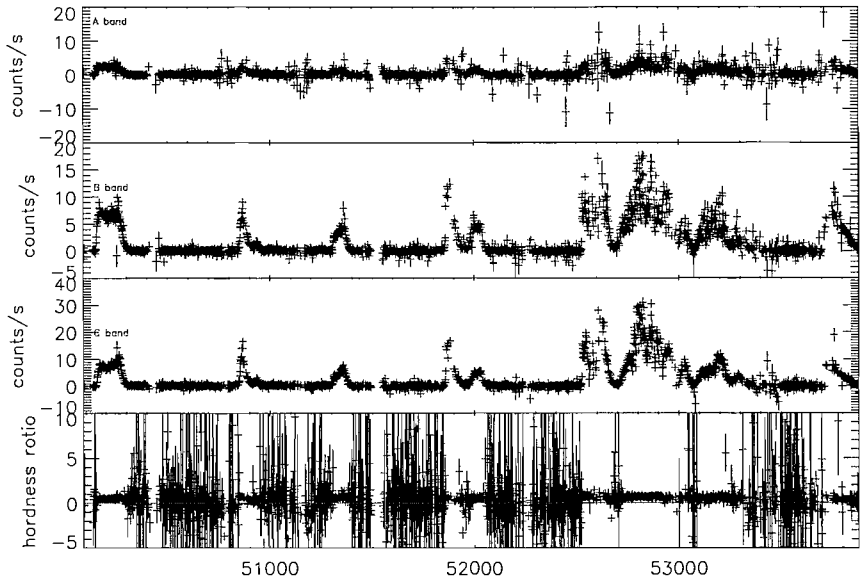

Figure 5.6: 4U 1630–47: A, B and C *RXTE*/PCA bands light curves and the hardness ratio (see text).

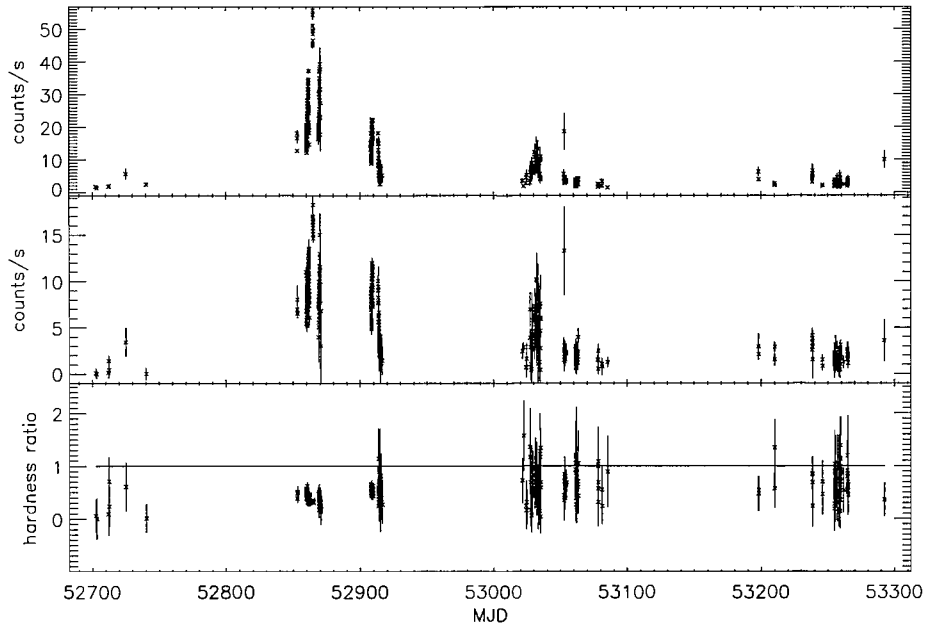

Figure 5.7: 4U 1630–47: IBIS light curves in three energy bands (20-40, 40-60, 60-100 keV) and the hardness ratio (see text).

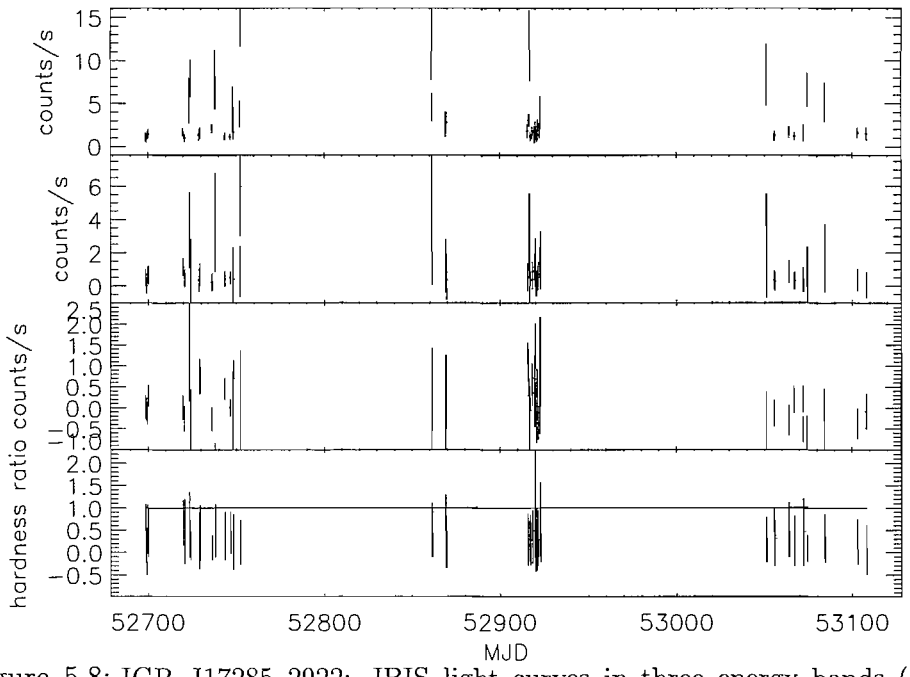

Figure 5.8: IGR J17285–2922: IBIS light curves in three energy bands (20-40, 40-60, 60-100 keV) and the hardness ratio (see text).

5.3 Concluding remarks

This Chapter illustrates the capability of the IBIS telescope to detect the state transitions in transient black hole binaries. This work has been limited to the transient BHC found in the second survey catalogue. In the third catalogue, that is still in publication, there are another five BHCs detected in outburst. All of these BHCs are distributed around the galactic centre as expected for LMXBs. For this reason *INTEGRAL* with its energy coverage, large field of view and observational strategy, has a good probability to detect transient LMXBs and especially the BHCs because of their hard spectra. The next two Chapters illustrate the detailed analysis of two BHC, IGR J17091–3624 and IGR J17464–3213, performed with the IBIS telescope, JEM-X monitor and, when it was possible, also the spectrometer SPI.

Chapter 6

IGR J17464–3213 (H1743–322)

6.1 History and characteristics of the source

On 2003 March 21 during the GCDE Program *INTEGRAL* detected a relatively bright source (~60 mCrab at 15-40 keV) named IGR J17464–3213. The source was then localised at R.A. (2000) = $17^h46.3^m$, Dec. = $-32°14.4'$, with an error box of 1.6 arcmin (90% confidence) and associated with H1743–322 (Markwardt et al. 2003; Revnivtsev et al. 2003a), a bright BHC observed by *HEAO1* in 1977 with an intensity of 700 mCrab at 2-10 keV (Doxsey et al. 1977) and localised with two possible positions. The error box of IGR J17464–3213 was compatible with only one of these two, thereby resolving this 25 year old ambiguity. The source outburst evolution was followed by *RXTE* and *INTEGRAL* reported strong flux and possible spectral variability (Markwardt et al. 2003; Revnivtsev et al. 2003a). After the start of the outburst in 2003, the source remained bright in soft X rays (E < 15 keV) for ~ 8 months and was regularly detected with the JEM-X monitor on board *INTEGRAL* . The source, after the first and brightest outburst, showed another two peculiar out-

bursts. A radio-band observation campaign was also performed. A radio flare was seen by NRAO during the rising part of the first outburst (MJD=52728) and two jets were detected between the first and the second outburst (MJD= 52955-53049; Corbel et al. 2005). Interestingly, the time period between the peak of an outburst and the subsequent one is equal and it has a value of about 400 days with decreasing flux. Figure 6.1 indicates the *INTEGRAL* observation coverage compared with the monitoring of the source that has been made by *RXTE*/ASM from March 2003 to August 2005.

Some results shown in this Chapter have been published in the Astrophysical Journal in 2005 (Capitanio et al. 2005b), while the others have been presented in conferences and workshops in 2005 and 2006 (Capitanio et al. 2005a; Capitanio et al. 2006a; Capitanio et al. 2006b).

6.2 Data Analysis

The data set consists of all *INTEGRAL* public observations in which IGR J17464–3213 was within the high energy detectors field of view. The *INTEGRAL* observations are organised into un-interrupted ~2000s long science windows (SCW). Light curves, hardness ratio and spectra are then extracted for each individual SCW. Broad band spectra of the source are obtained using data from the three high energy instruments (JEM-X, IBIS and SPI). In particular, the IBIS and JEM-X data were processed using the Off-line Scientific Analysis (OSA; Goldwurm et al. 2003) and divided in two subsets according to the source position being within the partially coded field of view (PCFOV) or in the narrower fully coded field of view (FCFOV). Both data sets have been used, after source intensity correction for off-axis detectors response, to produce the source light curves in different energy ranges. Only

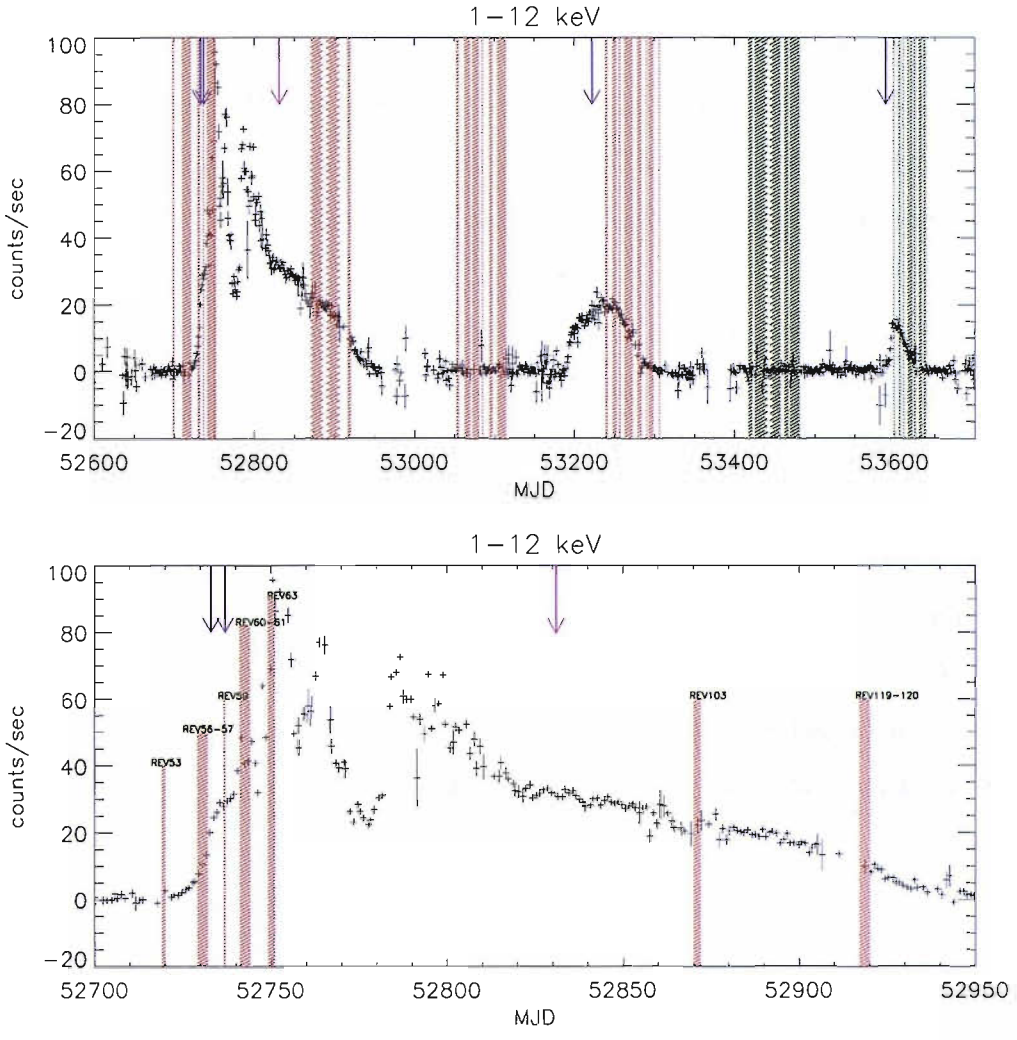

Figure 6.1: *Top panel:* *RXTE*/PCA 1-12 keV light curve of the H1743–322 temporal behaviour from March 2003 to August 2005. The dotted rectangles represent the *INTEGRAL* observation periods of the source (red: public data, green: proprietary data, violet arrows: radio observations with detection, pink arrow: radio observations without detection). *Bottom panel:* the zoom on the first outburst data of the *RXTE*/ASM 1-12 keV light curve. The dotted rectangles are the *INTEGRAL* fully coded observation periods of the source with their revolution numbers (the arrows have the same meaning explaned in the top panel caption).

FCFOV data, less affected by the off-axis response of the gamma-ray instruments, was selected for spectral extraction and fitting.
SPI spectra have been obtained in collaboration with the SPI instrument team and were extracted using software specially developed for fitting the positions and the fluxes of all significant sources in the field of view. The background model used for SPI data is based on a uniformity map determined for each energy band from empty fields observation.
When spectral data are obtained in the same time interval from more than one instrument, the proper normalising constant is added in the data fit, taking into account the best knowledge of the instrument cross calibration. In optimum conditions, the *INTEGRAL* spectra we produced cover the range from 3 keV to 400 keV. The data of IGR J17464–322 are mostly collected from the Core Program observations. For this reason the data set covers most of the phases of the outburst with a serendipidous distribution. While IBIS and SPI provide a very large FOV (>30 deg), JEM-X has a narrower FOV (>10 deg). This fact, together with the Core program dithering politics, provided only a partial overlap of JEM-X with the high energy detectors.

6.3 Results

6.3.1 The time evolution of the outbursts

The source was continuously monitored by the *RXTE*/ASM and whenever possible by *INTEGRAL* as shown in the top panel of Figure 6.1, with the simultaneous *INTEGRAL* observation periods represented by dashed red and green lines. The first peak was observed by *INTEGRAL* quite continuously, while the second peak was observed only in its declining phase. The analysis of the third peak is not consid-

ered in this work because the data were proprietary when this analysis was made. Figure 6.2 shows the *RXTE*/ASM light curves in three energy bands (A-B-C) and the hardness ratio (HR) defined as:

$$HR = (flux_C - flux_A)/(flux_A + flux_C).$$

The three peaks of the source outbursts are clearly evident.

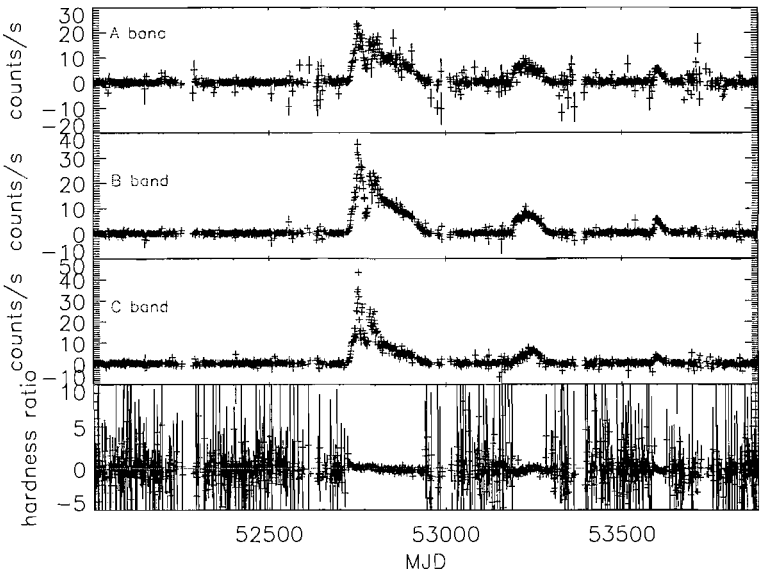

Figure 6.2: *RXTE*/PCA light curve in A (1.5-3 keV), B (3-5 keV), C (5-12 keV) energy bands of H1743–322 during its three outbursts (from March 2003 to August 2005) and the hardness ratio (see Section 6.3.1).

Figure 6.3 shows the IBIS light curves of all the *INTEGRAL* public observations of the source and the corresponding hardness ratio (HR) defined as:

$$HR = (flux_{60-100} - flux_{20-40})/(flux_{60-100} + flux_{20-40}).$$

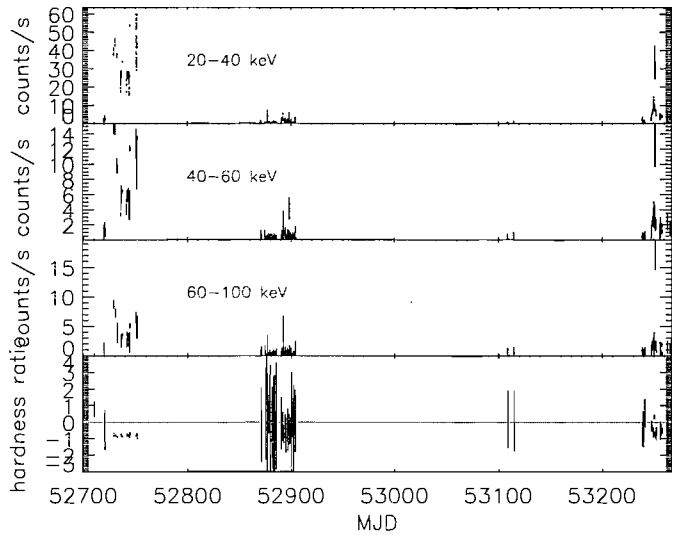

Figure 6.3: IBIS light curves of H1743–322 (20-40 keV, 40-60 keV, 60-100 keV) and the hardness ratio (see Section 6.3.1).

6.3.2 First outburst

As the bottom panel of Figure 6.1 shows, the monitoring of the source was quite continuous during the pre-outburst episode (from revolution 53 to 61) and then the rest of the outburst was covered only by three deep observations. The first was performed during the peak of emission (revolution 63). The other two after about 4 (revolution 103) and 5.5 months (revolutions 119-120) respectively.

The evolution of the first outburst followed the typical behaviour of a transient black hole: it was first detected in the hard state, then passed thorough the soft and very high soft state and, at the end of the outburst, it was back to the hard state. The IBIS 20-40 keV and 40-60 keV light curves of the rising part of the first outburst, flux averaged over one SCW, are shown in Figure 6.4 together with the hardness ratio (HR) defined as:

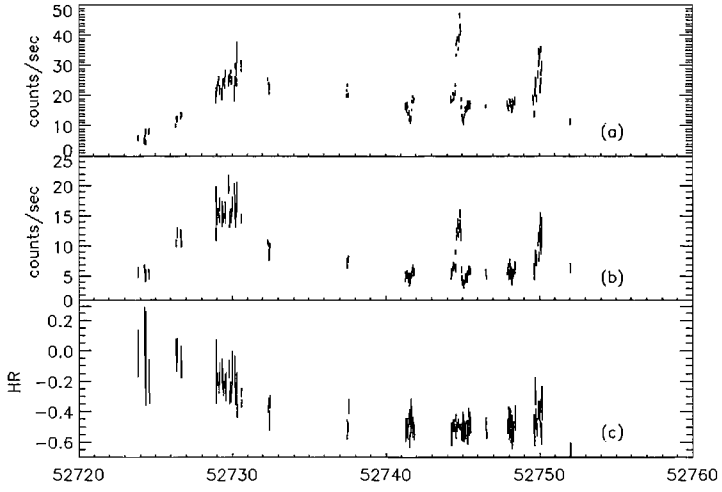

Figure 6.4: (a) 20-40 keV and (b) 40-60 keV IBIS light curves from revolution 53 to revolution 61. The hardness ratio derived from the two energy ranges is shown in the bottom part of the figure (c) and defined in Section 6.3.2.

$$HR = (flux_{40-60} - flux_{20-40})/(flux_{40-60} + flux_{20-40}).$$

In this period, the IBIS light curves show strong variations and it is possible to note several short peaks in the flux intensity with different shapes in the lower and higher energy bands. From the beginning of the IBIS observation, MJD ~52729 to ~52731, the source averaged intensity increases monotonically in the lower energy range while the flux is almost unchanged at higher energies: this is reflected in the anticorrelation shown by the HR that decreases continuously in the same week as can be seen in Figure 6.4(c). The few points sampled in the next 20 days, due to a limited coverage, show a decrease in both low energy flux and HR. Starting from day MJD ~52744, the source shows a clearly visible flux increase in a few hours by a factor of 2.6, 3.0 and 3.2 in the 20-40, 40-60 and 60-100 keV ranges respectively, without any corresponding hardening. After the peak, the source emission falls by

a factor of ∼4.5 in the following hours (20-40 keV) with a small decrease of the HR; the soft part of the spectrum becomes now more prominent (Figure 6.4).

This corresponds to a dip in the flux emission, lasting a few hours (around day 52745.1), during which the source shows the lowest observed value for the HR. Finally, the high energy component, and the HR, increase again (MJD=52745.5). The source shows a similar behaviour around MJD=52750.

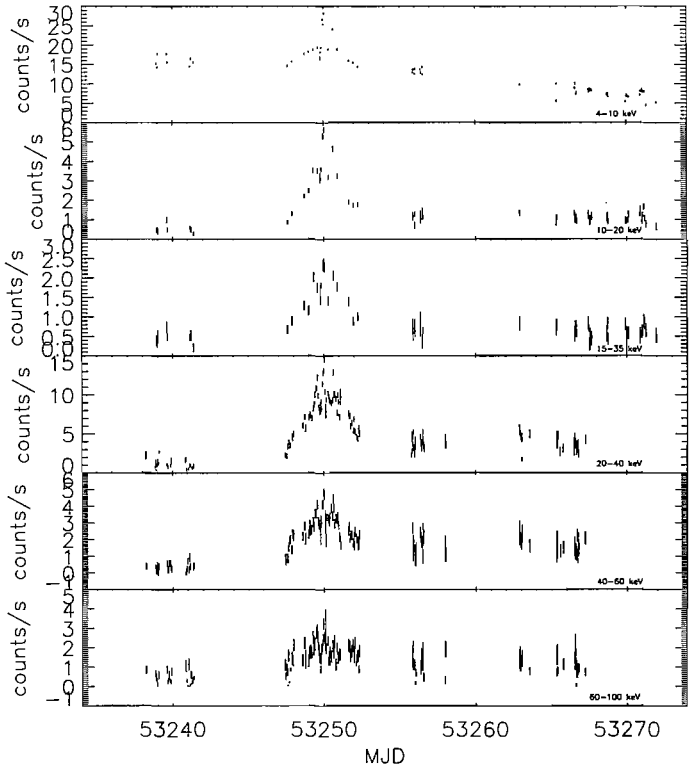

Figure 6.5: IBIS and JEM-X light curves binned to 2000 seconds of the July 2004 outburst.

6.3.3 Second outburst

For the second outburst, the analysed data show that the source had a short transition to the hard state and then back to the soft state with a peculiar temporal

and spectral behaviour as the *RXTE*/ASM hardness ratio shows in bottom panel of Figure 6.2. The *INTEGRAL* data cover only the declinig part of the outburst. IBIS/JEM-X light curves in six energy ranges of this period, as Figure 6.5 shows, is characterised by the presence of a small secondary peak of about 4 days. This peak is not visible in the ASM light curve. Figure 6.6 shows the IBIS hardness ratio (HR) of the second outburst,defined as:

$$HR = (flux_{40-60} - flux_{20-40})/(flux_{40-60} + flux_{20-40}).$$

The data shows a sharp softening of the sources during its declining phase coincident with the small peak of Figure 6.5.

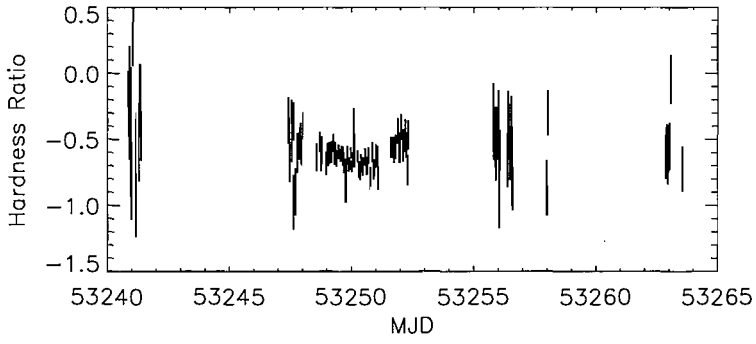

Figure 6.6: *INTEGRAL* hardness ratio curve around the peak present in the declining part of the second outburst. The HR is defined in Section 6.3.3.

6.3.4 Spectral evolution of the source

6.3.4.1 First outburst

The three panels in Figure 6.7 show the detailed spectral behaviour of the source during the rising and declining part of the outburst, while Figure 6.8 shows the very high/soft state of the source. The whole set of data has been fitted with standard XSPEC tools. At the beginning of the outburst (revolution 53) the source is very weak and therefore the flux is below the JEM-X sensitivity. Therefore, it was possible to extract only a few points from the JEM-X data in the range 15-22 keV and only a 2σ upper limit at lower energies. A single COMPTT model fits the whole data set (15-150 keV) well, as shown in Table 1 with a $kT_e \sim 20$ keV and a $\tau_p \sim 3$.

The point corresponding to revolution 53 in Figure 6.9 shows the correlation between the photon index and the flux for this data, indicating a low/hard state (Grebenev et al. 2003). In a few days the source flux then increases quickly, and the statistics enable extraction of the SPI spectra as well (revolutions 56 and 60-61). The high energy spectral evolution clearly indicates that the source makes a transition to the soft state as also shown in the HR evolution (see Figure 6.4 (c)). During revolution 56 the source was out of the JEM-X FOV. Therefore, only in this case, there are no data for E $<$ 20 keV. But the source is quite luminous in the hard X-rays as shown by IBIS and, moreover, looking at the spectral evolution during the outburst (Figure 6.7), is possible to suppose that the source is still in a low/hard state. In revolutions 57-59 the 3-200 keV data can be fitted with a cutoff powerlaw or with a thermal Comptonization model without adding any blackbody component (Table 1). In revolutions 60-61 the disk blackbody appears very bright and the emission of this component accounts for 45% of the total luminosity.

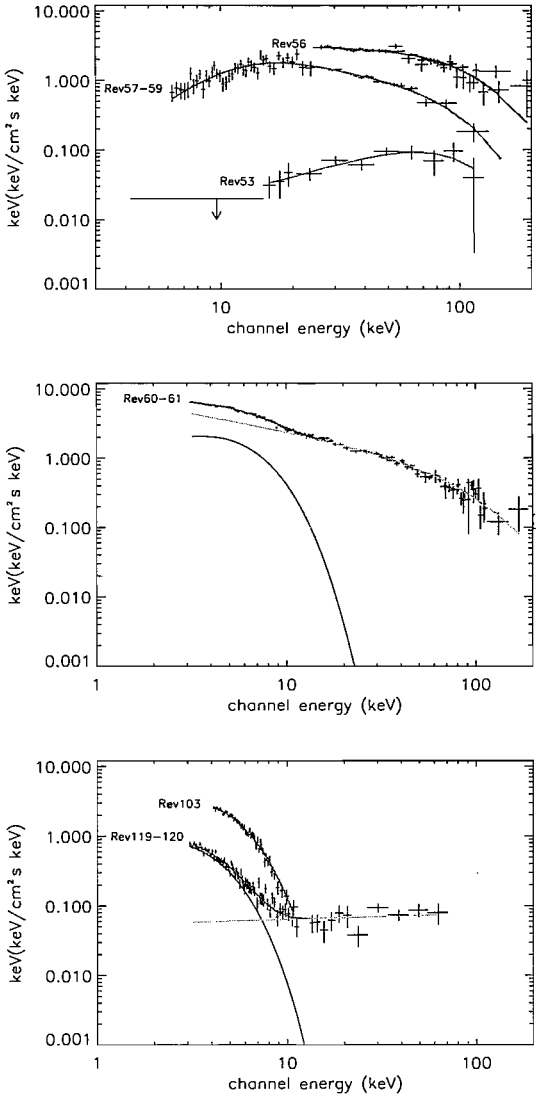

Figure 6.7: IBIS, JEM-X and SPI common spectra in different states of the source outburst: the numbers on the top of each spectrum indicate the revolution number of the corresponding *INTEGRAL* observation.

During the brightest part of the outburst the source still had a prominent disc emission ($T \sim 1.3$ keV) and a variable flux. Its spectra had a soft tail extending until 300 keV without any cut off with a photon index of about 3. Figure 6.8 shows a source spectrum of the VHS period.

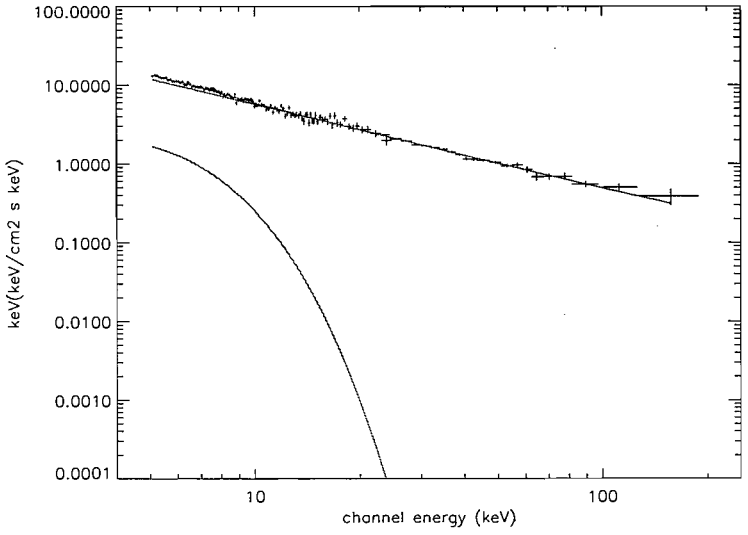

Figure 6.8: IBIS and JEM-X common spectra during the VHS of the source outburst (revolution 63). The data were analysed with OSA software version 5.2.

During the phase of decreasing flux (revolution 103), there was no evidence of a hard tail in the IBIS data (20-250 keV, 2 σ upper limit corresponding to 0.2 $\times$ 10^9erg$\times$cm^{-2}s^{-1}) while the source was clearly detected by JEM-X (see Figure 6.7) and the data fitted with a Disc blackbody component (DISKBB) show a large value of the normalisation constant ($N_{\rm Disk}$, see Table 1), that is proportional to the square of the inner accretion disk radius (Mitsuda et al. 1984). Two months later, close to the end of the outburst (revolutions 119-120), most of the flux is still due to the disc emission but a clear, though faint, Comptonised high energy tail is present in the IBIS data. The IBIS spectra taken during revolution 53 and 119-120, (i.e. at the beginning and at the end of the outburst) are compatible with the same COMPTT model parameters: it is clear that in both cases the source shows a hard tail in the high energy spectrum. Moreover, at the end of the outburst a disc component is still present, as also confirmed by the *RXTE* analysis of the data collected immediately before this *INTEGRAL* observation (from 2003 August 26 to 2003 September 23; Lutovinov et al. 2003).

Revolution	$T_{\rm in}$	$N_{\rm Disk}$	kT_e	τ_p	$N_{\rm Comp}$ $\times 10^2$	χ^2_ν	Deg.of	flux ($\times 10^9$)	Fluxband
-	keV	-	keV	-	-	-	freedom	$erg \times cm^{-2}s^{-1}$	keV
Rev53	-	-	20^{+15}_{-5}	3^{+4}_{-2}	$2.38^{+0.01}_{-0.01}$	0.7	7	$\sim$0.3	(15-250)
Rev56	-	-	24^{+3}_{-3}	$1.5^{+0.2}_{-0.3}$	$8.3^{+0.8}_{-0.7}$	0.96	14	$\sim$7	(20-250)
Rev57-59	-	-	19^{+5}_{-3}	$1.3^{+0.2}_{-0.4}$	$1.5^{+03}_{-0.3}$	1.03	57	$\sim$6	(3-250)
Rev60-61	$1.5^{+0.1}_{-0.1}$	77^{+16}_{-18}	33^{+14}_{-8}	$0.4^{+0.2}_{-0.2}$	8.3^{-2}_{+2}	1.01	106	$\sim$20	(3-250)
Rev103	$1.09^{+0.02}_{-0.02}$	357^{-26}_{+39}	-	-	-	1.09	57	$\sim$3	(3-20)
Rev119-120	$0.87^{+0.02}_{-0.02}$	402^{+344}_{-214}	>13	<3	$1.5^{+5}_{-0.3}$	1.10	68	$\sim$1	(3-250)

Table 6.1: Fit parameter values of the first outburst spectra (90% confidence). $T_{\rm in}$: temperature at inner disk radius; $N_{\rm Disk}=((R_{\rm in}/km)/(D/10kpc))^2 \times \cos(\theta)$, where $R_{\rm in}$ is the inner disk radius, D the distance to the source, and θ the angle of the disk; $kT_{\rm e}$: electron plasma temperature; τ_p: plasma optical depth; $N_{\rm Comp}$: COMPTT normalization constant.

To look for a possible correlation of the flux vs. spectral index we have fitted the IBIS spectra of the first outburst, during revolutions 53, 57, 59-61 and 119-120, with a cutoff powerlaw model. We noticed that the cut off energy of the model had substantially the same value in each fit, so we freeze it to an average value of E=53.3 keV. The reduced spectral fit χ^2_ν covers a range from 0.8 to 1.3. The results, summarised in Figure 6.9, shows that the spectral index has a "circula" or "hysteresis"-like behaviour. The diagram in this figure is directly comparable with the classification of the black hole transients evolution (Fender Belloni & Gallo 2004)

In fact, at the end of the main outburst (revolution 103-120), the source goes back to a hard state, very similar to the one of the pre-outburst IBIS measurements (revolution 53), but in the lower energy range a disk blackbody component is still present.

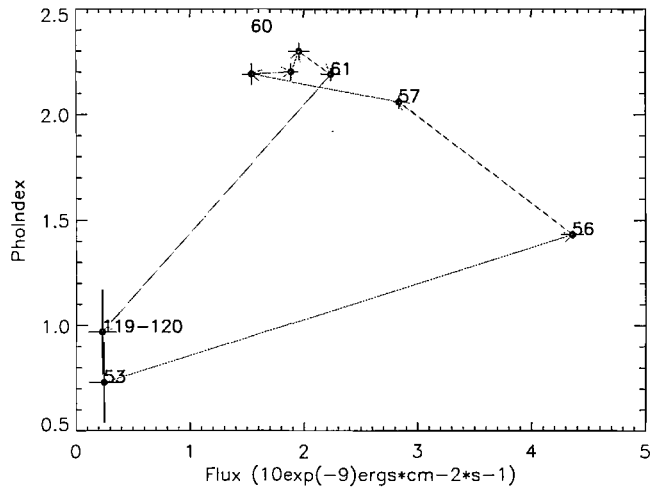

Figure 6.9: Flux vs. powerlaw photon index for every SCW. The labels indicate the revolution number.

6.3.4.2 Second outburst

The spectral analysis presented here is focused on the secondary peak detected by *INTEGRAL* shown in Figure 6.5. The source spectrum varies from the start to the end of the peak. The spectra are all well fitted with a disc blackbody component plus a powerlaw without a cutoff. The spectrum shown in Figure 6.10 represents the peak of the light curves in Figure 6.5. The spectral behaviour indicates, as does the hardness ratio (Figure 6.6), a softening of the source with the presence of a moderate blackbody component ($T_{\rm in}$=1.2 keV) and a hard tail without any cutoff up to 200 keV. The diagram in Figure 6.11 shows the photon index variation of the powerlaw component versus flux (3-200 keV). The diagram shows that the source became softer and brighter and then went back to a harder state creating a sort of loop in the diagram.

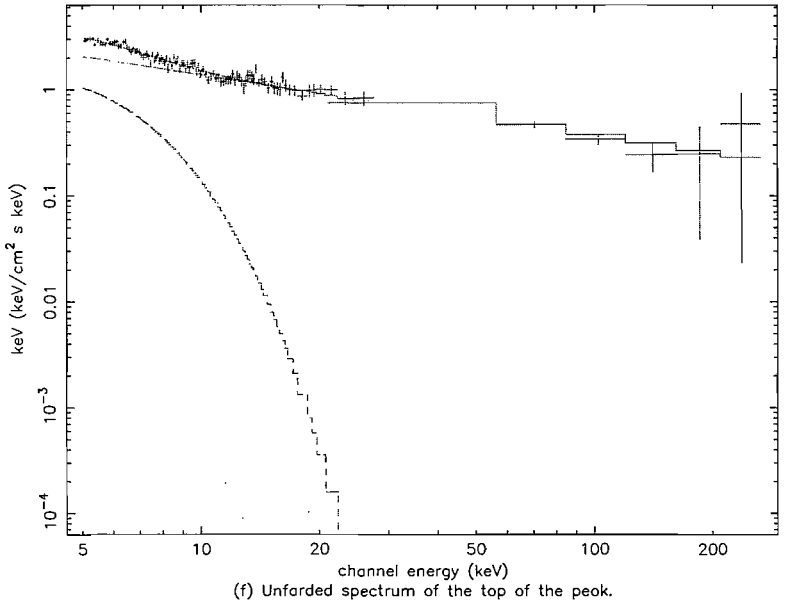

Figure 6.10: Spectrum of the top of the peak shown in Figure 6.5.

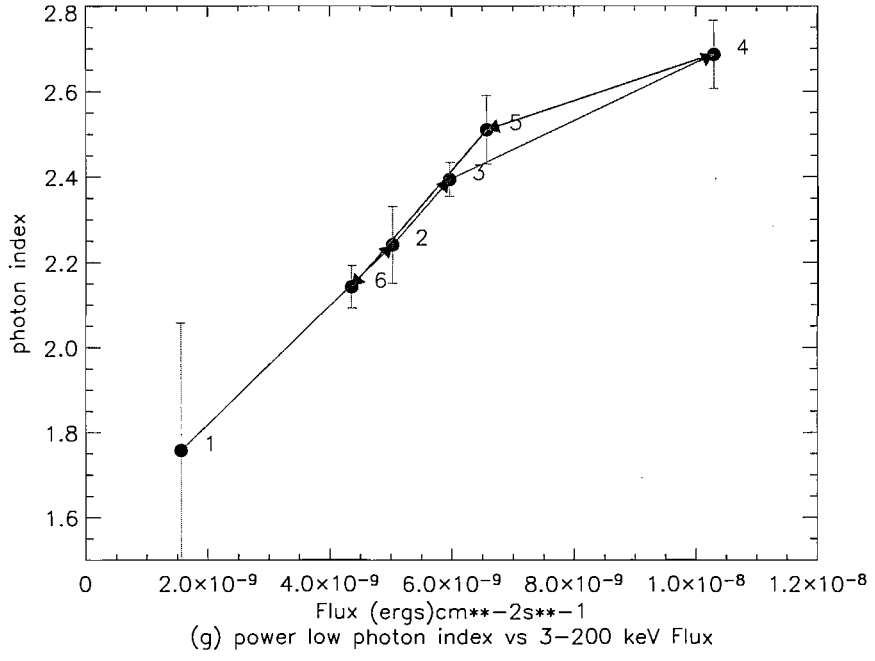

Figure 6.11: Photon index vs. flux of the different spectra during the outburst.

6.4 Discussion and Conclusion

The picture obtained from the spectral analysis can be summarised as follows:

- **Phase 1**. The source is in a "low/hard state". At the beginning of the *INTEGRAL* monitoring campaign (revolution 53) the source has a low luminosity and the bulk of the emission is in the energy range 50-90 keV with a Comptonised hard spectrum (kT_e ~20 keV and τ_p ~3). In this phase there is no evidence of a soft disk component emission. About 10 days later, the amount of accreted matter increases dramatically and in revolution 56 the total emitted energy has increased by a factor of 30: the temperature of the Comptonised plasma is not changed and the optical thickness of the inner part of the corona becomes smaller, i.e. from τ_p~3 to τ_p~1.3 (revolutions 57-59). There is still no evidence of soft emission from the system. The source is still in the hard state, but its flux is increased. Slowly, the peak emission shifts from 70 keV (revolution 53) to 40 keV (revolution 56) and finally to 20 keV (revolutions 57-59). The spectral evolution is shown in Figure 6.7 (top panel). Quite simultaneously a strong radio flare (MJD=52735) is detected (violet arrow in Figure 6.1; Rupen et al. 2003a). Probably the source is approaching the "Soft Intermediate State" (SIMS).

- **Phase 2**. The source is in an "intermediate state" probably a SIMS (revolution 60-61). Over a few days the average amount of energy released increases by a factor of 3 to 5, the optical thickness of the inner part of the corona becomes lower and lower (τ_p ~0.4), the temperature of the hot Comptonised part increases accordingly up to ~40 keV and a bright soft disk component become visible, being responsible for the majority of the system energy release. The fit parameters are compatible with a T_{in} temperature of 1.5 keV and a disk close to the last stable orbit. The spectrum obtained with JEM-X, IBIS and SPI (Figure 6.7, middle panel) has a high statistical significance showing the presence of a substantial Comptonised component.

- **Phase 3.** A few days later the source, probably in high/soft state, reached its maximum, showing a factor of two more flux with high energy behaviour dominated by the thermal emission of the disc. The hard tail without cut-off is probably due to the compton up scattering of non-thermal electrons present in the corona (Zdziarski & Gierliński 2004) or at the base of the jets (Markoff et al. 2001). The source is probably entering a "high soft state" which is also confirmed by the absence of QPOs in the *RXTE* power density spectrum from 8 days later. After this period of observation there is a gap of a few months in the *INTEGRAL* data. During this period 5 *RXTE* pointed observation were made. The results reported by Homan at al. (2005) desribe a further transition to a hard and then back to a soft state. At MJD=52825 the radio observations do not detect any emission from the source. This probably means that the source was in the soft state.

- **Phase 4.** The source is at the end of its "soft state". These observations were performed in revolution 103, a few months after the main peak of the outburst. The energy release has substantially decreased (factor of $\sim$3) and the hard emission has basically switched off.

- **Phase 5.** The source is coming back to the hard state; in revolution 120 a weak hard tail is present again but more than 10 times weaker than in revolutions 60-63. The emission peaks at about 70 keV as in the pre-outburst state (revolution 53). The source is coming back to the hard state and the temperature of the disk dropping to 0.9 keV. Soon afterwards, the source was no longer detectable by *INTEGRAL* ; one month later it was also below the *RXTE*/ASM detection capability.

- **Phase 6.** After about 400 days the source went again into outburst as seen in Figure 6.1 being again active also in the radio band (MJD 53225). Unfortunately the *INTEGRAL* observations cover only the final part of the outburst.

Looking at the *RXTE* hardness ratio (Figure 6.2 bottom panel), as reminded in the previous Sections, it is noticeable that, contrary to the other two outbursts (the first and the third ones), the second outburst of the source starts with a hardening and then comes back to the soft state. This is not common behaviour for a TBHB outburst, but unfortunately the data coverage is not enough to understand better what was happening. The source, during the secondary short 4 days peak of the outburst decay, has a sharp transition to the soft state. The best fit for the high energy data is a powerlaw without any detectable cutoff even near the top of the peak, where the source is bright enough to permit the extraction of the IBIS spectrum up to 200 keV. This suggests, as in the first outburst, the presence of non-thermal processes at work.

Chapter 7

IGR J17091–3624

7.1 History and characteristics of the source

This new source was discovered by *INTEGRAL* /IBIS during a pointed observation on 2003 April 14-15. It was designated IGR J17091–3624 based on its position at R.A. (2000) = $17^h09.1^m$, Dec. = $-36°24.5'$, with an error box of $3'$ at 90% confidence (Kuulkers et al. 2003).

Initially, its flux was ∼20 mCrab in the 40-100 keV energy band exhibiting a hard spectrum, while it was not detected in the 15-40 keV band with an upper limit of ∼10 mCrab. A week earlier, the source was not detected in any energy band, with upper limits of ≃10 mCrab (Kuulkers et al. 2003). During subsequent observations of the GCDE on 2003 April 15-16, the source flux increased to ∼25 mCrab in the 40-100 keV band. It was also included in the *INTEGRAL* IBIS/ISGRI galactic plane survey catalogue (Bird et al. 2004) and classified as unknown. Observations with the Very Large Array revealed the presence of a possible radio counterpart with a steeply falling spectrum typical of synchrotron emitters (Rupen et al. 2003b). This

was also confirmed by a subsequent observation with the Giant Metrewave Radio Telescope (Pandey et al. 2006).

Immediately after the *INTEGRAL* discovery, an *RXTE* observation was performed. The analysis of the *RXTE* data showed a relatively stable source flux without features associated with quasi-periodic oscillations in the power spectrum. Based on the energy and power spectra, Lutovinov & Revnivtsev (2003) suggested that IGR J17091–3624 is an X-ray binary in the low/hard state and probably a black hole system. IGR J17091–3624 was then searched for in the X-ray catalogs and detected in the archival data of both the TTM telescope on board the KVANT module of the *Mir* orbital station (Revnivtsev et al. 2003b), and in the *BeppoSAX* WFC (Rupen et al. 2003a). Following this, Lutovinov et al. (2005) performed a preliminary study of the IBIS/ISGRI spectrum of the source, showing that its flux changed by a factor of $\sim$2 between 2003 April and 2003 August-September. During 2003, the source spectrum was described by a simple powerlaw with a photon index of $\Gamma \simeq 2.2$ in the 20-150 keV energy band, i.e., softer than the *RXTE* spectrum. As the source flux in the hard X-rays increased in 2004, the spectrum became harder with $\Gamma \simeq 1.6$. From the above investigations, IGR J17091–3624 appears as a moderately bright variable (probably a transient) source with flaring activity in 1994 October (*Mir*/KVANT/TTM), 1996 September (*BeppoSAX*/WFC), 2001 September (*BeppoSAX*/WFC, in 't Zand et al. 2003), and 2003 April (*INTEGRAL* /IBIS, Kuulkers et al. 2003).

7.1.1 Improvements over previous analysis

We have performed a more accurate spectral analysis of this source compared to those reported in previous publications, analysing all the available *INTEGRAL* data (the source was detectable until the end of 2004 April). The new set of data allowed

us to fit a joint *RXTE/INTEGRAL* spectrum of IGR J17091–3624 in the low/hard state.

We obtained spectral coverage with IBIS up to 150 keV fitting the data with detailed models, thus obtaining new information on the geometry of the source and on the accretion disk optical depth and temperature. We have also extracted a JEM-X spectrum that confirms the previous hypothesis of a transition to the soft state (Lutovinov et al. 2003) and furthermore we have found suggestions of a hysteresis-like behaviour in the source spectral evolution, with the hard-to-soft state transition occurring at higher luminosity than the soft-to-hard transition. We then speculate on the source nature, even if the final picture is still not evident. The results of this work were published on the Astrophysical Journal in 2006 (Capitanio et al. 2006c).

7.2 Data Analysis

We analysed the data set consisting of all *INTEGRAL* (Winkler et al. 2001) Core Program and public observations in which IGR J17091–3624 was within the IBIS field of view, and of the *RXTE* Proportional Counter Array (PCA, Bradt et al. 1993) data collected during the 2 ks observation performed on 2003 April 20. The *INTEGRAL* observations, though not continuous, cover a period of one year from 2003 April to 2004 April. The *RXTE* observation corresponds to a period between *INTEGRAL* revolution 61 (2003 April 14-16) and the beginning of revolution 63 (2003 April 21). Table 7.1 summarises the *INTEGRAL* observations of the source. Light curves, hardness ratio and spectra are then obtained for each individual SCW. We use here *INTEGRAL* data from the coded mask imager, IBIS. Then, in order to obtain broad-band spectra, we add the lower energy data from the PCA, and, whenever available, those from the *INTEGRAL* X-ray Monitor, JEM-X.

Table 7.1: The log of the *INTEGRAL* observations of IGR J17091–3624 used for the spectral fits.

Revolution	Start Date	End Date	ISGRI exposure [ks]
61-63[a]	2003-04-12	2003-04-21	15
100-119	2003-08-10	2003-10-04	77
164-185	2004-02-17	2004-04-02	77

[a] Including the 2-ks *RXTE* observation on 2003-04-20.

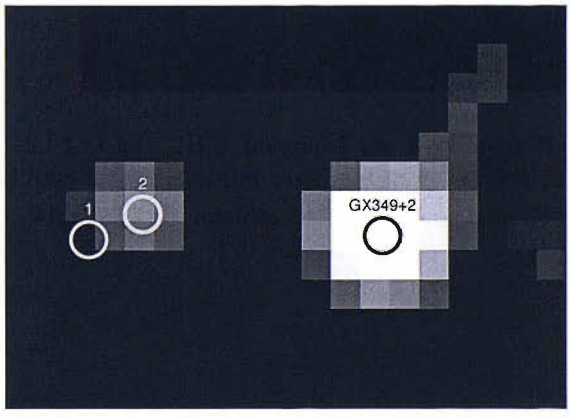

Figure 7.1: The 20-150 keV IBIS image of the field near IGR J17091–3624. It can be seen that IGR J17098-3628 (1) is not visible during the *RXTE*/PCA observations of IGR J17091–3624 (2), which argues against any contamination in the PCA field of view.

Figure 7.1 shows the 20-150 keV *INTEGRAL* image of IGR J17091–3624 during the period of the *RXTE* observation. The figure shows that the transient source IGR J1709.8-3628, detected 9.4′ from IGR J17091–3624 on 2005 March 24 (Grebenev et al. 2005), was not visible. This rules out any contamination of other sources in the *RXTE*/PCA field of view. The data set has been divided in two subsets according to the source position being either within the partially coded field of view (PCFOV, 19° × 19°) or in the narrower fully coded field of view (FCFOV, 9° × 9°). Both data sets have been used to produce the source light curves in different energy ranges while only FCFOV data have been used for spectral extraction because of the better signal to noise ratio. Since the IBIS spectra do not show any substantial variability during 2003 April 14-21, we have integrated the spectrum over this observation period. While IBIS provides a large FOV, $> 30°$, that of JEM-X is narrower ($> 10°$), thus providing only a partial overlap with the high energy detector. In general, the effective JEM-X exposure is ∼15% of that of IBIS. Therefore, a combined JEM-X/IBIS spectrum was possible only for a small fraction of the data.

We have extracted the PCA spectrum and the light curve from the *RXTE* public data archive[1]. When spectral data are obtained in the same time interval from more than one instrument, we allowed a free relative overall normalisation constant for each instrument with respect to IBIS.

7.3 Results

[1]http://heasarc.gsfc.nasa.gov/docs/xte/xte_public.html.

7.3.1 Time evolution

IGR J17091–3624 is a very faint source, which is often below the detection limits of IBIS and JEM-X in a single 2000-s SCW (~5 mCrab in the 20-100 keV IBIS energy range, and ~23 mCrab in the 3-20 keV JEM-X energy range). Furthermore, most of the JEM-X data were not in its FCFOV, which is partly due to the pointing algorithm of the GCDE. As a result, the JEM-X effective exposure was ~10 times shorter than that of IBIS.

We have followed the IBIS evolution of the source flux from the first *INTEGRAL* detection of the source. First, a flux increase took place in the first SCWs of revs. 61-63 (2003 April 14-21), as can be seen in Figure 7.2. We have also found a very faint signal in the data of revolution 60.

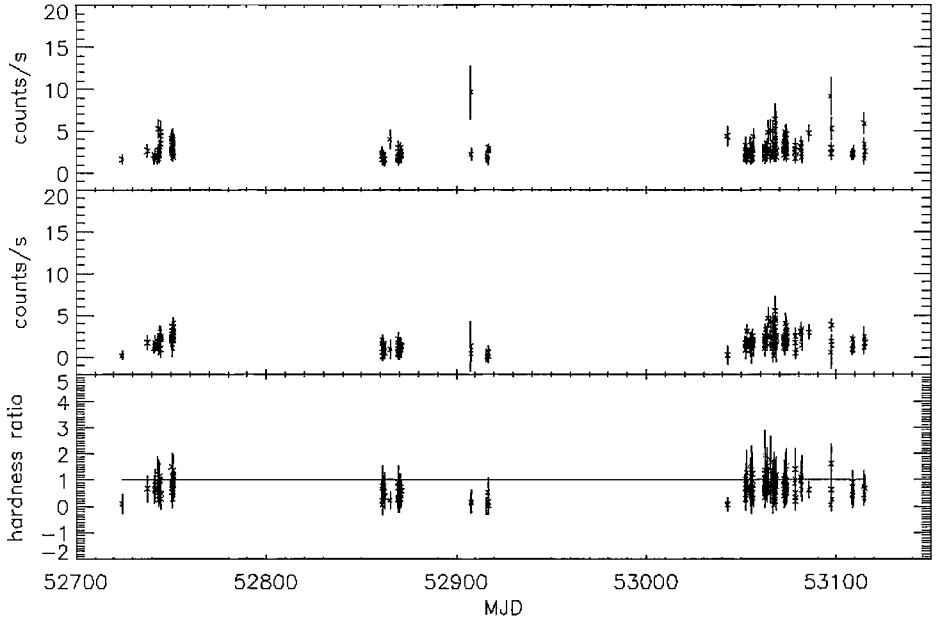

Figure 7.2: The 20-40 keV and 40-100 keV light curves (the top and middle panel, respectively) and the corresponding hardness ratio (the bottom panel), with the solid line representing a value of 1.

We have analysed the data until rev. 185 (2004 April 19-20), as later observations do not show any signal in the direction of the source at least until rev. 232 (2004 September), the current limit of the public data set at the time of our analysis. We have produced IBIS light curves in two different energy bands, 20-40 and 40-100 keV (the top and middle panel, respectively, of Figure 7.2). The light curves are derived from the flux and variance maps for each individual SCW by extracting values directly from the derived source positions. Differences in the size of the error bars on individual points are due to both different SCW exposures and different source locations within the field of view. The bottom panel of Figure 7.2 shows the hardness ratio, $HR \equiv R_{40-100}/R_{20-40}$, where R is the count rate. During MJD 52860-52924 (2003 August-October), the source was rather faint, especially in the 40-100 energy range, and the hardness ratio shows a weak indication of softening corresponding to 25%.

The *RXTE* observation lasted only 2 ks, so that it has not been possible to extract information on the long-term temporal behaviour. A detailed timing analysis of the 2-ks data set is given by Lutovinov & Revnivtsev (2003).

For the third observation period, during MJD 53054-53097 (2004 February-April), only IBIS data were available. The light curves are characterised by an increased flux with respect to the previous periods together with a faint tendency of source hardening.

7.3.2 Spectral evolution of IGR J17091–3624

We have studied the spectral behaviour separately for 3 epochs:

1) revolutions 61-63 (2003 April 15-21, ~15 ks), which is the first *INTEGRAL* observation combined with the *RXTE*/PCA data;

2) revolutions 100-119 (2003 August-October, ~77 ks), during which the IBIS spectrum softened, and which includes the only JEM-X detection;

3) revolutions 165-185 (2004 April, ~77 ks), containing only the IBIS data.

The data sets have been fitted with XSPEC tools. Several models have been tested for each of the data sets. In our fits, we have confirmed the constraint found by Lutovinov & Revnivtsev (2003), $N_{\rm H} < 10^{22}$ cm^{-2}, which is also in agreement with the galactic column density along the direction to the source, $\simeq 8 \times 10^{21}$ cm^{-2} (http://heasarc.gsfc.nasa.gov). For revs. 61-63, the relatively high brightness and the lack of variability have allowed us to obtain a combined IBIS/PCA spectrum (see Figure 7.4). We use two thermal Comptonization models, COMPTT (Titarchuk 1994) and COMPPS (Poutanen & Svensson 1996), both assuming a slab geometry. The COMPPS model is an accurate iterative-scattering model, in which subsequent photon scatterings are directly followed. It has been extensively tested against Monte Carlo results, e.g., by Zdziarski, Poutanen & Johnson (2000). On the other hand, COMPTT is based on an approximate solution of the kinetic equation with some relativistic corrections, and the resulting spectra are also only approximate (see the appendix of Zdziarski, Johnson & Magdziarz 1996). For the COMPPS model, we assumed a viewing angle of 60° and the source of seed photons to be at the slab bottom (the model geometry parameter was set equal to 1) with a blackbody distribution at $kT_{\rm bb} = 0.1$ keV. For the COMPTT model, we used Wien seed photons with the temperature as above. The free parameters of each model are the electron temperature, $kT_{\rm e}$, the Thomson optical depth, τ, and the normalization, N. There is no evidence of a Compton reflection component, and the weak fluorescent *Fe Kα* line present in the spectrum appears mostly due to the galactic ridge emission (Lutovinov & Revnivtsev 2003). Table 7.2, the left panel of Figure 7.3 and the red curve in Figure 7.4 show our results.

The results corresponding to revs. 100-119 consist of the combined JEM-X (6 SCWs) and ISGRI average spectra. Given the difference in the JEM-X and ISGRI exposures, we have also compared the ISGRI count rate for the 6 SCWs for which the JEM-X spectrum was obtained, and found it is almost the same as the count rate averaged over the entire period of revs. 100-119. We have analysed in detail the JEM-X data in order to exclude any possible contamination from close by sources, IGR J17091–3624 being located in a crowded region near the galactic center.

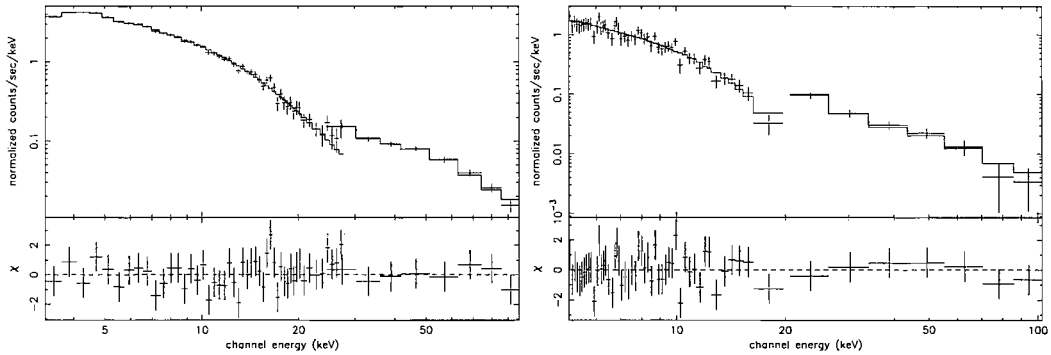

Figure 7.3: Left panel: the *RXTE*/IBIS count spectra for revs. 61-63; Right panel: the JEM-X/IBIS count spectra for revs. 100-119.

The source shows a bright component in soft X-rays, followed by a weak high-energy tail. Thus, we have used the model consisting of a disk blackbody (DISKBB, Mitsuda et al. 1984) and a powerlaw spectrum. Table 7.3 summarizes our results, and the spectrum is shown in the right panel of Figure 7.3 and in the blue curve in Figure 7.4.

We clearly see a transition from the hard to the soft state from the first to the second epoch. After this, the source returns to the hard state, as shown by the IBIS data for revs. 164-179, green spectrum in Figure 7.4. The epoch 3 IBIS data are fitted by COMPTT with $kT_e = 21^{+4}_{-4}$ keV and $\tau = 2.7^{+1.2}_{-0.5}$; these values are similar to those of epoch 1 (Table 7.2).

Table 7.2: The fit parameters to the PCA/IBIS spectrum of revs. 61-63 with the COMPTT and COMPPS models (see the red spectrum in Figure 7.4).

model[b]	kT_e keV	τ	χ^2/ν	d.o.f	F(3-100 keV) erg cm^{-2} s^{-1}
COMPTT	24^{+9}_{-4}	$2.1^{+0.3}_{-0.5}$	0.93	54	2.5×10^{-10}
COMPPS	31^{+12}_{-4}	$2.3^{+0.2}_{-0.4}$	0.96	54	2.4×10^{-10}

[b] $N_H < 10^{22}$

Table 7.3: The fit parameters to the JEM-X/IBIS spectrum of revs. 100-119 with the disk blackbody and a powerlaw model (see the blue spectrum in Figure 7.4).

Model	kT_{in} keV	N_{disk}	Γ	N_{pl}[c]	χ^2/ν	d.o.f.	F(3-100 keV) erg cm^{-2} s^{-1}
DISKBB+POW	$2.6^{+0.2}_{-0.2}$	$1.9^{+0.7}_{-0.6}$	$2.1^{+0.3}_{-0.4}$	$0.2^{+0.4}_{-0.1}$	1.0	53	2×10^{-9}

[c] keV^{-1} cm^{-2} s^{-1} at 1 keV.

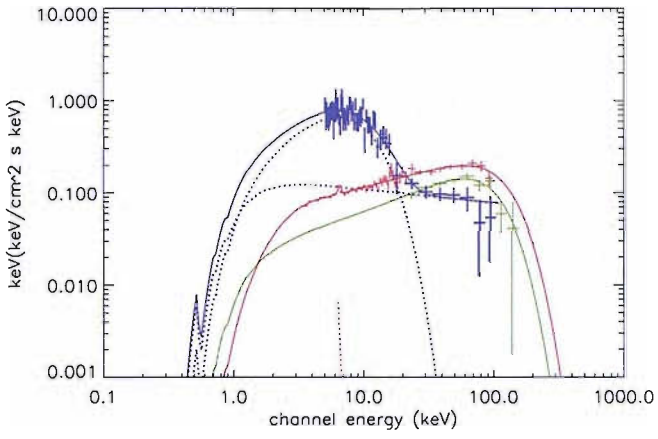

Figure 7.4: The unfolded spectra showing the source evolution during the *INTEGRAL* and *RXTE* observations. The red spectrum (PCA/IBIS) corresponds to revs. 61-63, the blue spectrum (JEM-X/IBIS) corresponds to revs. 100-119, and the green spectrum (IBIS) corresponds to revs. 164-185. The *Fe* $K\alpha$ line, shown by the red dotted curve, is due to the galactic ridge emission. The blue dotted curves denote the disk blackbody and powerlaw components of the models.

The spectral evolution of IGR J17091–3624 shows both similarities and differences with respect to that of the black hole candidate IGR J17464–3213 (see Chapter 6). Therefore, we report here the spectra and fit results for that object as well. Table 7.4 shows fit results with both COMPTT and COMPPS for the hard state and Figure 7.5 shows a comparison of its hard and soft states with those of IGR J17091–3624.

7.4 Discussion and conclusions

We have followed the evolution of an outburst of IGR J17091–3624. Within the course of less than one year, the source went from the hard to the soft state and then back to the hard state.

Table 7.4: The fit parameters to the hard-state spectrum of the black hole candidate IGR J17464–3213 (= H1743–322, Capitanio et al. 2005) with the COMPTT and COMPPS models (see the light green spectrum in Figure 7.5).

model	kT_e	τ	χ^2/ν	d.o.f	F(3-100 keV)
	keV				erg cm^{-2} s^{-1}
COMPTT	18^{+4}_{-2}	$1.3^{+0.2}_{-0.4}$	1.05	119	6×10^{-9}
COMPPS	20^{+3}_{-1}	$2.0^{+0.1}_{-0.2}$	1.04	119	4×10^{-9}

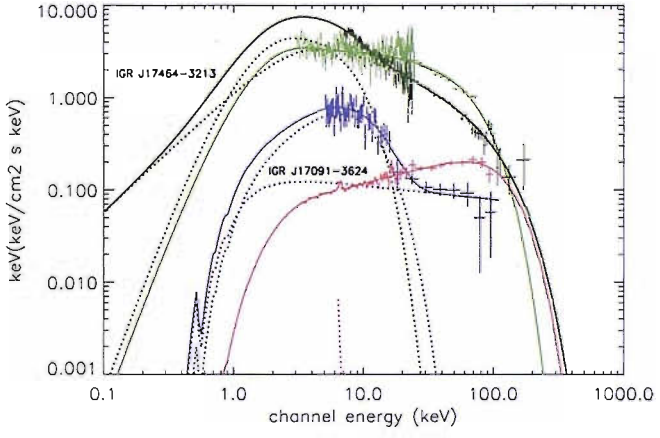

Figure 7.5: The spectra of IGR J17091–3624 during the rising part of the outburst (red: hard state; blue: soft state), compared with the spectra of IGR J17464–3213 also corresponding to the rising part of its outburst (dark green: soft state; light green: hard state). The blue and red dotted curves denote the same model components as in Fig. 7.4. The dark green dotted curves denote the blackbody and thermal-Compton components of the corresponding fit.

We consider here the standard hard-state model with the dominant radiative process being thermal Comptonization of disk blackbody photons. An intriguing feature of our hard-state spectra is the rather low electron temperature, ~20 keV, while the range of temperatures typical for black hole binaries is ~50-100 keV (e.g., Zdziarski & Gierliński 2004). This low temperature is obtained using both the COMPPS and COMPTT models, and for both occurrences of the hard state, in the rise and decline. Such a low temperature may be a characteristic of the hard state of neutron-star low-mass X-ray binaries, although at present it is rather poorly constrained (e.g., Gierliński & Done 2002). On the other hand, we might have caught the source during transitionary phases, with enhanced Compton cooling due to the increasing flux of disk blackbody emission and the correspondingly lower electron temperature.

During the soft state in epoch 2, the peak of the $EF(E)$ emission is at several keV, as compared to the ~100 keV peak in the hard state. There is a high-energy tail, but its weakness does not permit us to put constraints on its origin.

IGR J17091–3624 is located 10° from the galactic centre region, where the highest concentration of LMXRBs in the Galaxy is present (White & van Paradijs 1996). The model unabsorbed bolometric (0.01-500 keV) luminosities in the hard (revs. 61-63) and soft state (revs. 100-119), assuming a distance of 8.5 kpc and isotropy, are $L \simeq 1 \times 10^{37}$ erg s^{-1} and $L \simeq 2 \times 10^{37}$ erg s^{-1}, respectively. These values are not far from those characteristic to the hard and soft states of black hole binaries (e.g., Zdziarski & Gierliński 2004), although the neutron-star nature of the source cannot be excluded. On the other hand, the *RXTE* power spectrum, without QPO-like features and with band-limited noise (Lutovinov & Revnivtsev 2003), commonly observed in black hole binaries in the low/hard spectral state, as well as the probable correlation with a radio source (Pandey et al. 2006; Rupen et al. 2003b) may also argue for the black hole nature of this source.

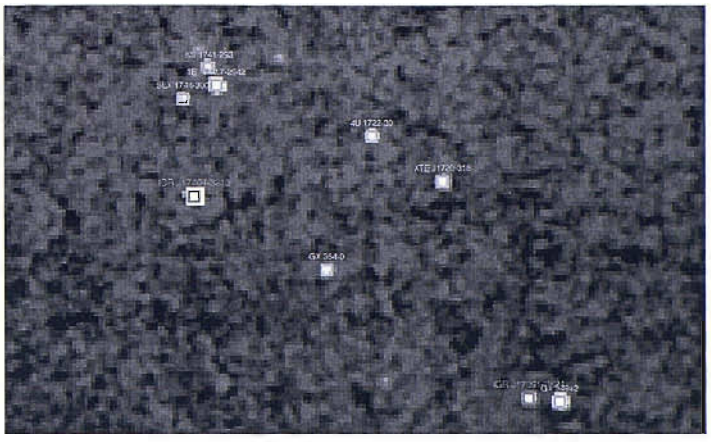

Figure 7.6: galactic centre region IBIS image between 20-40 keV covering a period in which both IGR J17091–3624 and IGR J17464–3213 were in outburst.

7.4.1 Similar properties between IGR J17091–3624 and IGR J17464–3213

In Section 7.3.2, we have also compared the evolution of IGR J17091–3624 with the other *INTEGRAL* transient source, a BHC, presented in this thesis, IGR J17464–3213. Figure 7.6 shows the IBIS image between 20-40 keV of the galactic centre zone in a period in which both IGR J17091–3624 and IGR J17464–3213 were in outburst. Both sources show similar spectral evolution during outbursts of similar duration. However, as shown in Figure 7.5, the hard-state spectrum of IGR J17464–3213 is substantially softer than that of IGR J17091–3624, although both sources share the relatively low electron temperature of $\sim$20 keV. Furthermore, the relative normalisation of the observed hard and soft state spectra is different. Curiously, the high-energy parts ($\gtrsim$30 keV) of both spectra of IGR J17464–3213, are virtually identical. The various amplitudes of the hard and soft state spectra are often seen in X-ray transients (e.g., Zdziarski et al. 2004), and are due to the hysteretic behaviour of the accreting systems.

7.4.2 New open questions on IGR J17091–3624 from optical observations

In a recent work (Negueruela & Schurch 2007) a probable optical counterpart of IGR J17091–3624 has been identified in photometric catalogue archives as a late F star. This could confirm the hypothesis made in this Chapter that the source is a low-mass X-ray binary. Another important characteristic of this late F star is its distance, that seems to be around 800-pc, certainly much closer than the galactic bulge, where most of the low mass X-ray binaries reside. If this counterpart will be confirmed, it could open a new scenario on IGR J17091–3624: a BHC with very faint outbursts, not belonging to the galactic bulge, but very near to us.

Chapter 8

BeppoSAX WFC sky

8.1 Introduction and aim of the work

During 6 years of the *BeppoSAX* (Boella et al. 1997a) operational life, the Wide Field Camera (WFC) observations covered almost the full sky at different epochs. The energy coverage, the wide field of view and the imaging capability share some common characteristics with IBIS. A comparison between the IBIS sources catalogue and the WFCs one, especially in the overlapping energy range of the two instruments, can be very useful in order to better understand the nature of the sources detected in the IBIS survey. Since a final catalogue of the sources detected with the WFCs has not been published yet, the aim of the work, described in this Chapter, is to analyse all the Wide Field Camera pointings available in two different energy bands producing a mosaic of the images of all the single pointing observations and search the map for sources as has been made for the IBIS survey. This work represents the first unbiased source list compilation produced in this way from the overall WFC data set. Besides its application to IBIS, this work is useful in its own right,

demonstrating the effectiveness of the WFC and the archival dataset it has produced.

8.2 BeppoSAX satellite

In this Section the principal characteristics of the *BeppoSAX* mission and payload are briefly summarised. The *BeppoSAX* (acronym for the Italian Satellite for X-ray Astronomy, *SAX*) mission was a program of the Italian Space Agency (ASI) with participation of the Netherlands Agency for Aerospace Programs (NIVR). It has been developed with the support of a consortium of institutes in Italy and in The Netherlands and the Space Science Department of ESA. After launch it was named *BeppoSAX* in honor of Giuseppe (Beppo) Occhialini. *BeppoSAX* was launched on April 30, 1996 by an Atlas 1-Centaur from Cape Canaveral into a 600 km orbit at 4 degrees inclination.

8.2.1 The scientific payload

The payload is characterised by a wide spectral coverage from 0.1 to 300 keV. The configuration of the scientific payload and the energy bands covered by the different instruments are presented in Figure 8.1 and Figure 8.2 respectively.

A set of instruments co-aligned with the Z axis of the satellite (see Figure 8.1), called Narrow Field Instruments (NFI), consisted of:

- MECS (Medium Energy Concentrator Spectrometers): a medium energy (1.3-10 keV) set of three identical grazing incidence telescopes with double cone geometry, with position sensitive gas scintillation proportional counters in their focal planes (Boella et al. 1997b).

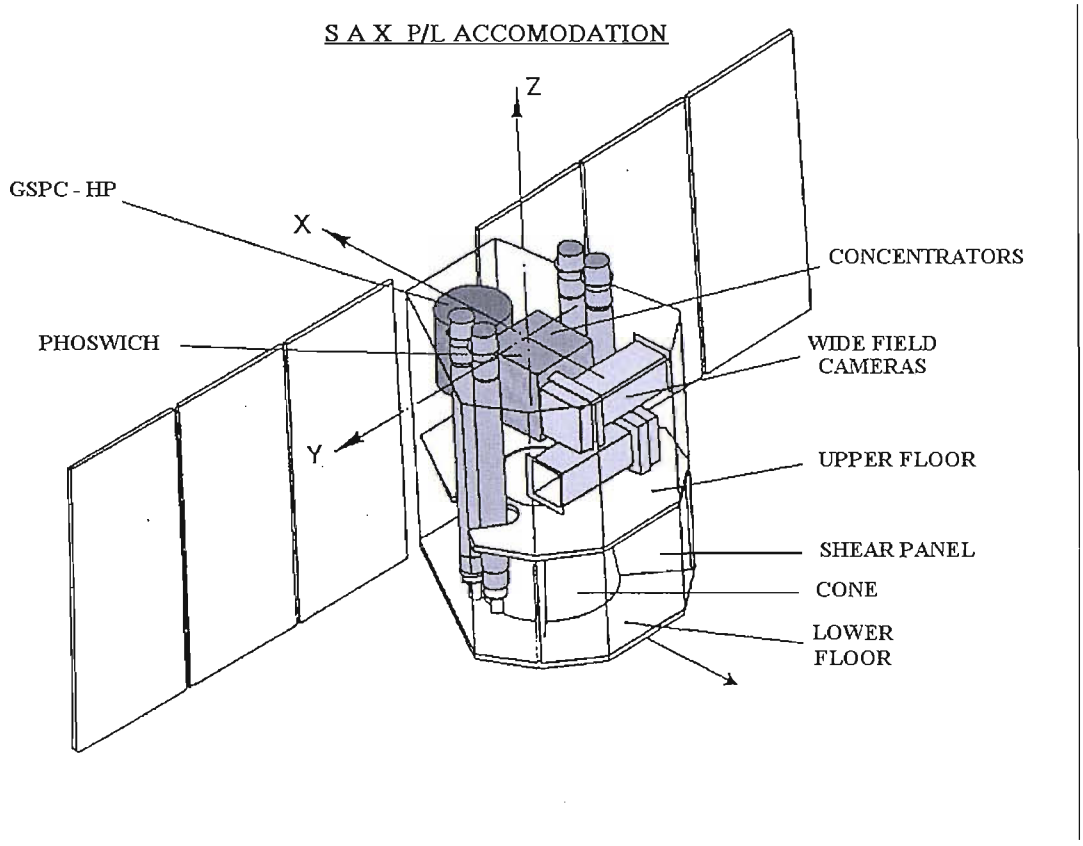

Figure 8.1: *BeppoSAX* scientific payload accommodation.

- LECS (Low Energy Concentrator Spectrometer): a low energy (0.1-10 keV) telescope, identical to the other three, but with a thin window position sensitive gas scintillation proportional counter in its focal plane (Parmar et al. 1997).

- HPGSPC, a collimated High Pressure Gas Scintillation Proportional Counter operating between 4-120 keV, (Manzo et al. 1997).

- PDS, a collimated Phoswich Detector System operating between 15-300 keV, (Frontera et al. 1997).

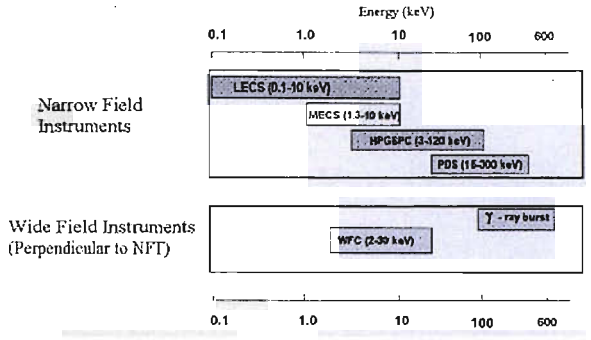

Figure 8.2: Energy coverage of *BeppoSAX* Instrument.

8.2.2 BeppoSAX WFC

Perpendicular to the axis of the NFI and pointed in opposite directions there were two coded mask proportional counters, the Wide Field Cameras (Jager et al. 1997), that provided access to large regions of the sky in the range 3-28 keV. Each WFC had a field of view of 20° × 20°(FWHM) with an angular resolution of 5′. The two *BeppoSAX* WFCs were shadow mask cameras: a two-dimensional position and energy sensitive detector (Multi Wire Proportional Counter) placed behind an opaque screen with a pseudo random array coded mask. The WFCs had a high sensitivity over a large field of view and at the same time a good angular resolution over the whole field due to small mask holes (See Table 8.1 for details). Figure 8.3 shows an image of one of the WFC.

The detector and the mask had nearly the same sizes of 25.5 × 25.5 cm^2 and 25.6 × 25.6 cm^2, respectively. A stainless steel structure between the detector and the mask allowed the X-ray photons to reach the detector through the mask only and fixes the position of the mask 0.7 m away from the detector. In front of the mask a 6 μm thick kapton foil was placed as a thermal shield. The field of view was 20 square degrees (FWHM) although sources could be detected with less sensitivity in a field of 40° × 40° in total. The angular resolving power of 5 arcmin (FWHM),

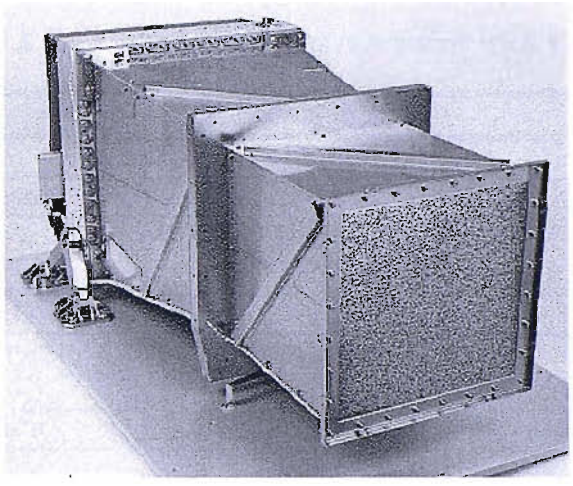

Figure 8.3: View of one of the *BeppoSAX* Wide Field Cameras

was determined by the mask-to-detector distance, the size of the mask elements, 1×1 mm^2, and the detector position resolution. The source location accuracy was better than one arcminute, limited mainly by the satellite pointing stability and the statistical noise of the observed sources. The energy resolution was 20% at 6 keV and 22% at 22 keV. The limiting sensitivity was a few mCrab in 10^5 s but varied with the number of sources in the field of view and thus with the pointing direction in the sky. At high galactic latitudes the noise was dominated by the diffuse X-ray background (130 cts/s) plus the detector background (20 cts/s) while near the galactic plane the main contribution was from strong X-ray sources.

8.3 WFCs sky map production

The two WFCs were mounted 180 degrees away from each other and perpendicular to the pointing direction of the Narrow Field Instruments (NFI), looking at two different sky zones during any NFI pointing. In this way, during the 6 years of *BeppoSAX* operational life, the WFCs secondary mode observations covered all the

Table 8.1: *BeppoSAX* WFCs characteristics compared with the IBIS/ISGRI ones.

parameter	WFC value	ISGRI value
Energy range	3-28 keV	17 keV - 1MeV
Energy resolution	20% at 6 keV	8% at 100 keV
Field of view	$40° \times 40°$ (FWZR) $20° \times 20°$ (FWHM)	$29° \times 29°$ zero response ($8.9° \times 8.9°$ FCFOV)
Angular Resolving Power	5'	12'
Source location accuracy	$<$ 1 arcminute	3 arcminute at 100 keV (5 σ) 50 arcseconds at 100 keV (50 σ)
Sensitivity in $10^3 s$	~10 mCrab (3-28 keV)	~30 mCrab (20-40 keV)

sky, with at least one pointing, in the range of 1.8-28 keV. Moreover, two times a year (autumn and spring), the WFCs observed, as the primary *BeppoSAX* instrument, the galactic bulge region for an average of one day per week (In 't Zand 2001). The time devoted to this program corresponds to 8% of the total observing time. Twelve such campaigns were carried out amounting to a total net exposure up to 6 Msec.

The WFCs data are organised in short observational periods (OP) of at least 100 ks. Each pointing exceeding 100 ks is divided into more than one OP. We selected all the OPs available in the archive of the IASF institute of Rome. Some of the OPs were corrupted, so that only 70% of the total amount of OPs have been chosen for the analysis. After the analysis a filter has been applied again in order to eliminate the noisy images, so at the end the final amount of data corresponds to 60% (100 Ms) of the total observation time. Figure 8.4 shows the final exposure map: the collected data covered all the sky although not uniformly, in fact there are zones with higher exposure such as the galactic center or the zone around the Polaris star (and the "anti" Polaris zone). This is due to the observing strategy and manoeuvre techniques of the *BeppoSAX* satellite. The averaged exposure is about 1×10^4 s, even if there are some regions with an exposure of two orders of magnitude less. Nevertheless these regions are quite small covering a zone with a radius of about 10

degrees.

We analysed all the selected OPs with the *BeppoSAX*/WFCs Data Analysis System, extracting the images for two energy ranges: 3-17 keV and 17-28 keV. The latter band was selected to allow a direct comparison between WFCs and IBIS. The WFC standard software uses the IROS method to extract sources from the shadowgrams of the WFC coded masks. Following the IROS procedures, we forced the software to extract a big number of sources for each OP images, effectively cleaning down into the noise. A mosaic of images, for both energy ranges, produced by IROS software, has been generated using the same software used for the IBIS survey. In this way the eventually false detections extracted by "stressing" the WFC software have been eliminated. Two final maps have been obtained as shown in Figure 8.5 and Figure 8.6.

8.3.1 Source search and localization

The sources' position and flux were identified using a barycentering method to determine the centroid of the source profile. The mean flux of the sources was determined from the count rate at the position of the source maximum significance, using the same software developed for the IBIS survey. A second method based on SExtractor 2.4.4 software (Bertin & Arnouts 1996) has been used to cross check the results. The list of excesses was then checked manually. After all the checks the final list contains 236 excesses. Of these excesses 215 were identified and classified as sources, while 21 do not have a firm identification. Of these 21 excesses, after a filtering and a visual inspection of the maps, only two have been chosen as new source candidates. All the WFCs excesses were compared with the *INTEGRAL* lowest energy range maps, 18-60 keV and 20-100 keV, while the 17-30 keV map was not considered because of its high noise.

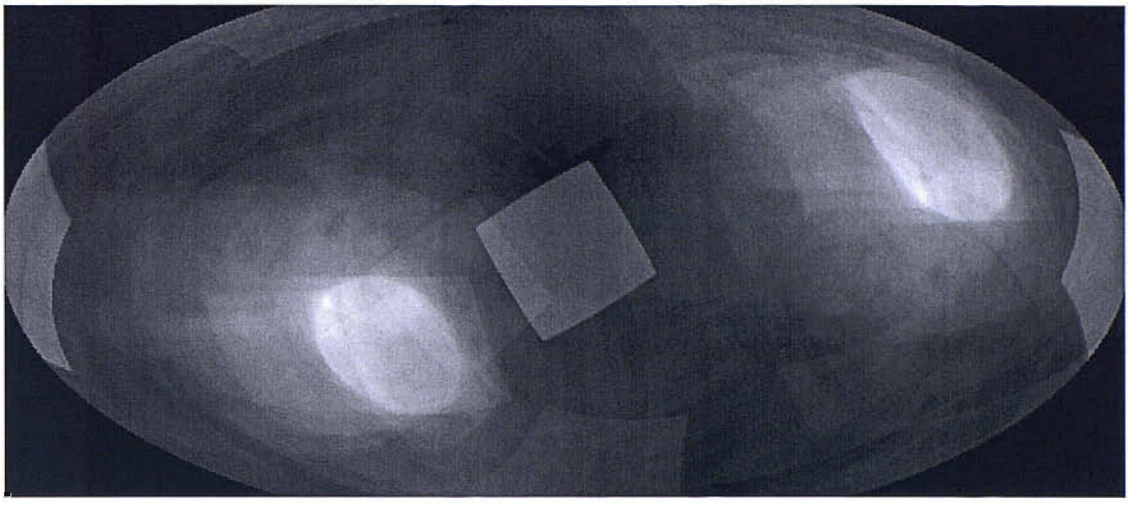

Figure 8.4: Exposure final map of the WFCs images mosaic.

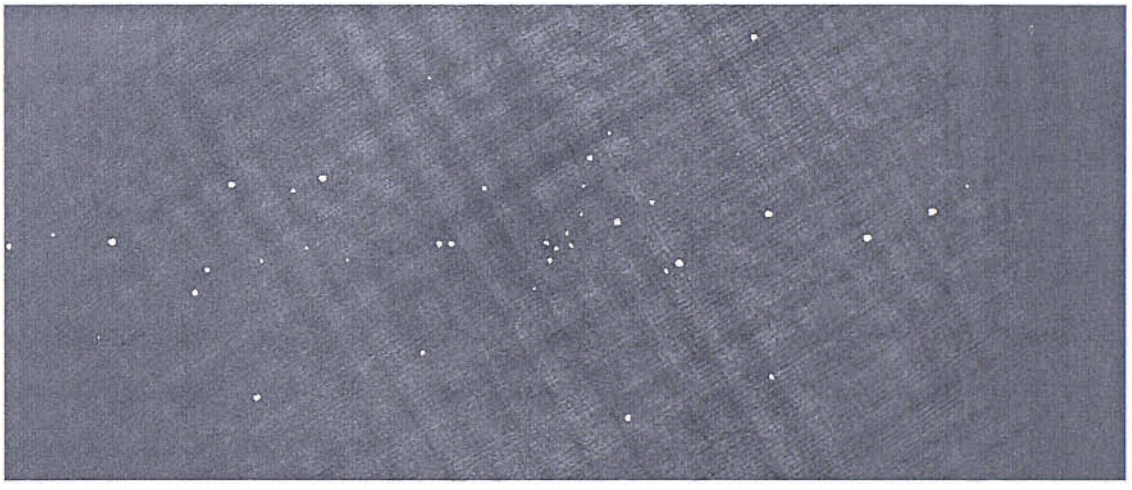

Figure 8.5: WFCs final mosaic between 3-17 keV: Zoom of the galactic centre region.

8.4 Correlation between the IBIS and WFC maps

The *INTEGRAL* and WFC source lists have been compared, both for understanding systematic effects in IBIS survey and for extrapolating more information on the characteristics of the sources, such as recurrency and duration of outbursts as well as spectral and time variability. We correlate the two excesses lists obtaining two

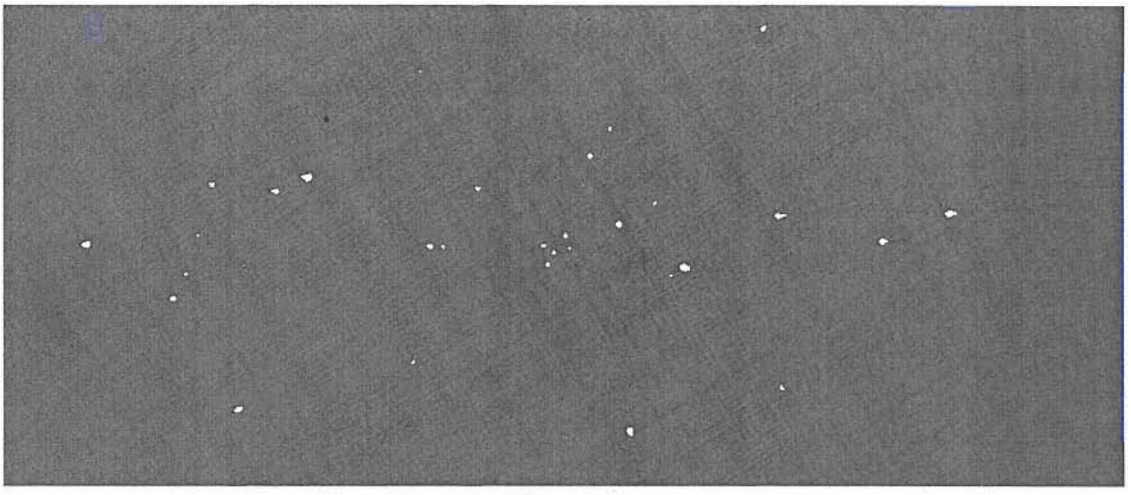

Figure 8.6: WFCs final mosaic between 17-28 keV: Zoom of the galactic centre region.

different lists of sources: the first contains all the excesses detected by both IBIS and WFCs while the second contains the sources detected only by WFCs. The overall list of the sources detected by WFCs mosaics are plotted in Table 8.2, at the end of this Chapter, with their name, coordinates, significance in the two energy bands, exposure time and source type [1]. 85 of these sources (bold font sources in Table 8.2) are the ones not detected in IBIS survey maps while 129 are detected by both IBIS and WFCs. Figure 8.7 shows the different type distribution of the detected sources, respect to their total number, for both IBIS and WFCs catalogue. The distribution is different for the two instruments and this is mainly due to their different energy coverage, exposure and sensitivity: as Figure 8.7 shows, the sources of the IBIS survey catalogue present a higher percentage of both AGNs and unidentified sources with respect to the WFC catalogue. Otherwise the WFCs catalogue lists a higher percentage of clusters of galaxies and low-mass X-ray binaries.

In order to understand the reason why some sources have been detected only in the WFCs mosaics, Figure 8.8 shows the difference in % of the source types detected only

[1]The sources have been classified according to the SIMBAD and NED databases

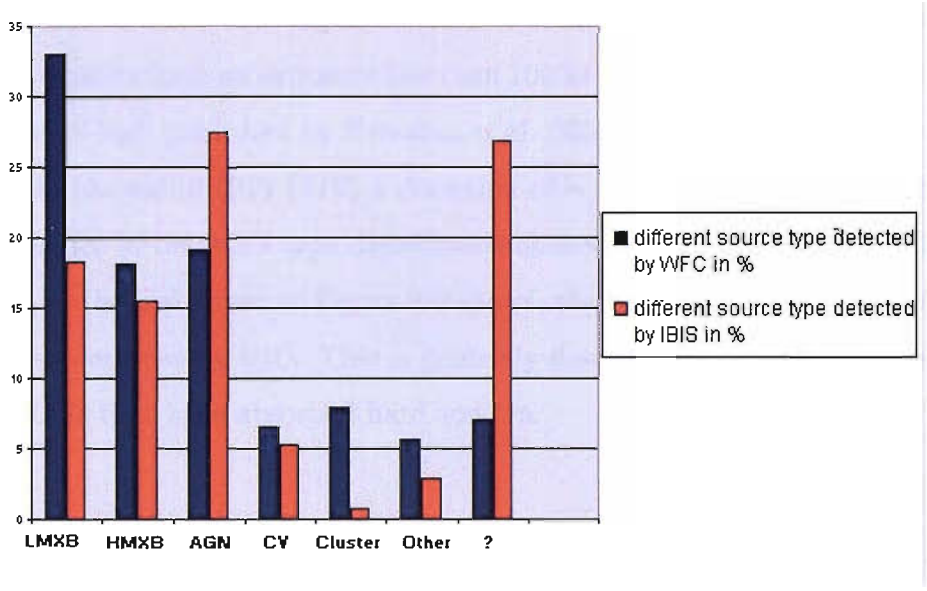

Figure 8.7: Percentage of different source types detected in WFC and IBIS/ISGRI catalogues. The question mark indicates the unidentified sources.

by WFCs or by either IBIS and WFCs whit respect to the total of WFCs sources. Although the exposure distribution is similar in both instruments (both of them have a considerable higher exposure around the galactic centre zone) the diagram shows some remarkable differences: most of the LMXBs are present in the mosaics of both instruments. 8% of them, detected only by WFCs, were mostly off after the *INTEGRAL* launch as can be verified from the *RXTE*/ASM light curves, except for four LMXB that have an IBIS exposure less than 1 ks (X2127+119, 1H0512–401, XTE J1118+480, 4U 1700+24).

The same situation applies for the HMXBs: the ones detected only by WFCs were mostly off after the *INTEGRAL* launch. The number of transient sources in HMXB is less than the one in LMXB, this is obviously reflected in the histogram of Figure 8.8. The typical soft spectra of clusters of galaxies is probably the reason why this class of sources is mostly detected only by WFC. Concerning AGN, detected in the WFCs mosaics, about 40% of them have not been observed by IBIS, and this is

principally due to a low IBIS exposure. In fact of 66% of the AGN detected only in the WFCs mosaics have an exposure less than 100 ks in IBIS (we extrapolated, from the AGN logN-logS published by Krivonos et al. 2007, that for an IBIS observation of 100 ks, in the entire IBIS FOV, a detection of $\sim$ 1 AGN is expected). There is also a difference in the AGN type distribution observed between IBIS and WFC. In particular, as the histogram in Figure 8.9 shows, the Seyfert 2 galaxies detected by WFC are all detected by IBIS. This is probably due to the spectral characteristics of these AGNs that have absorbed hard spectra.

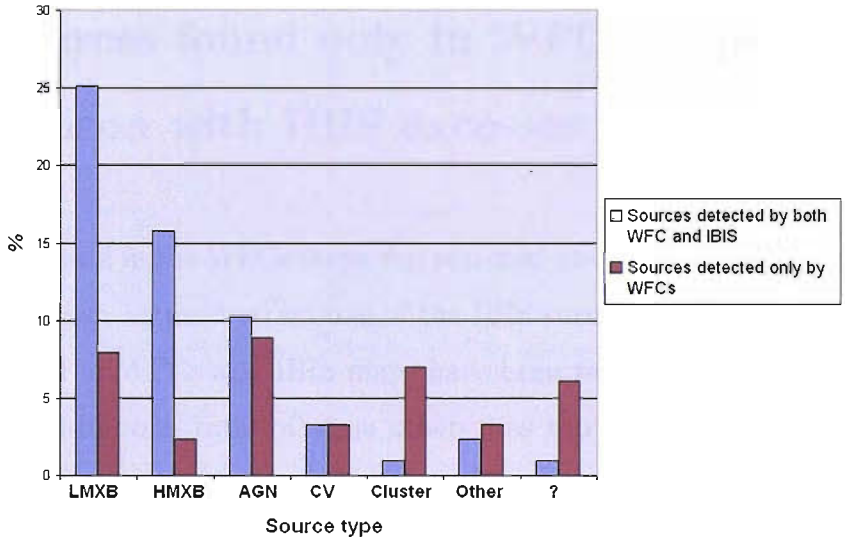

Figure 8.8: Percentage of different source types detected only by WFCs and by both WFCs and IBIS. The question mark indicates the unidentified sources.

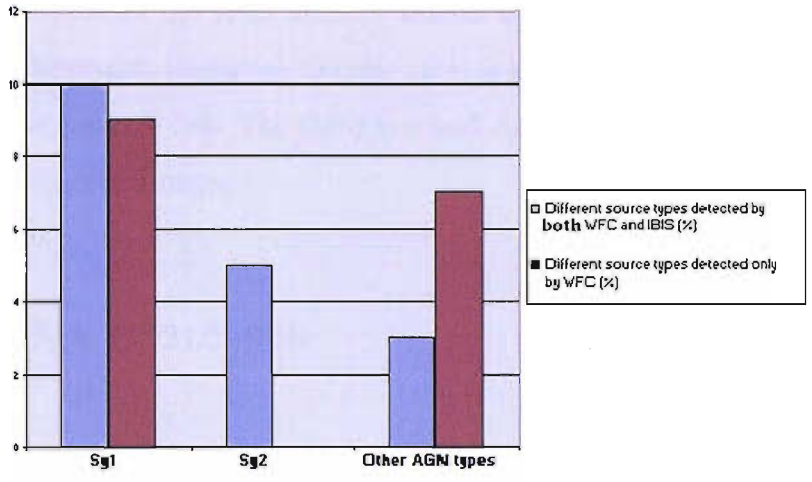

Figure 8.9: Percentage of different AGN types detected only by WFCs and by both WFCs and IBIS.

8.5 Sources found only in WFCs maps and comparison with IBIS excesses

Each excess found in the WFCs maps was searched also in the IBIS maps in order to better distinguish between structures of the IBIS survey mosaics and sources. The excesses found in WFCs and IBIS maps have been recognized, mostly, as sources, but the signal-to-noise ratio of some others was too low, in the mosaics of both instruments, to be considered as a source. There are some cases that have been considered as ambiguous because the excesses in the WFCs maps were bright enough to be a source, but in IBIS maps the excesses at the same coordinates have a signal-to-noise ratio value too near the threshold significance.

We analysed in detail three of these cases that we believed as the most relevant to describe the use of this "comparison techniques". Of these three cases described in the next subsections, the first is a positive case: the source was detected in the IBIS mosaics thanks to WFCs detection. The second was an ambiguous case: the

source was detected in the IBIS mosaics thanks to WFCs detection, but even if it is probably a detection, its signal-to-noise ratio is too low to allow the source in the final IBIS survey source list. The third is a bad case: the source detected is clearly a structure of the IBIS maps.

8.5.1 EXMS B1210–645

In this case the source was detected by IBIS around 5 sigma, but the automated source search procedures failed to find it. Then this source has been classified as an *INTEGRAL* detection thanks to the WFCs detection. Figures 8.10 and Figures 8.11 shows IBIS and WFCs zoom of the maps centered around this source coordinates.

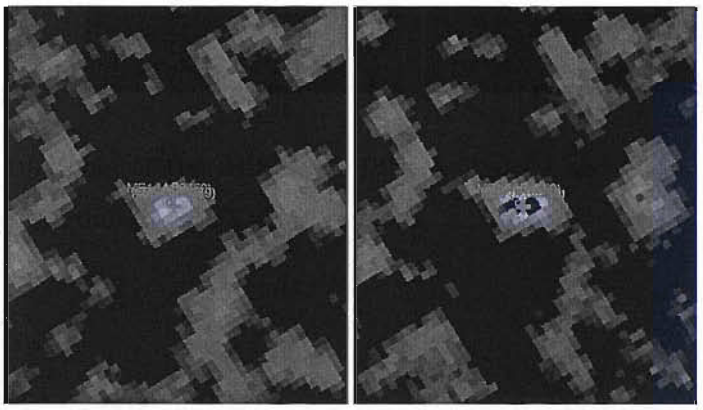

Figure 8.10: Zoom of the IBIS maps 18-60 keV (left) and 20-100 keV (right) centered around the coordinates of EXMS B1210–645.

8.5.2 3A 0726–260

This source was detected by IBIS at a significance of about $\sim 4\sigma$, i.e. below the limit of acceptance in a noisy region of the maps, so it was considered as a dubious source

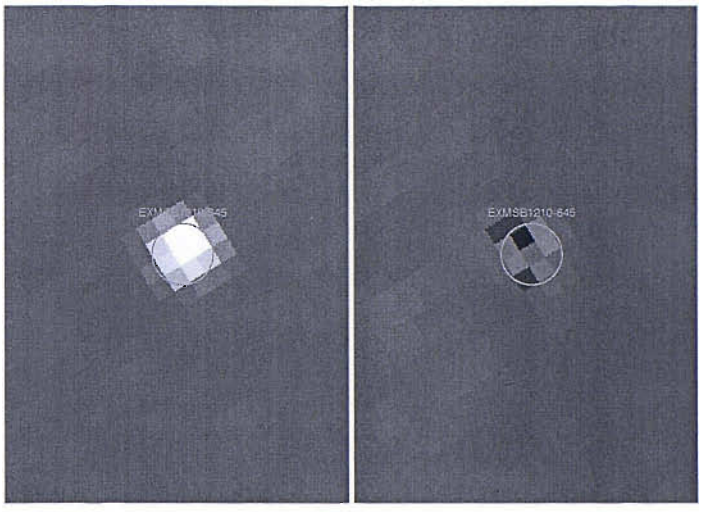

Figure 8.11: Zoom of the WFCs maps 3-17 keV (left) and 17-28 keV (right) centered around the coordinates of EXMS B1210–645.

even if it was clearly detected in the WFCs mosaics. Figures 8.12 and Figures 8.13 shows IBIS and WFCs zoom of the maps centered around this source coordinates.

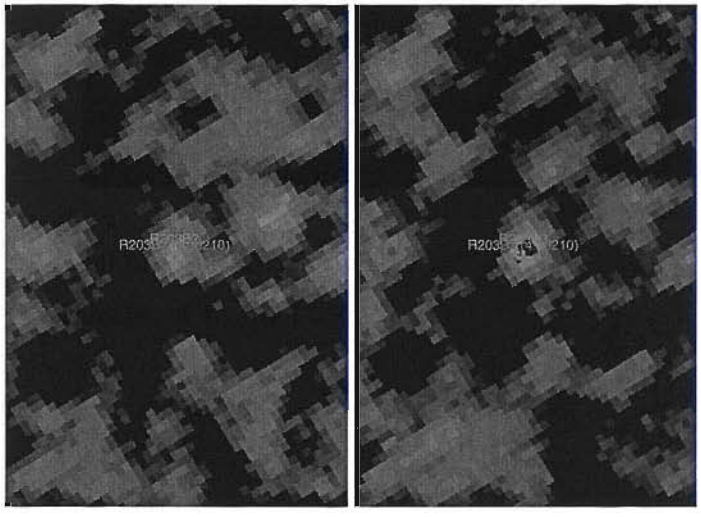

Figure 8.12: Zoom of the IBIS maps 18-60 keV (left) and 20-100 keV (right) centered around the coordinates of 3A 0726–260.

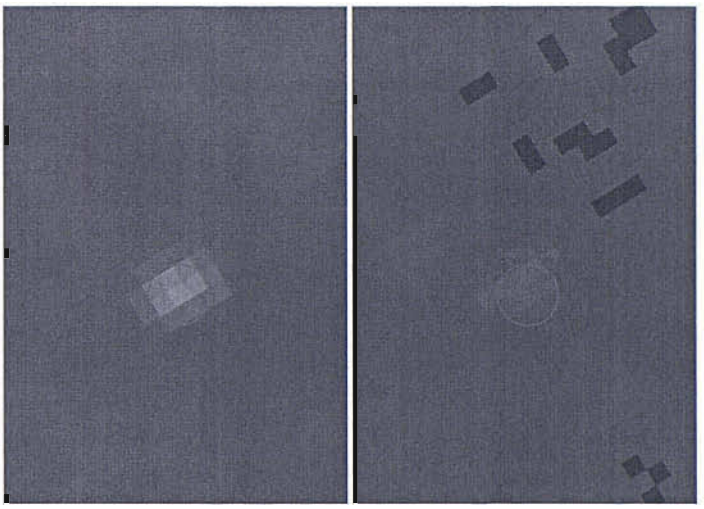

Figure 8.13: Zoom of the WFCs maps 3-17 keV (left) and 17-28 keV (right) centered around the coordinates of 3A 0726–260.

8.5.3 QSO B1821+643

This case was analysed in detail, but at the end, even if the source was clearly detected by WFCs, it was not accepted in the IBIS catalogue because in the IBIS mosaic maps, it is too close to a structure of the image and its PSF is very bad as Figures 8.14 and Figures 8.15 show. Could also be noted that the source is strongly visible in the low energy *BeppoSAX* map, so the excess in the 20-100 IBIS map might be a false correlation.

8.6 Light curves from SAX/WFC data

The single OP images that are basis for the mosaics, have been used also for light curve extractions: for each image, the fluxes taken at the position of the source, have been plotted, with their error, vs. time. The bin of the curves varies with the duration of the single OP observation and it is always less than 100 ks. The

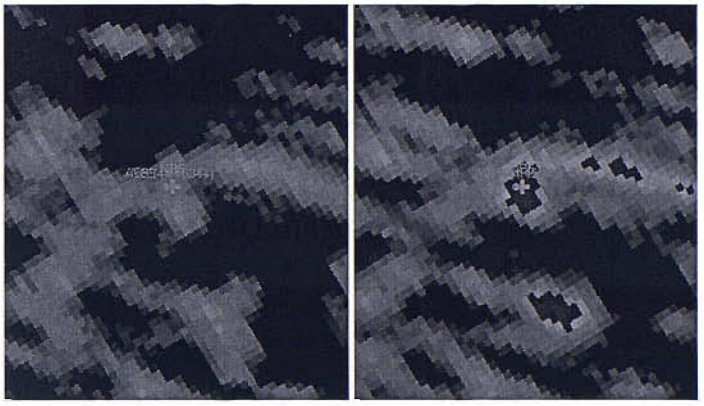

Figure 8.14: Zoom of the IBIS maps 18-60 keV (left) and 20-100 keV (right) centered around the coordinates of QSO B1821+64.

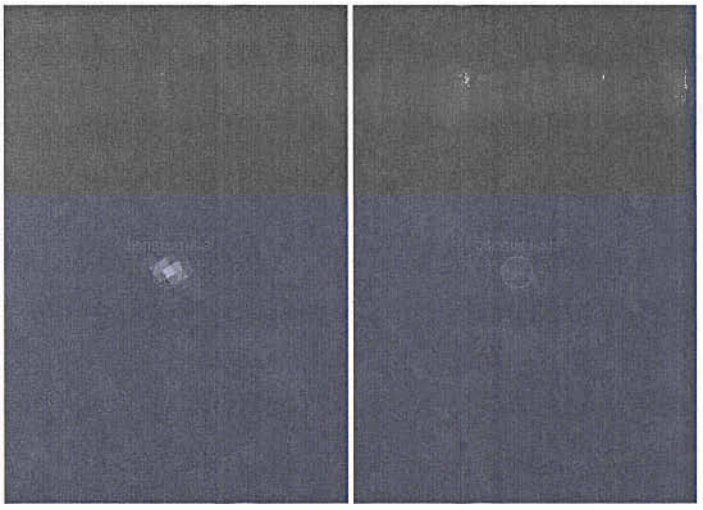

Figure 8.15: Zoom of the WFCs maps 3-17 keV (left) and 17-28 keV (right) centered around the coordinates of QSOB1821+64.

light curves have been extracted for either energy ranges of the images: 3-17 keV and 17-28 keV. A filter on the position of the source whit respect to the centre of the observation has been applied to each image, in order to minimize the different instrument response to the off-axis sources that is not completely corrected by WFC standard analysis. After a study on the off-axis flux from the Crab, only detections between 3° and 13° have been chosen.

8.6.1 Investigation of possible sources

In the WFC mosaics 18 possible new sources have been detected and light curves in two different energy ranges have been produced for these possible detections using as bin time a single OP. Most of the possible new sources have been discarded after a visual selection of the mosaics and light curves, and only two of them were added to the list of sources reported in Table 8.2. For these two sources the light curves in two energy ranges: 3-17 keV and 17-28 keV, are reported, as shown in Figure 8.16 and Figure 8.17. In the case of the source in Figure 8.16, named NEW-399, the light curves do not present any strong evidence that this source was active, so it is, probably, a faint persistent source whose signal became detectable only by adding all the observations. On the contrary the light curves of the other source, NEW-8046, (see Figure 8.17) shows that, at least, it was detectable around MJD~51850 in the hard energy range and MJD~51500 in the soft one.

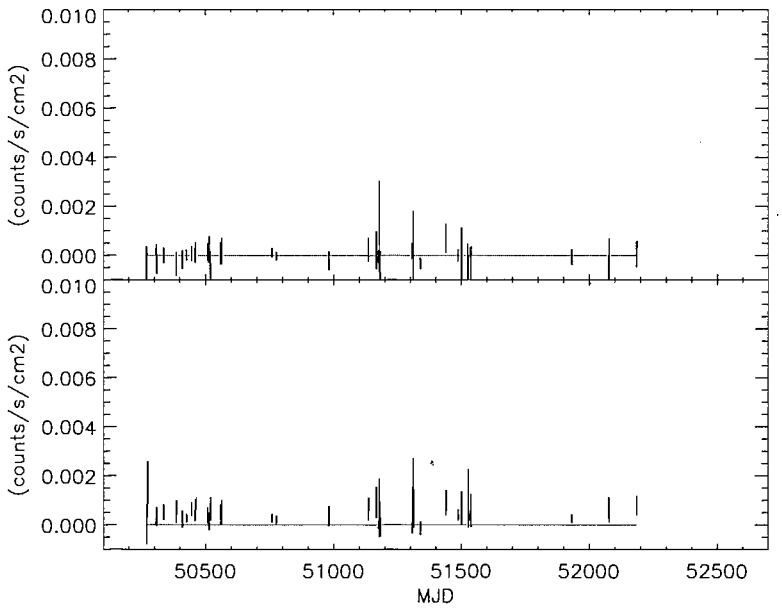

Figure 8.16: Light curves of one of the possible new sources (NEW-339, see Table 8.2) in two energy ranges 3-17 keV (top) and 17-28 keV (bottom). The zero flux line is represented in red.

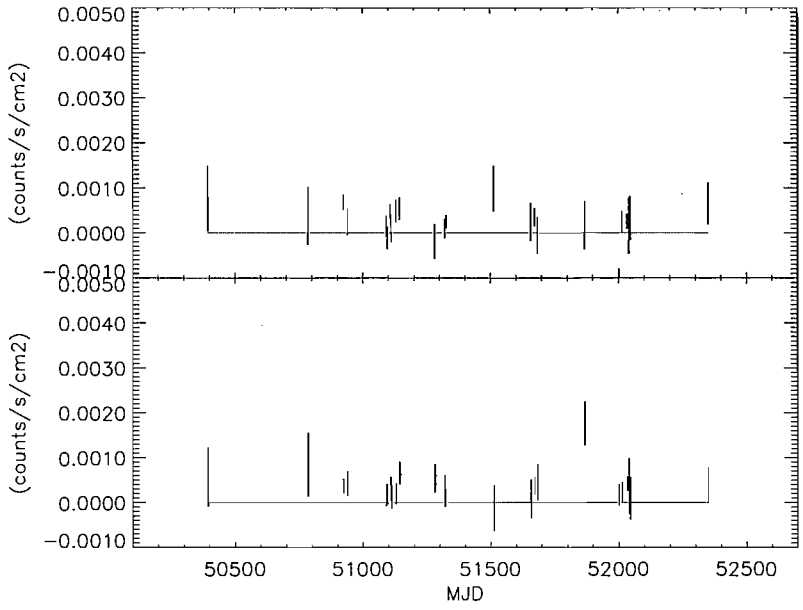

Figure 8.17: Light curves of one of the possible new sources (NEW-8046, see Table 8.2) in two energy ranges 3-17 keV (top) and 17-28 keV (bottom). The zero flux line is represented in red.

8.6.2 Temporal studies of BHC

The WFC list of sources also reports seven IGR sources and three *Swift* sources, all of them are very faint but clearly detectable in the mosaic maps. We reported here, as an example, the WFC light curves, binned to one OP, of two transient LMXBs that are subject of this thesis: IGR J17091–3624 and 4U1630–47. The first source is not present in the total mosaics because of its short and faint outbursts, while it was detected twice in the WFC data (1996 and 2001) as In 't Zand reported in 2003 (In 't Zand et al. 2003) and 2004 (In 't Zand 2004). Figure 8.18 shows the light curves in two energy ranges (3-17 keV and 17-28 keV) of this source, the green horizontal lines represent the periods in which In 't Zand reported the detections. We can confirm only the 2001 outburst as shown by the light curves (MJD$\sim$ 52100 – 52200). In Figure 8.19 we also report the 3-17 keV mosaic of the WFC observation

images taken in the period of the 2001 outburst. In this case the source is detected at a level of $\sim 15\sigma$. Concerning the 1996 outburst we found in the partial mosaic images a detection only at $\sim 4.5\sigma$ that is not enough to claim the presence of the source, because it is in a very crowded region near the galactic centre. Anyway, In 't Zand WFC archive research covers the entire data set, while our sample of WFC data covers only 60% of the total amount of data. As in the case of IGR J17091–3624 many other sources can be searched in the WFC data thanks to the light curves.

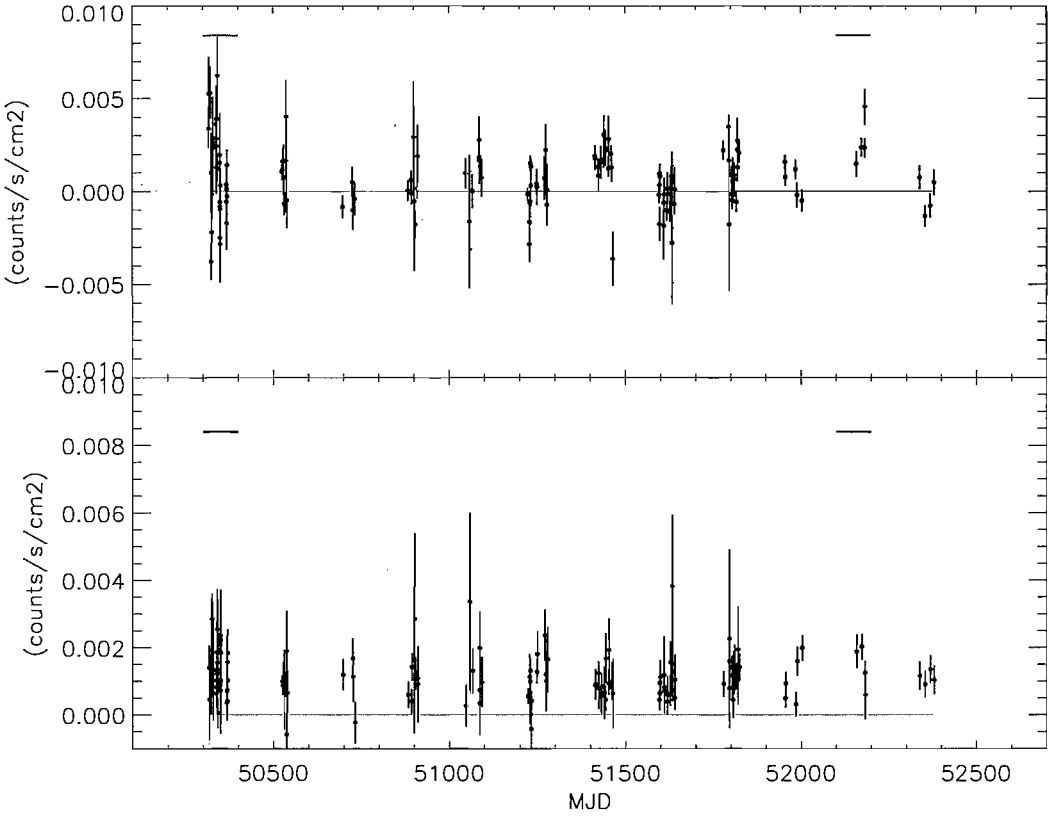

Figure 8.18: WFC light curves of the BHC IGR J17091–3624 in two energy ranges 3-17 keV (top) and 17-28 keV (bottom). The green lines sign the periods of the detections reported by In 't Zand et al. (2004). The zero flux line is represented in red.

Another example, briefly shown here, is 4U1630–47. This source is a bright

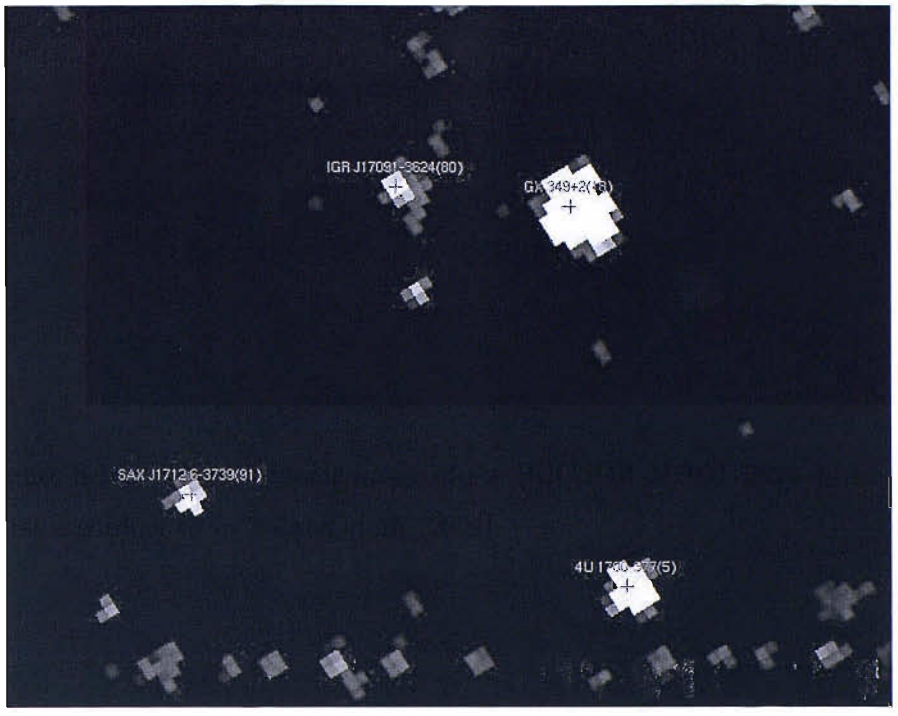

Figure 8.19: 3-17 keV mosaic image of the BHC IGR J17091–3624 during the 2001 outburst according to In 't Zand et al. (2004).

transient BHC detected in both IBIS and WFC maps. Figure 8.20 shows its 3-17 keV and 17-28 keV light curves and the hardness ratio defined as: HR=$(F_{17-28}-F_{3-17})/(F_{17-28}+F_{3-17})$. The source went into outburst several times during the *BeppoSAX* operational life. Unfortunately the WFC observational strategy did not permit to follow the entire outburst of the source and, for this reason, Figure 8.21 reports the WFC light curve between 3-17 keV together with the *RXTE*light curve between 5-12 keV in the same time interval. The hardness ratio, in Figure 8.20, shows that the source had a big soft flare at MJD $\sim$ 50900 then a hardening at MJD $\sim$ 51200 and the source was again in soft state at MJD $\sim$ 51900. Figure 8.21 shows the comparison between the 3-17 keV WFC light curves of 4U 1630–47 and the 5-12 keV *RXTE*/ASM light curves.

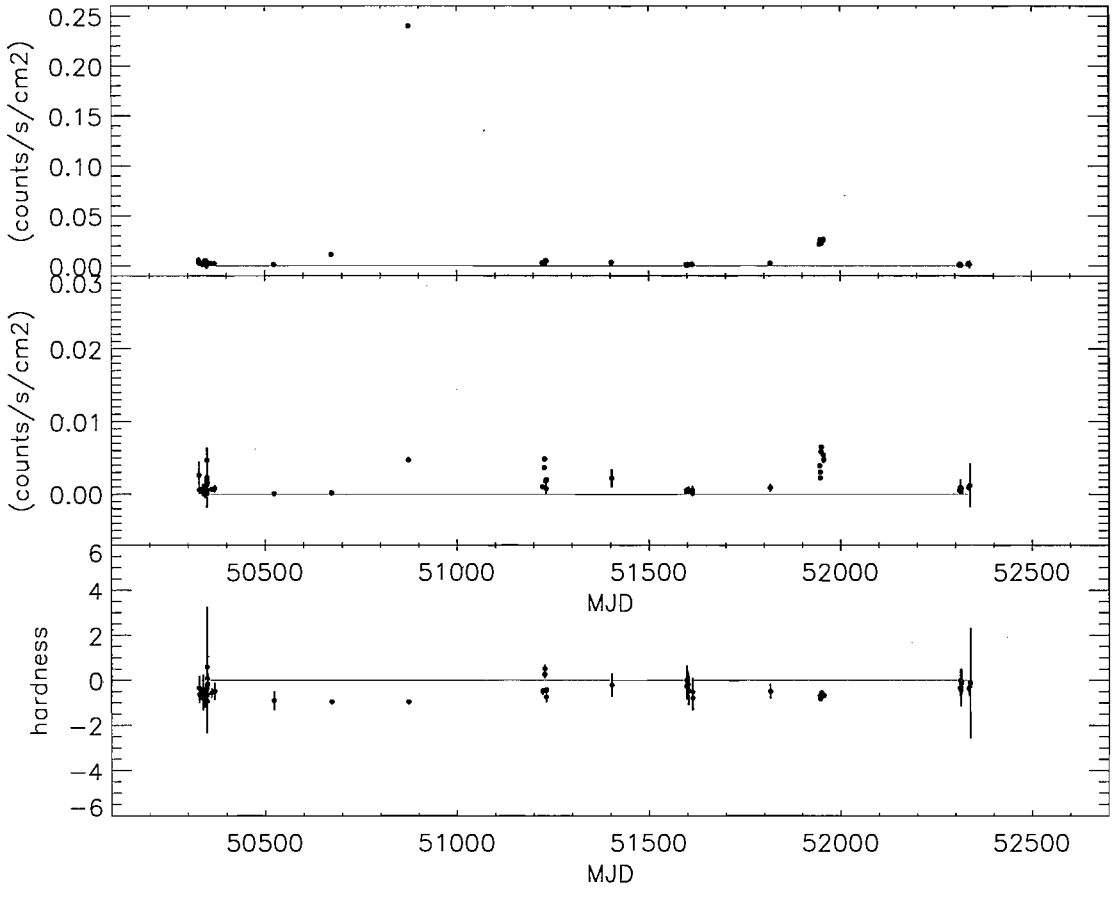

Figure 8.20: Light curves of the BHC 4U 1630–47 in two energy ranges 3-17 keV (top) and 17-28 keV (middle) and hardness ratio (bottom) (for the hardness ratio definition see text). The zero flux line is represented in red.

8.7 Concluding remarks

The WFC hardware configuration as well as the software approach were optimised for transient events (GRB, XRB, etc..). This could be a limit in the detection of very weak persistent sources. For example, the IROS approach to image deconvolution may not be optimised for later mosaicking. Nevertheless the mosaicking technique approach, developed for the IBIS survey, has been successfully applied in this work to the *BeppoSAX* WFCs. In fact, looking at the number of *Swift* and IGR sources

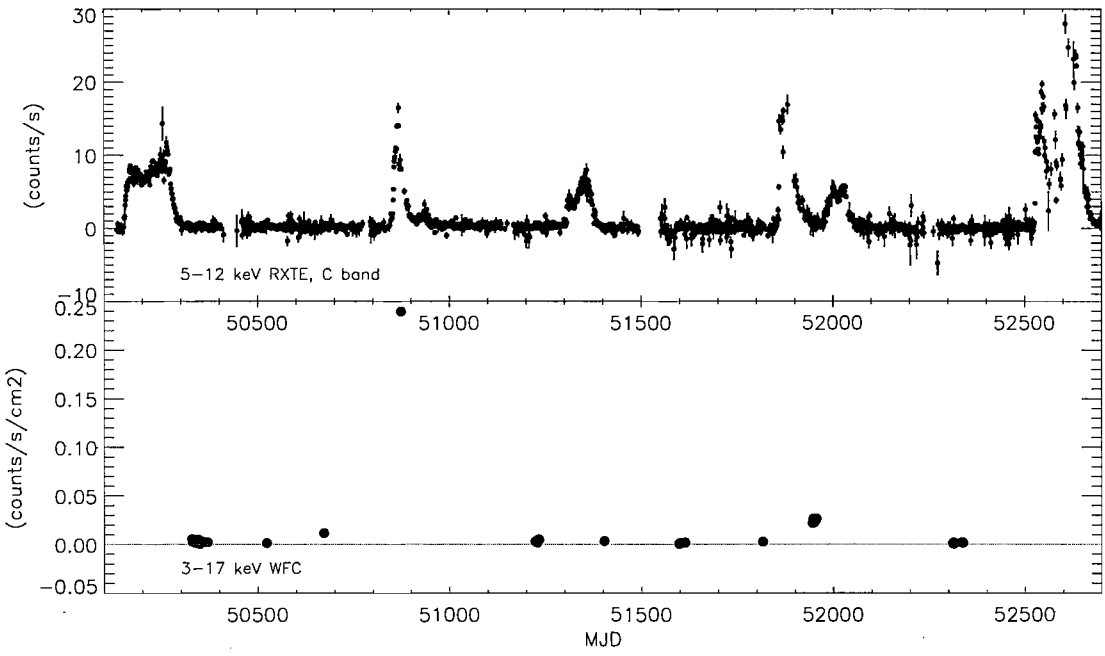

Figure 8.21: Light curves of 4U 1630–47. *Top panel RXTE*/ASM light curve (5-12 keV). *Bottom panel* WFC light curve (3-17 keV).

in the catalogue, it is clear that *SAX*/WFC data has not yet been fully exploited.

Unfortunately, it was not possible to have access to the entire WFC data set. With the complete archive more could have been done, although it also depends on the sky distribution of the missing data. In fact, if by adding these data we will get a more uniform sky exposure an improvement of the instrument sensitivity can be obtained especially for weak persistent sources as well as a 40% more chance to catch transient sources. Our approach to use the WFCs to complement the IBIS survey search for sources as been successful and for sure will certainly be used in future survey work.

The use of *SAX*, *RXTE* and IBIS data in combination offers an unique opportunity to cover long-term studies of single sources and/or classes of sources in overlapping energy bands from 1996 up to the present day.

Table 8.2: List of sources detected in WFCs mosaics. The sources in bolted have not been detected in IBIS maps. While the others have been detected in both instruments.

Name	Ra (deg)	dec (deg)	σ (3-17 keV)	σ (17-28 keV)	exposure (Ms)	source type
4U0022+63	6.31834	64.1909	141.595	12.0653	6.98418	SNR
V709Cas	7.20112	59.3030	25.8317	11.8183	5.99200	CV
1ES0033+59.5	8.96777	59.8473	33.1727	12.5262	6.37353	BLLAC
gamCas	14.1568	60.7161	124.234	42.1654	6.63829	HMXRB
XTEJ0111-7317	17.8498	-73.2878	70.0494	53.7418	10.6033	HMXRB
3A0114+650	19.5026	65.2868	61.4733	48.8518	6.53011	HMXRB
H0115+634	19.6205	63.7432	23.8867	18.4550	6.89315	HMXRB
SMCX-1	19.2862	-73.4450	420.960	230.769	10.5937	HMXRB
NGC526A	20.9763	-35.0672	11.8154	6.20370	2.52075	Cluster
4U0142+614	26.5929	61.7514	66.6555	3.38937	5.51083	AXP
RXJ0146.9+6121	26.7652	61.3469	53.0691	20.0326	5.54233	HMXRB
QSOB0241+62	41.2920	62.4818	20.5786	9.18191	5.70256	Sy1
4U0253+4	43.6542	41.5927	11.4513	3.34281	2.29718	Cluster
Algol	47.0433	40.9674	41.6329	2.59059	2.04728	Star
RXJ0317.9-4414	49.4688	-44.2333	11.7856	1.83838	4.08155	Cluster
NGC1275	49.9676	41.4995	199.457	32.6663	2.92814	Sy2
H0324+28	51.6275	28.6933	10.7020	1.00029	1.75583	CV
PLX-728	52.7700	43.9300	25.0596	14.3471	3.54941	CV
4U-0336+01	54.1994	0.587916	12.5986	2.07105	1.91496	CV
IGRJ03532-6829	58.2334	-68.5110	9.96127	1.64294	8.77392	BLLAC
XPer	58.8335	31.0497	89.9894	23.5753	1.80897	HMXRB
ABELL0748	63.3602	10.4667	11.7130	0.827295	2.22631	Cluster
ABELL3266	67.8301	-61.4262	10.7359	3.20928	7.61464	Cluster

Continued on Next Page...

Table 8.2 – Continued

Name	Ra (deg)	dec (deg)	σ (3-17 keV)	σ (17-28 keV)	exposure (Ms)	source type
3C120	68.2803	5.37344	11.1832	6.36176	2.18872	Sy1
LEDA168563	73.0293	49.5115	18.4753	8.38947	2.98416	Sy1
QSOB0502+675	76.9286	67.6173	19.0632	6.84063	7.27812	BLLAC
1H0512-401	78.5332	-40.0177	85.3516	25.8686	4.82603	LMXRB
1H0521-720	80.0519	-71.9495	600.290	107.854	12.4641	LMXRB
XSSJ05295-3252	82.3424	-32.8098	17.4836	7.59946	4.45087	CV
OrionComplex	83.7989	-5.37032	13.3781	5.24350	2.42135	OrionComplex
Crab	83.6293	22.0217	15830.5	4915.32	5.11987	Pulsar
LMCX-4	83.2055	-66.3673	95.9477	87.1328	7.92747	HMXRB
XLMCX-3	84.7316	-64.0846	495.256	25.0758	7.95744	HMXRB
LMCX-1	84.8960	-69.7420	517.889	25.8886	9.01888	HMXRB
BYCam	85.6978	60.8592	15.9777	7.79669	4.80522	CV
PSRB0540-69.3	85.0605	-69.2930	24.0871	7.78895	9.10927	XRB
MCG+08-11-011	88.7186	46.4279	24.5657	3.94754	6.02541	Sy1
EXO055620-3820.2	89.4940	-38.3168	7.19049	5.59198	5.18837	Sy1
1RXSJ061133.8-814917	92.9560	-81.8205	12.1297	5.41515	12.5971	nova
H0614+091	94.2826	9.13618	456.075	100.207	5.04196	LMXRB
3A0726-260	112.210	-26.1003	15.2614	8.02427	3.56390	HMXRB
4U0739-19	116.875	-19.3007	19.4958	2.06844	3.17065	Cluster
EXO0748-676	117.127	-67.7554	155.636	79.6226	11.0951	LMXRB
RXJ0812.4-3114	123.140	-31.2450	29.0387	15.1238	3.73574	HMXRB
1ES-0821-42.6	125.881	-42.8001	11.2462	2.27680	5.64721	SNR
NEW1-8046	126.300	73.1062	11.6074	3.77594	9.90238	Nosour
VelaPulsar	128.833	-45.1815	43.1107	17.3738	5.48134	Pulsar
QSOB0836+710	130.292	70.8969	26.4021	9.59867	9.64929	Blazar
VelaX-1	135.523	-40.5548	877.565	924.723	4.93001	HMXRB

Continued on Next Page...

Table 8.2 – Continued

Name	Ra (deg)	dec (deg)	σ (3-17 keV)	σ (17-28 keV)	exposure (Ms)	source type
SWIFTJ0917.2-6221	139.017	-62.3116	7.83899	3.03746	9.14126	Sy2
3A0921-630	140.706	-63.3028	38.4590	10.9299	9.35116	LMXRB
H0918-549	140.048	-55.1540	118.818	25.8325	6.57944	u
H0918-549	140.087	-55.1941	161.285	35.4680	6.44543	u
X0922-314	141.084	-31.6996	65.5295	11.0679	3.18614	u
MCG-05-23-016	146.909	-30.9328	29.2727	6.95066	2.73789	Sy2
M82	148.969	69.6707	17.5900	3.03702	8.95492	IGal
GROJ1008-57	152.438	-58.2961	12.9035	6.34903	7.43901	HMXRB
4U1036-56	159.454	-56.7584	16.9869	11.6190	7.24201	HMXRB
IGRJ10448-5945	161.251	-59.6999	52.6322	18.4115	7.77746	Star
Mrk421	166.151	38.2213	118.112	20.9139	2.72517	BLLAC
NGC3516	166.706	72.5821	27.3634	11.7216	9.92385	Sy1
XTEJ1118+480	169.580	48.0643	22.7135	5.68825	3.50217	LMXRB
CenX-3	170.307	-60.6266	828.544	573.210	7.32961	HMXRB
1H1121-591	171.140	-59.2594	17.3593	1.69421	7.11668	SNR
HR4492	174.872	-65.3930	59.8694	14.4377	7.62520	CV
NGC3783	174.730	-37.7532	15.6341	6.61433	3.13688	Sy1
SWIFTJ1142.7+7149	175.901	71.7022	13.2332	4.83423	10.0845	CV
IGRJ11435-6109	175.865	-61.1492	6.15299	1.29952	7.15088	HMXRB
1E1145.1-6141	176.865	-61.9636	132.823	101.060	7.18261	HMXRB
RXJ1145.2+7940	176.417	79.6881	11.1607	5.87884	9.90519	Sy1
H1145-619	177.016	-62.1990	23.4359	8.26284	7.01419	HMXRB
NGC4151	182.642	39.4111	76.5256	46.4709	3.21361	Sy1
EXMSB1210-645	183.284	-64.8853	50.3104	19.1657	7.41370	u
GX301-2	186.650	-62.7729	389.448	716.619	6.13120	HMXRB
3C273	187.279	2.04792	18.6343	7.89661	0.701545	QSO

Continued on Next Page...

Table 8.2 – Continued

Name	Ra (deg)	dec (deg)	σ (3-17 keV)	σ (17-28 keV)	exposure (Ms)	source type
IGRJ12349-6434	188.733	-64.5696	11.2296	13.1787	6.86560	Symb
1H1249-637	190.721	-63.0693	15.1452	6.73650	6.51476	HMXRB
3A1246-588	192.402	-59.0913	104.706	26.7911	5.93159	HMXRB
Abell3526	192.215	-41.2909	16.2513	3.14853	2.20531	Cluster
1H1251-291	193.122	-29.2559	26.5511	6.30936	1.78437	CV
1H1254-690	194.426	-69.2992	729.968	160.428	9.14823	LMXRB
comaCG	194.954	27.9613	19.3721	4.67689	1.63311	Cluster
4U1323-62	201.637	-62.1381	88.7906	40.9302	6.24667	LMXRB
CenA	201.365	-43.0199	138.655	75.1729	2.29013	Sy2
MCG-06-30-015	203.995	-34.3025	14.2180	6.80631	2.13042	Sy1
s1344-326	206.888	-32.8377	15.0844	3.26629	1.95469	Cluster
Abell1795	207.219	26.5817	14.0303	4.28744	1.77656	Cluster
IC4329A	207.334	-30.3108	31.8060	11.5270	1.95751	Sy1
Mrk279	208.264	69.3208	15.6263	2.23140	7.99785	Sy1
1H1348-633	209.495	-64.7329	35.5244	14.5440	7.05233	LMXRB
NGC5506	213.320	-3.21624	36.3907	17.7082	1.34728	Sy1
NGC5548	214.515	25.1250	13.4111	3.40731	1.71155	Sy1
H1417-624	215.302	-62.7062	23.2232	16.5656	5.63348	HMXRB
SAXJ1428.6-5422	217.150	-54.4053	39.6561	17.9725	4.02825	u
Abell202	227.755	5.74061	11.5135	2.02290	1.42461	Cluster
CirX-1	230.171	-57.1690	7950.28	1249.11	4.49952	LMXRB
RXCJ1539.5-8335	234.934	-83.5853	16.3168	0.720054	12.2913	u
H1538-522	235.597	-52.3880	95.4956	75.9046	3.97820	HMXRB
XTEJ1543-568	235.973	-56.7330	19.8686	19.6769	4.03635	HMXRB
4U1543-624	236.966	-62.5646	333.134	71.8923	5.19487	LMXRB
XTEJ1550-564	237.749	-56.4772	1088.61	93.8491	4.12376	LMXRB

Continued on Next Page...

Table 8.2 – Continued

Name	Ra (deg)	dec (deg)	σ (3-17 keV)	σ (17-28 keV)	exposure (Ms)	source type
Abell2142	239.607	27.2114	18.4396	7.96893	2.74943	Cluster
1H1556-605	240.306	-60.7606	210.035	38.5864	4.49780	LMXRB
1RXSJ160147.6-754507	240.474	-75.7593	16.7630	2.86467	12.7309	u
H1608-522	243.179	-52.4238	117.185	29.7587	3.91205	LMXRB
Abell2199	247.190	39.5497	21.9965	3.39497	4.97013	Cluster
H1624-490	247.018	-49.2119	445.533	117.941	3.18465	LMXRB
IGRJ16320-4751	248.0225	-47.8686	11.524	8.891	3.0556	u
4U1626-67	248.077	-67.4658	87.9540	58.5460	7.85885	LMXRB
4U1630-47	248.504	-47.3969	124.098	22.8206	3.07302	LMXRB
IGRJ16377-6423	249.471	-64.3817	13.3906	5.03318	5.70873	Cluster
H1636-536	250.231	-53.7527	2183.14	474.582	3.10582	LMXRB
GX340+0	251.448	-45.6132	3897.04	956.881	5.85603	LMXRB
Mrk501	253.466	39.7776	108.224	30.1326	5.35046	BLLAC
GROJ1655-40	253.522	-39.8348	1923.29	226.873	4.98225	LMXRB
HerX-1	254.461	35.3385	263.126	219.857	4.22297	LMXRB
4U1700-377	255.987	-37.8470	371.605	275.303	5.06663	HMXRB
EXSS1706.6+7842	255.992	78.6197	21.9809	10.4659	13.0383	Cluster
H1658-298	255.522	-29.9237	143.717	40.1639	3.81499	LMXRB
GX339-4	255.706	-48.7913	101.096	18.0820	2.94905	LMXRB
OAO1657-415	255.203	-41.6590	37.9979	44.6928	5.59195	HMXRB
4U1700+24	256.640	23.9588	16.4524	4.68779	2.58035	LMXRB
GX349+2	256.442	-36.4259	5262.98	1530.65	4.91381	LMXRB
H1702-429	256.559	-43.0423	327.298	95.8032	5.65664	LMXRB
H1705-440	257.223	-44.1027	927.058	236.222	5.70172	LMXRB
4U1708-40	258.099	-40.8768	151.853	28.2489	4.91099	LMXRB
SAXJ1712.6-3739	258.132	-37.6433	44.8714	11.8891	4.90433	LMXRB

Continued on Next Page...

Table 8.2 – Continued

Name	Ra (deg)	dec (deg)	σ (3-17 keV)	σ (17-28 keV)	exposure (Ms)	source type
XTEJ1716-389	258.935	-38.8690	98.6470	24.8816	4.84295	XRB
XTEJ1723-376	260.925	-37.6539	77.2228	16.7247	4.81628	LMXRB
GRS1724-308	261.890	-30.8042	299.965	125.744	4.12613	LMXRB
HD159023	262.165	59.0560	11.4298	0.489204	8.05477	Star
GX354-0	262.992	-33.8343	969.743	456.972	4.21959	LMXRB
GX9+9	262.934	-16.9617	1350.57	262.387	3.75875	LMXRB
4U1730-335	263.350	-33.3907	272.015	85.3046	4.19707	LMXRB
KS1731-260	263.535	-26.0661	783.368	260.554	3.94063	LMXRB
GX1+4	263.008	-24.7470	92.3477	131.931	3.91266	LMXRB
4U1735-444	264.742	-44.4525	1666.79	462.999	5.19142	LMXRB
SLX1735-269	264.572	-26.9922	77.6137	28.9677	4.20121	LMXRB
1E1740.7-2942	265.979	-29.7473	153.171	204.420	4.09207	LMXRB
XTEJ1739-278	265.687	-27.7494	110.578	6.66180	4.20507	LMXRB
1A1742-294?	266.476	-29.4906	270.484	157.300	4.11444	LMXRB
1E1743.1-2843	266.590	-28.6700	28.3316	26.9350	4.13322	LMXRB
GROJ1744-28	266.156	-28.7559	197.580	201.348	4.06334	LMXRB
GX3+1	266.982	-26.5624	3530.57	917.979	4.19628	LMXRB
SAXJ1747.0-2853	266.723	-28.8800	109.746	41.1885	4.19356	LMXRB
SLX1744-299	266.860	-30.0186	214.437	94.8626	4.25188	LMXRB
1H1746-370	267.550	-37.0446	407.462	142.282	4.63498	LMXRB
EXO1745-248	267.028	-24.7810	503.262	188.385	4.00327	LMXRB
GRS1747-312	267.654	-31.2965	63.8850	25.0908	4.38486	LMXRB
GRS1758-258	270.303	-25.7449	162.109	66.2465	4.02859	LMXRB
GX5-1	270.284	-25.0814	9270.36	2228.14	4.08232	LMXRB
GX9+1	270.388	-20.5292	4716.11	1170.71	3.89689	LMXRB
4U1812-12	273.775	-12.0974	68.2598	24.3324	4.52781	LMXRB

Continued on Next Page...

Table 8.2 – Continued

Name	Ra (deg)	dec (deg)	σ (3-17 keV)	σ (17-28 keV)	exposure (Ms)	source type
GX13+1	273.629	-17.1568	2392.98	374.771	4.09819	LMXRB
1H1814+498	274.061	49.8692	91.5320	40.1706	7.72613	CV
GX17+2	274.006	-14.0364	4165.70	1028.26	4.37304	LMXRB
QSOB1821+643	275.504	64.3416	18.1009	6.37046	8.18802	Sy1
H1820-303	275.917	-30.3622	2336.14	711.125	4.23966	LMXRB
3A1822-371	276.448	-37.1081	138.489	108.781	4.79882	LMXRB
H1822-000	276.346	-0.00991021	262.052	53.8537	1.91535	LMXRB
Ginga1826-24	277.367	-23.7996	218.935	99.7134	4.11005	LMXRB
3C382	278.794	32.6970	16.7407	5.34370	4.97860	Sy1
ESO103-G35	279.528	-65.4224	11.0073	10.8918	6.01987	Sy2
SerX-1	279.991	5.03692	2591.58	587.804	1.93523	LMXRB
3C390.3	280.554	79.7677	25.6861	10.8779	12.9423	Sy1
Ginga1843+009	281.403	0.870738	40.1581	50.9282	2.02709	HMXRB
3A1845-024	282.043	-2.46100	15.4029	18.4010	1.84845	HMXRB
3A1850-087	283.261	-8.70451	20.9314	7.33278	1.74095	LMXRB
XTEJ1855-026	283.877	-2.60739	7.64945	11.1360	1.97818	HMXRB
XTEJ1856+053	284.169	5.32109	26.3459	2.41578	2.20399	LMXRB
XTEJ1859+226	284.689	22.6703	132.131	9.01740	3.37324	LMXRB
4U1909+07	287.700	7.59662	29.1343	24.3972	2.03242	HMXRB
AqlX-1	287.817	0.588655	215.222	40.5819	2.16631	LMXRB
H1907+097	287.410	9.82998	48.9697	38.6753	2.26866	HMXRB
SS433	287.957	4.98426	27.0627	10.5066	2.23460	HMXRB
GRS1915+105	288.799	10.9439	6079.38	1530.40	2.39402	LMXRB
4U1916-053	289.702	-5.23652	101.793	32.7944	2.04551	LMXRB
4U1919+44	290.292	43.9603	24.3482	8.20544	7.01764	Cluster
ESO141-55	290.339	-58.6803	10.1511	4.97704	3.99528	Sy1

Continued on Next Page...

Table 8.2 – Continued

Name	Ra (deg)	dec (deg)	σ (3-17 keV)	σ (17-28 keV)	exposure (Ms)	source type
XTEJ1946+274	296.427	27.3650	86.9013	69.3140	3.43271	XRB
KS1947+300	297.400	30.2071	53.7895	35.7596	3.85861	HMXRB
3A1954+319	298.927	32.1013	117.906	86.6901	3.78569	LMXRB
4U1957+115	299.850	11.7023	293.302	23.5170	2.47388	LMXRB
CygA	299.880	40.7424	18.5783	8.19674	5.58442	Sy2
CygX-1	299.590	35.1983	4808.46	1663.34	4.96619	HMXRB
QSOB1959+650	300.046	65.1590	40.1296	7.55333	10.8880	Blazar
QSOB2005-489	302.306	-48.8583	54.9039	15.5552	2.59489	BLLAC
XTEJ2012+381	303.177	38.1831	11.0164	2.09689	4.72181	LMXRB
CygX-3	308.108	40.9561	2701.90	836.951	5.18115	HMXRB
EXO2030+375	308.058	37.6384	25.1847	14.9854	4.36609	HMXRB
4C74.26	310.698	75.1461	22.8232	11.1206	13.7501	QSO
Mrk509	311.060	-10.7330	16.1028	4.61255	1.76827	Sy1
1XRSJ205644.3+494011	314.167	49.6801	15.1359	5.42620	6.20829	u
[*WWF*2005]2	314.676	41.7609	11.8311	7.75949	5.24211	u
SAXJ2103.5+4545	315.894	45.7494	45.3801	27.8099	5.22746	HMXRB
SS52116+81	318.830	82.0506	15.3843	8.77117	12.8110	Sy1
IGRJ21247+5058	321.162	50.9713	19.3449	9.12722	6.12249	Sy1
SWIFTJ2127.4+5654	321.866	56.9181	6.13192	1.94945	7.31209	Sy1
X2127+119	322.512	12.1763	150.042	26.3435	1.15991	LMXRB
SSCyg	325.691	43.5700	65.9035	22.7378	5.28799	CV
CygX-2	326.169	38.3194	5236.82	1091.97	4.29372	LMXRB
PKS2155-304	329.754	-30.2496	20.8741	5.67615	2.72464	BLLAC
3A2206+543	331.982	54.5099	105.803	45.5702	6.69607	HMXRB
PB-7131	334.478	-8.31703	14.6095	8.58632	1.19937	CV
Ark564	340.661	29.7520	13.2756	1.04698	2.29426	Sy1

Continued on Next Page...

Table 8.2 – Continued

Name	Ra (deg)	dec (deg)	σ (3-17 keV)	σ (17-28 keV)	exposure (Ms)	source type
H2254-033	343.814	-3.19412	20.3670	6.22706	0.874964	CV
2E2259.0+5836	345.280	58.8782	11.8295	0.719059	7.60252	AXP
NGC7469	345.791	8.87446	10.8277	5.20997	1.43838	Sy1
NEW-339	350.872	57.7382	16.5449	2.16935	6.50998	New source ?
CasA	350.857	58.8155	993.744	88.1288	7.13330	SNR

Continued on Next Page...

Chapter 9

Conclusions

The work presented in this thesis is based on results and techniques of the first and second IBIS survey catalogues and could be ideally divided in two parts. The first part, dedicated to the data analysis, is focused on two BHCs that have similar spectral and temporal characteristics. Both of them were originally detected as new *INTEGRAL* sources and then associated with known sources detected in previous missions. One of these two sources is H1743–322, a bright BHC, previously observed only in 1977 by *HEAO1* and localised with two possible positions. Thanks to the *INTEGRAL* capability the ambiguity was solved, after 25 years, and the position was definitely fixed. The other one, IGR J17091–3624, after the *INTEGRAL* detection, was also found in the data archive of *BeppoSAX* satellite.

INTEGRAL data analysis of H1743–322 covers the entire source evolution during the different phases of its 2003 and 2004 outbursts: from the increase of the blackbody emission together with the softening of the hard part of the spectrum, to the following return to the hard state. A hysteresis-like behaviour of the state transitions has been demonstrated in both observed outbursts, as predicted for transient BH by Fender, Belloni & Gallo 2004. The analysis also provides one of the first examples of a joint spectrum of the three high-energy instruments on board

INTEGRAL , IBIS, JEM-X and SPI. The wide *INTEGRAL* energy coverage also permitted the observation of a hard tail in the soft state that has been detected up to 250 keV without any cutoff. The mass function of H1746–322 is unknown, because its optical counterpart has not been identified yet. Nevertheless *INTEGRAL* and radio results, merged, give value to the hypothesis that H1743–322 could really be a BH.

IGR J17091–3624, even if faint, was monitored by *INTEGRAL* throughout the entire outburst. A blackbody emission from the disc has been, for the first time, detected by JEM-X when the source was in the soft state and a simultaneous *RXTE/INTEGRAL* spectrum has been produced during the hard state. Moreover, an intriguing similarity of the spectral and temporal evolution of the outburst is found between IGR J17091–3624 and H1743–322. A speculation on the possibility that this source could be a LMXB in the galactic centre region is also presented. A very recent study on the optical counterpart of this source suggests that it could be effectively a LMXB but at a distance much closer to us than the galactic centre. The data analysis work, presented in this thesis, shows how IBIS, thanks to its high energy coverage, is able to detect BHC state transitions. This is clear for H1743–322 and IGR J17091–3624 but also for the other faint transient BHCs detected in the second survey catalogue for which the light curves are reported in Chapter 5.

In the second part of the thesis, the survey mosaicking technique approach has been successfully applied to the *BeppoSAX* Wide Field Cameras: a catalogue of Wide Field Cameras sources extracted from the mosaics, reported at the end of Chapter 5, shows sources that have not been previously detected in WFCs. In fact most of these sources have been discovered in the last years by *INTEGRAL* or even *Swift*. Moreover two possible completely new detections have been fixed. This Chapter also shows the capability of this method to extract light curves from the images, reporting as an example the light curves of two of the BHCs analysed in

the first part of the thesis: IGR J17091–3624 and 4U 1630–47. The IBIS survey mosaicking techniques opens a new scenario on the detection capability of WFCs, but could also be applied, in theory, to all other coded mask instruments, like, for example, the other *INTEGRAL* instruments, JEM-X and SPI or even the BAT telescope on board *Swift* satellite.

IBIS and WFCs are both coded mask instruments, they have a wide field of view and an observational strategy that favours the galactic centre zone. They have a complementary energy range, partially overlapped, and a good capability to detect transient sources, but unfortunately they have not operated in the same period of time. Even if most of the high energy emission is strictly time dependent, a comparison study of high energy sources with IBIS and WFC telescopes could be very useful in terms of long time period studies and also averaged spectra and hardness ratios.

Bibliography

(Abramowicz et al. 1995) Abramowicz, M., A., Chen, X., Kato S., et al. 1995, ApJ, 438, L37.

(Barlow et al. 2005) Barlow, E. J., Bird, A. J., Clark, D. J., 2005, A&A, 437 L27.

(Belloni 2006) Belloni, T., 2006, AdSPR, 38, 2801.

(Bertin & Arnouts 1996) Bertin, E., & Arnouts, S., 1996, 117, 393.

(Bird et al. 2004) Bird, A. J., Barlow, E. J., Bassani, L., et al. 2004, ApJ, 607, L33.

(Bird et al. 2006) Bird, A. J., Barlow, E. J., Bassani, L., Bazzano, A., Blanger, G., Bodaghee, A., Capitanio, F. et al., 2006, ApJ, 636, 765.

(Bird et al. 2007) A. J. Bird, A. Malizia, A. Bazzano, E. J. Barlow, L. Bassani, A. B. Hill, G. Belanger, F. Capitanio, F. et al., 2007 accepted for publication in ApJ Sup. Ser.

(Boella et al. 1997a) Boella, G., Butler R.C., Perola, C. et al., 1997, A&AS, 122, 299.

(Boella et al. 1997b) Boella, G., Chiappetti, L., Conti, G. 1997, A&AS, 122, 327.

(Cadolle Bel et al. 2004) Cadolle Bel, M., Rodriguez, J., Sizun, P. et al. 2004, A&A 426 659.

(Capitanio et al. 2006a) Capitanio, F., Bazzano, A., Ubertini, P., Bird, A. J. Proceedings of the VI Microquasar Workshop: Microquasar and Beyond. September 18-22 2006, Societá del Casino, Como, Italy, in publication. For the on line version see http://pos.sissa.it.

(Capitanio et al. 2006b) Capitanio, F., Bazzano, A., Bird, A., J., Ubertini, P., Federici, M. Proceedings of the 6th INTEGRAL Workshop 2006, submited.

(Capitanio et al. 2006c) Capitanio, F., Bazzano, A., Ubertini, P., et al. 2006, ApJ, 643, 376.

(Capitanio et al. 2005a) Capitanio, F., Bazzano, A., Ubertini, P., De Cesare, G., Del Santo, M., Tarana, A., Joinet, A. 2006, Ad.Sp.R., 38, 2816.

(Capitanio et al. 2005b) Capitanio, F., Ubertini, P., Bazzano, A., et al. 2005, ApJ, 622, 503.

(Capitanio et al. 2004) Capitanio, F., Bazzano, A., Ubertini, P. et al. 2004 NuPhS, 132, 580.

(Caroli et al. 1987) Caroli, E., Stephen, J. B., Di Cocco, G., Natalucci, L., & Spizzichino, A. 1987, Sp. Sc. Rew., 45, 349.

(Corbel et al. 2005) Corbel, S., Kaaret,P., Fender R. P. et al. 2005, ApJ, 632, 504.

(Courvoisier et al. 2003) Courvoisier T.J.L., Walter, R., Beckmann, V. et al., A&A, 2003, 411, L53.

(Dean et al. 2005) Dean A.J., Bazzano, A., Hill, A. B., 2005, A&A, 433, 485.

(Di Cocco et al. 2003) Di Cocco, G., Caroli, E., Celesti, E. et al. 2003, A&A, 411, L189.

(Done et al. 2004) Done, C., Wardzinski, G. & Gierliński, M., 2004, MNRAS, 349, 393.

(Doxsey et al. 1977) Doxsey, H. Bradt, G. Fabbiano , R. et al., 1977, IAU Circ.3113.

(Esin et al. 1998) Esin, A.A., Narayan, R., Cui, W., 1998, ApJ, 505, 854.

(Esin et al. 2001) Esin, A. A., McClintock, J. E., Drake, J. et al. 2001, ApJ, 555, 483.

(Falke & Biermann 1996) Falke, H. & Biermann, P.,L, 1996, A&A, 308, 321.

(Fender Belloni & Gallo 2004) Fender, R. P., Belloni, T. M. & Gallo, E., 2004, MNRAS, 355, 1105.

(Fender et al. 1999) Fender, R., Corbel, S.,Tzioumis, T. et al., 1999, ApJ, 519, 165L.

(Fenimore et al. 1981) Fenimore, E. E., & Cannon, T. M., 1981, Appl. Opt., 20, 1858.

(Frank et al. 2002) Frank,J., King A. R., Raine, D.J., 2002 Accretion Pover in Astrophysiscs 3rd Ed., Cambridge University Press.

(Frontera et al. 1997) Frontera, F., Costa, E., Dal Fiume, D. et al., 1997, A&AS 122, 357.

(Gaalev et al. 1979) Galeev, A. A., Rosner, R., Vaiana, G. S., 1979, ApJ, 229, 318.

(Gallo et al. 2003) Gallo, E., Fender, R. P., Pooley, G. G., 2003, MNRAS, 344, 60.

(Garcia et al. 2001) Garcia, M. R., McClintock, J. E., Narayan, 2001, ApJ, 553, L47.

(George & Fabian 1991) George & Fabian, 1991, MNRAS, 249, 352.

(Giacconi 1960) Giacconi, R., 1960, JGR, 65, 773.

(Gierliński & Done 2002) Gierliński, M., & Done, C., 2002, MNRAS, 337, 1373.

(Gierliński 2003) Gierliński, M. & Done, C., 2003, JL MNRAS,342, 1083.

(Goldwurm 1995) Goldwurm, A., 1995, Exp. Astron., 6, 9.

(Goldwurm et al. 2003) Goldwurm, A., David, P., Foschini, L., et al., 2003, A&A, 411, L223.

(Grebenev et al. 2003) Grebenev, S. A., Lutovinov, A. A., Sunyaev, R. A. et al., 2003, Atel, 189.

(Grebenev et al. 2005) Grebenev, S. A., Molcov, S., V., & Sunyaev, R., 2005, ATel, 444.

(Grimm et al. 2002) Grimm, H.-J., Gilfanov, M. & Sunyaev, R., 2002, A&A, 391, 923.

(Homan et al. 2005) Homan, J., Miller, J. M., Wijnands, R. et al. 2005, ApJ, 623, 383.

(Homan et al. 2001) Homan, J., Wijnands, R., van der Klis, M., Belloni, T. , 2001, ApJS, 132, 377.

(In 't Zand et al. 2003) In 't Zand, J. J. M., Heise, J., Lowes, P., & Ubertini, P., 2003, ATel, 160.

(In 't Zand 2001) In 't Zand, J.M., 2001, ESA SP-459, 463, September 2001, Proceeding of the 4th INTEGRAL workshop.

(In 't Zand 2004) In 't Zand, J.M., Heise, J., Ubertini, P. et al., 2004, ESA SP-552, 463, Febuary 2004, Proceeding of the 5th INTEGRAL workshop.

(Kaluzienski et al. 1977) Kaluzienski, L.J., & Holt, S.S., 1977, IAU Circ.3099.

(Kretschmar et al. 2003) Kretschmar, P., Chenevez, J., Capitanio, F., et al. 2003, Atel 180.

(Krivonos et al. 2007) Krivonos, R., Revnivtsev, A., Lutovinov, A. et al. 2007, summitted to A&A astroph: 0701836.

(Kuulkers et al. 2003) Kuulkers, E., Lutovinov, A., Parmar, A., Capitanio, F., et al. 2003, ATel, 149.

(Kuulkers 2004) Kuulkers, E., 2004, Proceedings of the meeting "Interacting Binaries: Accretion, Evolution and Outcomes", Eds. L.A. Antonelli, et al., Cefalu, Italy, July 2004, AIP.

(Jager et al. 1997) Jager, R., Mels, W.A., Brinkman, A.C. et al., 1997, A&AS, 125, 557.

(Joinet et al. 2005) Joinet, A., Jourdain, E., Malzac, J., et al. 2005, ApJ, 269, 1008.

(Junior et al. 1999) Junor, W., Biretta, J. & Livio, M. 1999, Nature, 401, 891.

(Lebrun et al. 2004) Lebrun, F., Terrier, R., Bazzano, A. et al. 2004, Nature, 428, L293.

(Lebrun et al. 2003) Lebrun, F., Leray, J. P., Lavocat, P. et al. 2003, A&A 411, L141.

(Liu et al. 2000) Liu, Q. Z., van Paradijs, J., & van den Heuvel, E. P. J., 2000, A&AS ,147, 25.

(Liu et al. 2001) Liu, Q. Z., van Paradijs, J., & van den Heuvel, E. P. J., 2001, A&A ,368, 1021.

(Longair 1997) Longair M. S. High Energy Astrophysics vol. 1, second edition, Cambridge University Press, 1997.

(Lund et al. 2003) Lund, N., Butz-Jorgentsen, C., Westergaard, N. J. et al. 2003, A&A, 411, L231.

(Lutovinov & Revnivtsev 2003) Lutovinov, A. A., & Revnivtsev, M. G., 2003, Astron. Lett., 29, 719.

(Lutovinov et al. 2003) Lutovinov, A., Revnivtsev, M., Molkov, S. & Sunyaev, R., 2005, A&A, 430, 997.

(Markoff et al. 2001) Markoff, S., Falke, H., & Fender, R., 2001, A&A, 372, L25.

(Markoff et al. 2005) Markoff, S., Nowak, M. A., & Wilms, J., 2005, ApJ, 635, 1203.

(Markwardt et al. 2003) Markwardt, C.B., & Swank, J.H., 2003, Atel, 133.

(Manzo et al. 1997) Manzo, G., Giarrusso, S., Santangelo, A., 1997, A&AS, 122, 341.

(Mas-Hesse et al. 2003) Mas-Hesse, J.M., Gimnez, A., Culhane, L.J. et al. 2003, A&A, 411, L261.

(McClintock & Remillard 2003) McClintock, J. E., & Remillard, R., 2003, Review Article, astro-ph/0306213.

(Mitsuda et al. 1984) Mitsuda, K., Inoue, H., Koyama, K. et al. 1984, PASJ, 36, 741.

(Miller et al. 2004) Miller, C. M. & Colbert, F., 2004, Int. J. Mod. Phys. D 13, 1.

(Narayan et al. 1998) Narayan, R., Mahadevan, R., Quataert, E., 1998, Tbha. Conf., 148, astro-ph:9803141.

(Negueruela & Schurch 2007) Negueruela, I. & Schurch, P. E., 2007, A&A, 461, 631.

(Pandey et al. 2006) Pandey, M., Manchanda, R. K., Rao, A. P. et al., 2006, A&A, 446, 471.

(Parmar et al. 1997) Parmar A. N., Martin, D. D., Bavdaz, M. et al. 1997, A&AS, 122, 309.

(Parmar et al. 2003) Parmar A. N., Kuulkers, E., Oosterbroek, T. et al. 2003, A&A, 411, L421.

(Poutanen & Svensson 1996) Poutanen, J. & Svensson, R., 1996, ApJ, 470, 249.

(Psaltis 2004) Psaltis, D., 2004, astroph:0410536. To appear in "Compact Stellar X-ray Sources", eds. W.H.G. Lewin and M. van der Klis.

(Rhoades & Runy 1974) Rhoades, C. E. & Runi, R., 1974, Phys. Rev. Lett., 32, 6.

(Renaud et al. 2006) Renauld, M., Vink, J., Decourchelle, A. et al. 2006, ApJ, 647, L41.

(Revnivtsev et al. 2003a) Revnivtsev, M., Chernyakova, M., Capitanio, F. et al. 2003, Atel, 132.

(Revnivtsev et al. 2003b) Revnivtsev, M., Gilfanov, M., Churazov, E. & Sunyaev R. 2003, ATel, 150.

(Rupen et al. 2003a) Rupen, M. P., Mioduszewski, A. J. & Dhawan, V. et al. 2003, ATel, 142.

(Rupen et al. 2003b) Rupen, M. P., Mioduszewski, A. J., & Dhawan, V. et al. 2003, ATel, 152.

(Rupen et al. 2004a) Rupen, M. P., Mioduszewski, A. J., Dhawan, V. et al. 2004,ATel, 314.

(Rupen M. et al. 2004b) Rupen, M. P., Dhawan, V., Mioduszewski, A. J. et al. 2004, ATel, 304.

(Rutledge et al. 2000) Rurledge, R. E., Bildsten, L., Brown, E. et al. 2000, ApJ, 529, 985.

(Shakura & Sunyaev 1973) Shakura N. I. & Sunyaev R. A., 1973, A&A, 24, 337.

(Schronfelder et al. 1993) Schronfelder V., Aarts H., Bennett K., et al. 1993, ApJ Suppl, 86, 657.

(Shapiro & Teukolsky 1983) Shapiro, S. L., Teukolsky, S., 1983, Black holes, white dwarfs, and neutron stars: The physics of compact objects, Cornell University, Ithaca, NY.

(Skinner 1995) Skinner, G. K., 1995, Exp. Astron., 6, 1.

(Tanaka & Shibazasky 1996) Tanaka, Y., & Shibazasky, N., 1996, Annu. Rev. Astrn. Astrophys., 34, 607.

(Titarchuk 1994) Titarchuk L., 1994, ApJ, 434, 570.

(Titarchuk et al. 2005) Titarchuk, L., Shaposhnikov, N., 2005, ApJ, 626, 298.

(Tomsick et al. 2005) Tomsick, J. A., Corbel, S., Goldwurm, A. et al. 2005, ApJ, 630, 413.

(Tomsick 2004) Tomsick, J. A., 2004, in AIP Conf. Proc. 714: X-ray Timing 2003: Rossi and Beyond, astro-ph/0401189, 71.

(Ubertini et al. 2002) Ubertini P., Lebrun, F., Di Cocco, G. et al. 2003, A&A, 411, L131.

(Ubertini et al. 2005) Ubertini, P., Bassani, L., Malizia, A., 2005, ApJ, 629, L109.

(Vedrenne et al. 2003) Vedrenne, G., Roques, J.P., Shoenfelder, V., 2003, A&A, 411, L63.

(van der Klis 1998) Van der Klis, M., 1998, Adv. Sp. Res. 22, 925.

(Van Paradijs & Verbunt 1984) Van Paradijs, J., Verbunt, F., 1984, in S.E. Woosley, ed., High Energy Transients in Astrophysics, AIP Conference Procs 115, 49.

(White & van Paradijs 1996) White, N. E. & van Paradijs, J., 1996, ApJ, 473, L25.

(Wilms et al. 2001) Wilms, J., 2001, MNRAS, 328, L27.

(Wilson et al. 2001) Wilson, A., Young, A. & Shopbell, P., 2001, ApJ 546.

(Winkler et al. 2001) Winkler, C. & Courvoisier, T.L.L. et al. 2003, A&A, 411, L1.

(Winkler 2001) Winkler, C., 2000, In: Exploring the gamma-ray universe. Proceedings of the Fourth INTEGRAL Workshop, 4-8 September 2000, Alicante, Spain. ESA Publications, 471.

(Zdziarski et al. 1996) Zdziarski, A. A., Johnson, W. N. & Magdziarz, P., 1996, MNRAS, 283, 193.

(Zdziarski et al. 2000) Zdziarski, A. A., Poutanen, J., & Johnson, W. N., 2000, ApJ, 542, 703.

(Zdziarski 2000) Zdziarski, A. A., 2000, Highly Energetic Physical Processes and Mechanisms for Emission from Astrophysical Plasmas IAU Symposium, Vol. 195, 2000 P. C. H. Martens, S. Tsuruta, and M. A. Weber, eds.

(Zdziarski et al. 2002) Zdziarski, A. A., Poutanen, J., Paciesas W. S., 2002, ApJ, 578, 357.

(Zdziarski & Gierliński 2004) Zdziarski A. A. & Gierliński, M., 2004, Prog. Theor Phys. Sup. 155, 99.

(Zdziarski et al. 2004) Zdziarski A. A., Gierliński, M., Mikołajewska, J. et al. 2004, MNRAS, 351, 791.

(Woods et al. 2002) Woods P. M., Kouveliotou C., Finger M. H., 2002, IAUC 785.